EXPERIMENTAL AND THEORETICAL STUDY OF THE
QUARTZ/BRINE/OIL WETTABILITY USING GONIOMETRY AND THE
POISSON-BOLTZMANN EQUATION

Amanda Vilela Fonseca

Dissertação de Mestrado apresentada ao
Programa de Pós-graduação em Engenharia
Química, COPPE, da Universidade Federal
do Rio de Janeiro, como parte dos requisitos
necessários à obtenção do título de Mestre em
Engenharia Química.

Orientadores: Frederico Wanderley Tavares
                      Helen Conceição Ferraz

Rio de Janeiro
Outubro de 2023

EXPERIMENTAL AND THEORETICAL STUDY OF THE QUARTZ/BRINE/OIL WETTABILITY USING GONIOMETRY AND THE POISSON-BOLTZMANN EQUATION

Amanda Vilela Fonseca

DISSERTAÇÃO SUBMETIDA AO CORPO DOCENTE DO INSTITUTO ALBERTO LUIZ COIMBRA DE PÓS-GRADUAÇÃO E PESQUISA DE ENGENHARIA DA UNIVERSIDADE FEDERAL DO RIO DE JANEIRO COMO PARTE DOS REQUISITOS NECESSÁRIOS PARA A OBTENÇÃO DO GRAU DE MESTRE EM CIÊNCIAS EM ENGENHARIA QUÍMICA.

Orientadores: Frederico Wanderley Tavares
Helen Conceição Ferraz

Aprovada por: Prof. Frederico Wanderley Tavares
Prof. Helen Conceição Ferraz
Prof. Aurora Pérez Gramatges
D.Sc. Gabriel Duarte Barbosa

RIO DE JANEIRO, RJ – BRASIL
OUTUBRO DE 2023

Acknowledgments

Agradeço inicialmente às agências de fomento, CAPES e FAPERJ, que foram imprescindíveis para a execução do trabalho.

Uma das minhas principais conquistas durante a realização do mestrado foi o estabelecimento de conexões com inúmeras pessoas, algumas das quais talvez não imaginam a importância que tiveram para a conclusão deste trabalho. Por isso, deixo aqui meus sinceros agradecimentos:

Aos meus queridos orientadores Fred e Helen, pela remoção de todas as "barreiras" possíveis, pelos preciosos ensinamentos e pelo enorme apoio emocional.

À professora Natália Salles pela "co-orientação", paciência e solicitude, sempre arrumando um tempinho para compartilhar comigo seus conhecimentos da forma mais leve possível.

Ao professor João Victor Nicolini por todos os ensinamentos e motivação para conclusão deste trabalho.

A todos os membros do LaFIT e do Latema, que me acolheram e deram todo o suporte possível durante a realização do trabalho. Em especial, agradeço ao Rafael Nascimento, não só pelos seus ensinamentos, mas pelas incríveis palavras que muito me motivaram em momentos difíceis.

Ao meu amigo Marlon, pela empatia e pelo coração gigantesco, sempre disposto a compartilhar seus conhecimentos, motivar e facilitar todo o caminho percorrido.

Aos meus queridos amigos Katiane, Pedro e Juliana, sempre presentes oferecendo um ombro amigo, incentivo e apoio.

Aos meus queridos pais, por todo o suporte, amor incondicional e orações.

Ao meu marido Adriano, pelos fundamentais companheirismo, suporte, amor e compreensão durante todo esse tempo.

A todos os demais que direta ou indiretamente tenham me apoiado e colaborado para a execução deste trabalho.

"Nature is full of apparent contradictions resulting from our own ignorance of the true situation."

<div style="text-align: right;">Drew Myers</div>

EXPERIMENTAL AND THEORETICAL STUDY OF THE QUARTZ/BRINE/OIL WETTABILITY USING GONIOMETRY AND THE POISSON-BOLTZMANN EQUATION

Amanda Vilela Fonseca

Outubro/2023

Neste trabalho, a molhabilidade de sistemas trifásicos compostos por quartzo, decano e soluções de cloreto de sódio foi investigada utilizando goniometria e um modelo de pressão de disjunção baseado na Equação de Poisson-Boltzmann (PBE). Os ângulos de contato medidos exibiram uma variação modesta com o aumento da salinidade, concordando com os cálculos teóricos e valores experimentais reportados, como esperado para um sistema contendo óleo apolar. É importante ressaltar que o modelo baseado em PBE capturou consistentemente esse comportamento e o representou com acurácia, mesmo para a faixa de alta salinidade. Estendendo este trabalho, cálculos utilizando óleo cru ao invés de decano foram capazes de reproduzir de forma acurada dados experimentais reportados na literatura para uma ampla faixa de salinidades. O aumento do pH melhorou a concordância entre os dados calculados e experimentais nos sistemas altamente concentrados, sugerindo que informações adicionais sobre o sistema podem ser necessárias para explicar o comportamento da molhabilidade nessa faixa de concentração. Em resumo, as simulações revelaram o potencial de se observar as alterações de molhabilidade com variações na força iônica e no pH, bem como o impacto substancial das forças de van der Waals e de solvatação dentro do filme.

Abstract of Dissertation presented to COPPE/UFRJ as a partial fulfillment of the requirements for the degree of Master of Science (M.Sc.)

EXPERIMENTAL AND THEORETICAL STUDY OF THE QUARTZ/BRINE/OIL WETTABILITY USING GONIOMETRY AND THE POISSON-BOLTZMANN EQUATION

Amanda Vilela Fonseca

October/2023

Advisors: Frederico Wanderley Tavares
         Helen Conceição Ferraz

Department: Chemical Engineering

This work investigated the wettability of three-phase systems comprising quartz, decane, and sodium chloride solutions using goniometry and a disjoining pressure model based on the Poisson-Boltzmann Equation (PBE). The measured contact angles exhibited a modest variation with increasing salinity, in agreement with the calculations and previously reported experimental values, as expected for a non-polar oil system. Notably, the PBE-based model consistently captured and accurately represented this behavior, even for the high salinity range. Extending this work, calculations using crude oil instead of decane could accurately reproduce experimental data reported in the literature for an extensive range of salinities. The increase in the pH improved the agreement between calculated and experimental data in the highly concentrated systems, suggesting that additional information about the system may be required to explain the wettability behavior within this concentration range. In summary, calculations revealed the potential for observing wettability alterations with changes in ionic strength and pH and the substantial impact of van der Waals and solvation forces within the film.

Contents

List of Figures

List of Tables

Chapter 1

Introduction

Recent global events have sparked a heightened discussion surrounding the energy transition from fossil fuels to cleaner and renewable energy sources. However, this transition must confront the Energy Trilemma, encompassing energy security, energy equity, and sustainable development [1–3]. Energy transition brings about transformations not only in the actual infrastructure and current technologies but also in demographic distribution, labor activities, and even social implications such as cultural aspects, sense of belonging to a place, and identity. The existing disproportionate access to energy and energy decision-making process requires planning and adequate time to implement just transition programs [4]. The energy transition will be gradual, and it will not lead to the complete elimination of fossil fuels. Instead, different types of energy sources are going to coexist simultaneously [1].

Oil remains the primary global energy source, accounting for 31% of the world's energy consumption in 2021 [5]. Consequently, developing strategies to ensure sustainable and responsible use of oil plays an important role in dealing with the above mentioned future challenges.

Enhanced oil recovery (EOR) methods can improve the energy efficiency of petroleum production. Furthermore, some of these techniques can reduce the CO_2 intensity of produced oil under certain conditions [6]. Conventional oil recovery methods typically extract 25 to 50% of the oil present in the reservoir [7]. Consequently, EOR techniques are being implemented to optimize the utilization of the existing fields.

Low-salinity waterflooding is a well-known method for improving oil recovery [8–10]. Various mechanisms have been proposed to explain this process. However, a comprehensive understanding of the underlying interactions has not yet been achieved [11, 12].

Electrostatic forces influence fluid-rock interactions in oil reservoirs since water is also present alongside the rock and oil phases. These interactions affect the rock wettability, a parameter describing the ability of a fluid to spread on a solid surface

in the presence of other fluids [13]. The contact angle measurement is a commonly used technique to determine wettability [14].

There are different techniques that can be employed for measuring the contact angle [15]. The combinations of experimental and theoretical studies are highly beneficial in expanding knowledge in this field, especially considering the nanoscale phenomena involved, where measurements are still difficult to achieve. Such studies also allow for the evaluation of the consistency of the descriptive models. Modeling the theoretical contact angle can be approached in different ways. One such method is the disjoining pressure approach [14, 16, 17]. A challenge associated with this method lies in properly describing the interactions present in systems containing charged particles.

Different models, such as the Derjaguin-Landau-Verwey-Overbeek (DLVO) theory, Poisson-Boltzmann Equation, classical Density Functional Theory, and Molecular Dynamics can be used to describe the interactions between bodies, including those electrically charged [18–21]. Each of these approaches comes with its own benefits and limitations. The choice of which method to use depends on the complexity of the system being modeled, the specific information being sought, as well as the computational resources available.

Rock/brine/oil systems are inherently complex due to the significant influence of surface morphology, pore structure, and phase compositions on wettability. Hence, the use of simpler systems is favored in order to isolate the specific fluid-fluid or fluid-solid interactions that are occurring [22, 23]. This strategy can provide insights into the interactions in rock/brine/oil systems and, subsequently, support the well exploration planning and the development of various energy optimization strategies.

1.1 Objectives

In this context, the aim of this work is to study the wettability of quartz/oil/brine model systems employing contact angle measurements and a disjoining pressure method based on the Poisson-Boltzmann equation. To achieve this goal, the specific objectives are as follows:

1. Measuring the contact angles of an apolar model oil in contact with a quartz surface and brine solutions by goniometry;

2. Measuring the interfacial tension between an apolar model oil and brine solutions by tensiometry;

3. Evaluating the effect of ionic strength on the measured three-phase system contact angle and on the measured oil/brine interfacial tension;

4. Describing the contact angle between quartz, oil and brine using a disjoining pressure approach based on the Poisson-Boltzmann Equation and evaluating its consistency;

5. Extending the model to calculate the contact angle of a system containing a polar oil phase (a two-charged surfaces system);

6. Evaluating the influence of pH on the contact angle of the system containing a polar oil phase.

Chapter 2

Theory

2.1 Enhanced Oil Recovery

A reservoir is a porous formation impregnated with hydrocarbons (oil and/or gas) and water. It consists of multiple permeable layers bounded by impermeable rocks and an underlying aquifer. The presence of porosity gives rise to significant capillary forces within these media [24].

Wettability is a physical property that characterizes the interaction between a fluid and a surface in the presence of other fluids [13, 25]. In the context of rock/brine/oil systems, wettability plays a crucial role. It significantly impacts fluid distribution that can even be manipulated to optimize oil recovery [13, 26].

Anderson [13] classifies the systems into three categories: water-wet, where water is the main phase in contact with rock; oil-wet, where the rock exhibits a preference for oil; and neutrally-wet, where no strong preference for oil or water is found. An oil-wet reservoir is considered to be unfavorable to oil extraction. The contact angle (CA) is a quantitative measure of the wetting process and is commonly used in oil recovery studies [10, 13, 25]. However, it is important to recognize that wettability cannot be fully characterized by the contact angle alone. Surface morphology, pore structure and phase composition also significantly determine the overall wettability behavior [13].

Most of the world's reservoirs are made up of sandstones, which were formed either from the earth's surface debris or chemical precipitations in aqueous environments. These rocks predominantly consist of quartz grains with a smaller proportion of other components, such as clay minerals and silts [10, 24, 27]. Because of their large specific surface, clay minerals have a high capacity for ion adsorption. Usually, they are negatively charged in aqueous media [10]. Most minerals, including quartz and carbonates, exhibit strong water-wet behavior [13]. Consequently, a thin layer of water is expected to be present, covering the rock grains and in contact with the

oil [27]. However, certain minerals still have a greater affinity for the oil phase, such as graphite, talc, and coal [13].

The adsorption of surface active compounds present in petroleum on the rock surface can alter the original water wetness of a reservoir. However, due to the wide variety of these compounds, identifying which specific components are responsible for the wettability alteration is challenging [13].

Oil recovery can be categorized into three types: primary or natural depletion, which relies on the reservoir's energy; secondary, which involves the injection of water or gas into the well; and tertiary, which employs advanced techniques to improve oil production [7, 24]. Enhanced oil recovery (EOR) includes secondary and tertiary oil recovery processes. Conventional oil recovery methods are capable of recovering 25 to 50% of the oil present in the reservoir [7]. Consequently, there is a significant demand for new methods and ongoing studies to improve oil recovery efficiency further.

EOR methods can be classified as [7]:

1. Waterflooding: in which injected water is designed with a specific composition [9].

2. Thermal flooding: These methods involve the application of heat to decrease the oil viscosity. Examples include steam injection and *in situ* combustion [7, 27].

3. Chemical flooding: These techniques use chemical agents, such as polymers and surfactants, to reduce interfacial tension or increase the water viscosity. Chemicals such as polymers and surfactants are commonly used in this approach [27].

4. Gas injection: This method involves the injection of different gases, such as carbon dioxide or nitrogen, to enhance the miscibility of hydrocarbon phases and improve oil recovery efficiency [27].

5. Microbial oil recovery: In this method, microorganisms with good compatibility with the oil reservoir are injected, and by their underground activity (fermentation, production of metabolites, for instance) recovery of crude oil is enhanced [7].

2.2   Low-salinity waterflooding

Water injection is a common practice to keep well pressure and displace oil or gas [8, 9, 27]. However, by adjusting the composition and the salinity of the injected

water, it is possible to improve oil recovery. This engineered fluid can be called low-salinity or "smart" water [11]. This approach has gained significant attention as a cost-effective and environmentally friendly enhanced oil recovery method [10, 11, 28].

Different mechanisms have been proposed to explain how smart water influences EOR. These mechanisms include pH increase, migration of fine particles, ion exchange, expansion of the electric double layer, salting in effect, osmotic effect, and formation of microdispersions [10, 11, 29]. pH and salinity have a significant impact on surface charge and fluid interactions. pH directly influences the ionization reactions of surface-active compounds in crude oil and surface rock, as well as the solubility of the rock minerals [13]. Salinity is known to influence the expansion or contraction of the electrical double layer, which can increase the water film between rock and oil, a desired effect for improving oil mobility [28]. Additionally, salinity may promote the adsorption of surfactants onto the rock surface, especially in the presence of multivalent cations [10, 13]. Microdispersion formation is also considered a fundamental mechanism that controls the effectiveness of low-salinity waterflooing by facilitating interfacial interactions between the fluid phases [29]. However, there still need to be a consensus regarding the dominant mechanism driving the process, and further research is needed to understand the underlying mechanisms [8, 11].

Various factors that influence enhanced oil recovery through low-salinity waterflooding have been identified. [9, 11, 13]. Some of them are summarized below:

1. Low-salinity effect can be observed only in oils containing polar compounds (such as acid or basic organic molecules) [9].

2. The effective salinity range is between 1000 and 5000 ppm. Also, it was demonstrated that divalent cations such as Ca^{+2}, Mg^{+2} decreased oil recovery, while increasing SO_4^{2-}, K^+, and Na^+ improved it [8, 9, 11].

3. Rock composition significantly influences oil recovery, particularly because of the clay content [9]. Besides presenting high ion exchange capacity and swelling behavior, clay type also determines interaction strength among the three phases.

4. Existing connate water is also important since it contains multivalent cations, which are believed to act like bridges between oil and rock clay compounds [9, 28].

5. Initial oil-wet or neutral wet state is believed to be more favorable to observing low-salinity effects [13].

6. The pH in the water phase rules surface charges in oil and rock surfaces. At higher pH, sandstones are generally more hydrophilic, and low-salinity effects

6

are not well observed [11].

The impact of temperature and pressure is not extensively explored in the literature. Some studies have indicated a linear relationship between contact angle and temperature. On the other hand, the pressure effect is generally considered to be small or negligible [11, 30–33].

The complex composition of reservoirs presents challenges in formulating low-salinity water. Computer simulations of wetting phenomena offer a promising approach to address this complexity. These simulations enable the investigation of the various system interactions and isolate different effects, providing valuable insights into the behavior of "smart" water formulations.

2.3 The Contact Angle

The contact angle (CA) arises from intermolecular interactions present in a three-phase system. When a drop of one fluid is placed on a solid flat surface immersed in another fluid, a finite angle is formed at the three-phase line, representing the fluid-fluid interface's intersection with the solid plane. Figure 2.1 depicts the configuration of the CA in the context of oil reservoirs [15, 34].
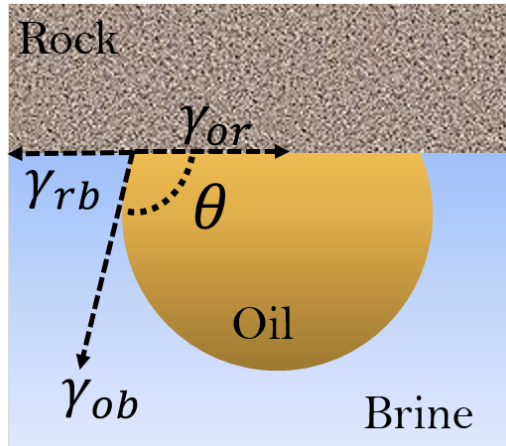
Figure 2.1: Contact Angle in a Three-Phase System: Solid-Brine-Oil.

The contact angle in this system can be described using Young Equation (2.1), which is valid for homogeneous, smooth, and rigid solid surfaces [15]. For a solid state, it is a statement of thermodynamic equilibrium [14].

$$\gamma_{ob} \cos \theta = \gamma_{rb} - \gamma_{or} \tag{2.1}$$

Being $\gamma_{i,j}$ the interfacial tension between the phases i and j. The subscripts 'o','r', and 'b' designate the oil, rock, and brine phases, in that order.

The condition for a finite contact angle is that $\cos\theta <= 1$. If θ equals 0, then the solid becomes completely wetted by the oil phase [34]. In this work, we consider the follow classification: if the wetting angle is greater than 90°, the system will be oil-wet. Otherwise, it is considered water-wet[27].

Contact angle measurements are typically performed using low-cost apparatus, and are relatively easy to manipulate. Different methods can be employed for contact angle measurements, including direct and indirect techniques. Direct methods, such as the sessile drop and captive bubble techniques, involve directly observing the shape of a liquid droplet or bubble placed on a solid surface. Indirect methods provide alternative parameters, which are used in contact angle determination. Some examples are tensiometry and geometric analysis of the meniscus shape [25, 35].

Young's equation is based on the assumption of a smooth and flat surface. However, most real surfaces exhibit irregularities and chemical heterogeneity. This can result in deviations between the experimentally observed CAs and the predicted ones by Young's Equation [35]. Two models are commonly used to account for surface roughness and heterogeneity: the Wenzel and the Cassie-Baxter models [25, 36, 37]. The former considers the roughness factor(r), defined by Equation (2.2), as the ratio between the actual and apparent surface areas. The relationship between the apparent (θ_{ap}) and Young's contact angle (θ) is determined by Equation (2.3).

$$r = \frac{actual\ surface\ area}{apparent\ surface\ area} \tag{2.2}$$

$$\cos\theta_{ap} = r\cos\theta \tag{2.3}$$

From Equation (2.3), we observe that when the Young angle is less than 90°, the apparent angle becomes smaller, while for θ greater than 90°, θ_{ap} increases[25].

The Cassie-Baxter model takes into account the chemical heterogeneity of the surface [15, 34, 38]. For a solid containing two types of regions with contact angles θ_1 and θ_2, which occupy the fractions *f* and (*1-f*) of the total interface area, Equation (2.4) describes the correlation between the apparent CA and the two Young's angles [38].

$$\cos\theta_{ap} = f\cos\theta_1 + (1-f)\cos\theta_2 \tag{2.4}$$

This equation is also applied to porous surfaces, where air becomes trapped on the surface grooves. This surface is considered to be heterogeneous because it is analogous to a composite made of solid and air phases [39].

2.4 Interfacial tension

At interfaces, atoms and molecules experience asymmetric forces when compared to the same species in a bulk solution. This results in a higher free energy and different properties in the boundary region between phases [25, 40]. The surface tension, also called interfacial tension (IFT), arises from the non-uniformity of local properties in the interface. It can be interpreted from different perspectives [25, 41].

From a thermodynamic perspective, interfacial tension represents the surface density of excess free energy or the work required to form a new unit surface by "cutting" a bulk phase [41]. Therefore, the higher the IFT, the greater the work to create a new surface. On the other hand, from the mechanical equilibrium condition perspective, it is regarded as the excess tangential force per unit of length of the surface perimeter or as the work required to stretch an existing surface to form a new unit area at constant volume and height [41, 42]. For liquids in equilibrium, both definitions lead to the same value [25, 41].

Figure 2.2 shows a curved interface with two curvature radii (R_1 and R_2), separating two bulk phases (α and β). The Young-Laplace Equation (2.5) describes the relation between the interfacial tension and the change of pressure (P_α-P_β) across this surface. It comes from the mechanical definition of IFT [25, 42].
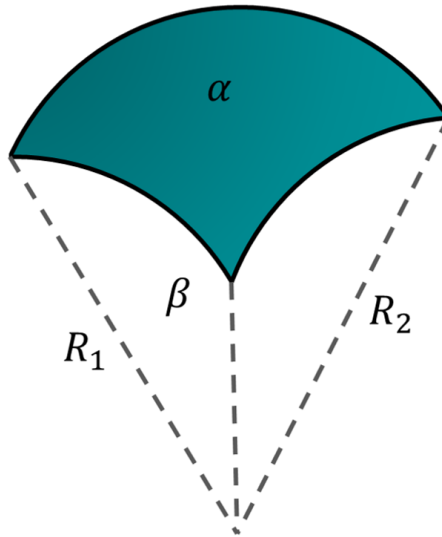
Figure 2.2: Curved interface of curvature radii R_1 and R_2, separating phases α and β.

$$P_\alpha - P_\beta = \gamma \left(\frac{1}{R_1} + \frac{1}{R_2} \right) \tag{2.5}$$

The greater the physical distinctions between the molecules of each phase, the greater the IFT [25]. Therefore, this parameter can be related to solubility and the

affinity between the phases [41].

Different techniques can be used to measure interfacial tension, such as: Pendant drop, Spinning drop, Wilhelmy plate and Du Noüy Ring [43]. The pendant drop technique (PD), in particular, has some advantages: it requires an small amount of sample, has high accuracy, and provides fast analysis [15]. PD is based on the Young-Laplace formulation for an axisymetric fluid droplet suspended from a needle (Figure 2.3) [44].
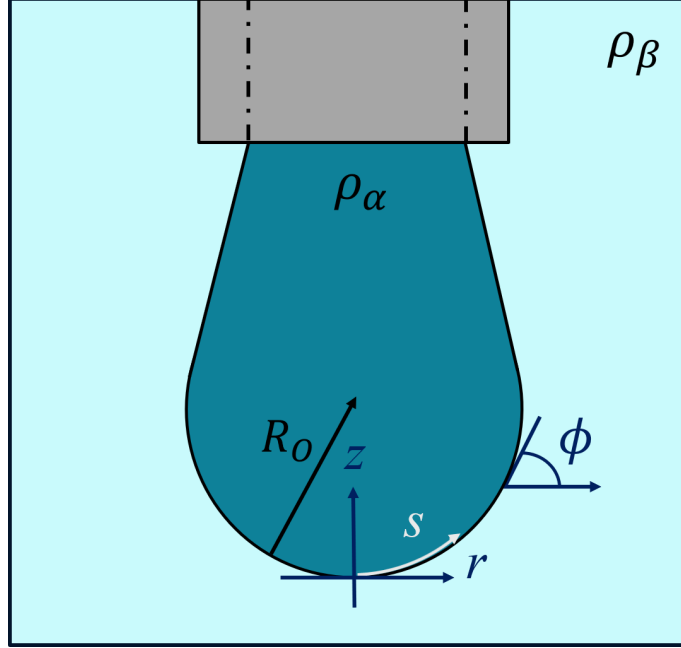
Figure 2.3: Geometric representation of a droplet suspended from a needle. Adapted from [15, 44].

Equations (2.6) to (2.8) describe the Young-Laplace formulation using cylindrical coordinates r, z, and the tangent angle ϕ. The fluids inside and outside the drop have densities ρ_α and ρ_β, respectively [44].

$$\frac{d\phi}{d\tilde{s}} = 2 - Bo\tilde{z} - \sin\phi \tag{2.6}$$

$$\frac{d\tilde{r}}{d\tilde{s}} = \cos\phi \tag{2.7}$$

$$\frac{d\tilde{z}}{d\tilde{s}} = \sin\phi \tag{2.8}$$

Being s the arc length measured from the drop apex. The bar above the variables indicates dimensionless quantities by R_o. Bo denotes the Bond number, as defined in Equation (2.9) [44].

$$Bo \equiv \frac{\Delta\rho R_o^2 g}{\gamma} \tag{2.9}$$

$\Delta\rho$ represents the difference between the densities of the two fluids. In practice, by adjusting the drop image profile and solving the set of differential equations, the Bond number can be determined. The interfacial tension is then directly obtained from the Bo [44].

2.5 Modelling interactions in charged systems

In aqueous media, most surfaces become electrically charged due to the high dielectric constant of water. The charging of surfaces can occur through various processes: preferential solubilization of surface ions, ionization of surface groups, substitution of surface ions, ion adsorption, and charging arising from specific crystal structures [25, 34, 45]. The presence of electrical charge on surfaces holds great significance as it can influence intermolecular interactions and have implications for various phenomena, including particle coalescence. For instance, the coalescence of equal particles can be prevented by manipulating repulsive electrostatic forces [25, 34].

Surface charges lead to the redistribution of nearby electrolyte ions so that counterions are attracted towards the surface while coions are repelled. This originates the so-called electric double layer (EDL): the first layer comprises the surface charges, and the second consists of nearby ions [19]. Different models have been proposed to describe the structure of the EDL. In 1879, Helmholtz considered an arrangement of charges in two parallel planes, similar to a capacitor. Gouy and Chapman (1910-1917) considered the thermal motion of ions, leading to the formation of a diffuse layer. Later, in 1924, Stern proposed a modification to the Gouy-Chapman model, taking into account the phenomenon of surface potential inversion [19, 34, 46].

The linearized Poisson-Boltzmann Equation, combined with the Hamaker model, forms the basis of the Derjaguin-Landau-Verwey-Overbeek (DLVO) theory, which has great historical importance, since it was the first model capable of explaining the stability of colloidal systems [19, 25]. The development of the modified Poisson-Boltzmann Equation led to significant improvements by incorporating dispersion interactions with polarizability effects at the same level of non-linearity as the electrostatic contributions [47, 48]. More detailed approaches, such as the classical density functional theory and molecular dynamics, have also been applied to some specific systems, where higher concentrations or elevated surface charge densities lead to deviations [49–52].

Molecular Dynamics is a computational method derived from statistical mechanics. It is also referred to as a "computational experiment", which explicitly describes existing the system species. This path provides more realistic results de-

spite increasing dramatically the degrees of freedom and, consequently, the required computational time [21]. Density Functional Theory, originated from statistical mechanics, was proposed by Hohenberg and Kohn in 1964. They established that the many-particle ground state free energy is a unique functional of the ground state electronic density [53]. Classical Density Functional Theory (cDFT) is an analogous approach to DFT: the free energy is expressed as a functional of the density of all species, such as atoms, ions, and molecules [20]. Compared to the above strategies, cDFT offers a more detailed description of the existing interactions - *e.g.*, Coulombic, electrostatic correlations, hard-spheres contributions - while a lower computational cost is generally required compared to molecular dynamics [50].

2.6   Poisson-Boltzmann Equation

In charged systems, neglecting gravitational effects, the total chemical potential of a component i, μ_i, is determined by various contributions, including ideal, electrostatic and non-electrostatic terms (Equation 2.10) [21, 48].

$$\mu_i(r) = \mu_i^0 + k_B T \ln \rho_i(r) + z_i e \psi(r) + \sum_j E_{ij}(r) \qquad (2.10)$$

Where μ_i^0, ρ_i, and z_i denotes the reference state chemical potential, the concentration and the valence of component i. The term ψ represents the mean field electrostatic potential as a function of spatial coordinate r. e is the elementary charge (1.60×10^{-19} C), k_B is the Boltzmann constant, and T represents the temperature. E_{ij} encompasses all non-electrostatic potentials that can be accounted for, such as van der Waals, external field, image, and excluded volume potentials [48].

In the bulk phase, denoted by the superscript 'b', Equation (2.10) becomes:

$$\mu_i^b = \mu_i^0 + k_B T \ln \rho_i^b + z_i e \psi^b + \sum_j E_{ij}^b \qquad (2.11)$$

As a condition of chemical equilibrium, chemical potential should be equal for each component in all phases. Therefore, combining the equations for a bulk phase and an interfacial region, we obtain the modified Boltzmann distribution of ions (Equation 2.12):

$$\rho_i(r) = \rho_i^b \exp\left\{ -\frac{z_i e[\psi(r) - \psi^b] + \sum_j [E_{ij}(r) - E_{ij}^b]}{k_B T} \right\} \qquad (2.12)$$

In the bulk, the electrostatic potential (ψ^b) and electrical field are taken to be zero [18].

The Poisson-Boltzmann Equation (PBE) derives from the combination of the

Boltzmann distribution of ions, which neglects all other non-electrostatic potentials, with the Poisson equation (Equation 2.13) [19, 45, 54]. In this theory, ions are treated as point charges without volume, surrounded by a continuous phase of a dielectric medium [54]. It provides a mathematical correlation between the electrostatic potential and the ion density profile in the system.

$$\varepsilon_0 \nabla \cdot [\varepsilon \nabla \psi(r)] = -\sum_i z_i e \rho_i(r) \tag{2.13}$$

Where ε represents the medium dielectric constant, and ε_0 the vacuum permittivity (8.854×10^{-12} $C^2 N^{-1} m^{-2}$) [45].

Equation (2.14) gives PBE in its original formulation [19, 21, 45].

$$\varepsilon_0 \nabla \cdot (\varepsilon \nabla \psi(r) = -e \sum_i z_i \rho_i^b exp \left[\frac{-e z_i \psi(r)}{k_B T} \right] \tag{2.14}$$

It is worth mentioning that the PBE can be considered a specific case of the cDFT when size and electrostatic correlations are disregarded [50].

The linearized version of PBE, as shown by Equation (2.15), is known as the Debye-Hückel theory (DH). It provides good predictions at low potentials and low electrolyte concentrations. This formulation has played a significant role in developing the DLVO theory, the first model capable of qualitatively describing the stability of colloidal systems. DLVO calculates the total interaction energy between particles by summing the van der Waals interaction energy with the electrostatic energy term [19, 25, 45].

$$\nabla^2 \psi(r) = \kappa^2 \psi(r) \tag{2.15}$$

Where κ (Equation 2.16) is the inverse of the Debye length, which is a reference length of the double electric layer thickness [18, 54].

$$\kappa^2 = \frac{2e^2 I}{\epsilon \epsilon_0 k_B T} \tag{2.16}$$

Being I the ionic strength of the aqueous medium, calculated by Equation (2.17) [18].

$$I = \frac{\sum_i \rho_i^b z_i^2}{2} \tag{2.17}$$

For a system containing only one charged flat surface in contact with a salt aqueous solution, with low surface potential (below 25mM), the following expression (Equation 2.18) gives the electrostatic potential along the distance z from the surface [19, 45].

$$\psi(z) = \psi_0 \exp(-\kappa z) \tag{2.18}$$

Being ψ_0 the potential at the $z = 0$ or at the surface.

Equation 2.19, which is a simplification of the Grahame equation, relates the surface charge density (Q_0) with ψ_0 for the same system.

$$Q_0 = \varepsilon_0 \varepsilon \kappa \psi_0 \tag{2.19}$$

When charged particles move within an electrolyte solution, a portion of the fluid moves together with the particles. The plane that separates the region of the fluid moving alongside the particle is termed shear plane. The zeta potential (or electrokinetic potential) corresponds to the electrostatic potential at this shear plane [19, 25]. The experimental measurements of this potential can be used to estimate the surface potential [47].

In DLVO theory, even incorporating the polarizability effects from Lifshitz theory in the Hamaker constant calculation between bodies, inconsistencies still arise ([48]). The linearization of PBE is a simplification that causes the loss of some information, applying only to low electrostatic potentials [47, 54]. Consequently, other numerical methods, such as finite volume, finite differences, and orthogonal collocation, have been employed to solve PBE accurately [47].

In concentrated systems, where ion sizes and electrostatic correlations between them are more pronounced, the calculation of thermodynamic properties may need to be revised [34, 48, 50, 55]. The modified Poisson-Boltzmann equation (mPBE) is one way to reach this, improving the consistency of the total mean interaction potential calculation. This happens because the non-electrostatic interactions are treated with the same level of non-linearity as electrostatic contributions, as shown in Equation (2.20) [47, 48].

$$\varepsilon_0 \nabla \cdot (\varepsilon \nabla \psi) = -e \sum_i z_i \rho_i^b exp\left(-\frac{z_i e \psi + \sum_j E_{ij}}{k_B T}\right) \tag{2.20}$$

Since mPBE (or PBE) is a second-order non-linear differential equation, its solution requires the specification of two boundary conditions (BC) [45]. There are three kinds of boundary conditions. For a system constituted by two surfaces in contact with the electrolyte, the possible BC are [18, 21, 45]:

1. Dirichlet: The mean electrostatic potential is specified at the boundary.

$$\psi|_{surface1} = \psi_1 \tag{2.21}$$

$$\psi|_{surface1} = \psi_2 \tag{2.22}$$

Where ψ_i is the mean electrostatic potential at surface i.

2. Neumann: The derivative of the mean electrostatic potential is specified at the boundary.

$$[\varepsilon \nabla \psi]|_{surface1} \cdot \vec{n} = -\frac{Q_1}{\varepsilon_0} \qquad (2.23)$$

$$[\varepsilon \nabla \psi]|_{surface2} \cdot \vec{n} = -\frac{Q_2}{\varepsilon_0} \qquad (2.24)$$

Where Q_i is the charge density at surface i, and $\vec{n}$ is a unit normal vector to the surfaces.

3. Robin: It is a linear combination of Dirichlet and Neumann BC. This condition is often used in systems where pH or other ions close to the surface influence charge densities. In this case, a charge regulation model is required to solve PBE.

2.6.1 Charge regulation model

In most surfaces immersed in aqueous media, ionizable surface groups are not completely dissociated, leading to alterations in charge density and surface potential [45]. This issue is commonly addressed by a surface complexation model (SCM) [56–60]. The charge regulation will directly influence the boundary conditions of Equations (2.23) and (2.24). In this work, we will use the approach of Lima *et al.* (2017) and Barbosa (2019) [50, 57]. First, the following reaction (Equation 2.25) will be considered at the surface:

$$> SH \leftrightarrows \ > S^- + H^+ \qquad (2.25)$$

The symbol $>$ represents the surface, and S is any surface group.

From the chemical equilibrium criteria [61], K_{eq} is defined as:

$$K_{eq}(T) = \prod_i^C a_i^{v_i} \qquad (2.26)$$

Being C, the total number of components, $a_i^{v_i}$ the activity of the component i, and v_i the stoichiometric number in the reaction.

Assuming that the activity coefficient of the species i can be approached by its local molar density at the surface ($\rho_i|_{surface}$), and that the number of surface sites is equal to their molar surface density ($N_{>SH}$), the equilibrium constant will be expressed by Equation (2.27) [50].

$$K_{eq}(T) = \frac{\rho_{S^-}|_{surface}\rho_{H^+}|_{surface}}{N_{>SH}} \tag{2.27}$$

The maximum surface sites density (N_{max}) is defined as:

$$N_{max} = N_{>SH} + N_{S^-} \tag{2.28}$$

The charge density of the surface (Q) may be expressed by the sum of densities of the charged sites, and their charge number as:

$$Q = e \sum_i z_i N_i \tag{2.29}$$

The combination of Equations (2.27), (2.28), and (2.28) yields an expression for the surface charge density (Equation 2.30), which can be used as a boundary condition. Notably, Q will depend only on the maximum number of surface sites and the local density profile of H^+ at the surface.

$$Q = \frac{-eK_{eq}N_{max}}{K_{eq} + \rho_{H^+}|_{surface}} \tag{2.30}$$

2.7 Van der Waals interactions

Van der Waals (VDW) forces arise from coordinated interactions of moving electric charges, currents, and fields, averaged on time [62]. They are responsible for different phenomena, including phase condensation, adhesion, adsorption, and wetting. These interactions are classified into three types: Keesom, Debye, and London (or dispersive) forces [45, 62].

At the atomic scale, van der Waals forces are weaker than Coulombic interactions. However, when considering macroscopic bodies, the net interaction energy becomes proportional to the size, which makes them much stronger [45]. From a pairwise summation approximation, Hamaker calculated the energy interaction between spherical particles, introducing a coefficient of interaction, which was further nominated by the Hamaker constant [62, 63]. This pairwise summation depends on the geometry of the system. For example, the VDW energy interaction between two flat surfaces per unit area, W_{flat}, can be written as:

$$W_{flat} = -\frac{A}{12\pi l^2} \tag{2.31}$$

Being A the Hamaker constant, and l the separation distance between the surfaces.

Two disadvantages of the Hamaker approach are the assumptions of additivity

and non-retardation of the pair potential. The first limitation can be overcome by considering the Lifshitz theory, which originates in quantum mechanics. It treats large bodies as continuous media, ignoring their atomic structure. Incorporating the Lifshitz theory, the Hamaker constant can be calculated from bulk properties, such as dielectric constants and refractive indexes. For two bodies one (1) and two(2), interacting across a third (3) medium, the non-retarded Hamaker constant ($A_{non-ret}$) can be calculated [45]:

$$A_{non-ret} \approx \frac{3}{4}kT \left(\frac{\varepsilon_1 - \varepsilon_3}{\varepsilon_1 + \varepsilon_3}\right) \left(\frac{\varepsilon_2 - \varepsilon_3}{\varepsilon_2 + \varepsilon_3}\right) + \frac{3h}{4\pi} \int_{\nu_1}^{\infty} \left(\frac{\varepsilon_1(i\nu) - \varepsilon_3(i\nu)}{\varepsilon_1(i\nu) + \varepsilon_3(i\nu)}\right) \left(\frac{\varepsilon_2(i\nu) - \varepsilon_3(i\nu)}{\varepsilon_2(i\nu) + \varepsilon_3(i\nu)}\right) d\nu \quad (2.32)$$

Where ε_j are the static dielectric constants of medium j; $\varepsilon_j(i\nu)$ is the ε at imaginary frequencies (ν), $\nu_1 = 2\pi k_B T/h$, and h is the Planck's constant.

While the first term in (2.32) represents the Keesom and Debye forces, the second accounts for the London forces. Considering that the absorption frequencies of all three media are the same, the expression for the non-retarded Hamaker constant is [45]:

$$A_{non-ret} = A_{\nu=0} + A_{\nu>0} = \frac{3}{4}kT \left(\frac{\varepsilon_1 - \varepsilon_3}{\varepsilon_1 + \varepsilon_3}\right) \left(\frac{\varepsilon_2 - \varepsilon_3}{\varepsilon_2 + \varepsilon_3}\right) + \frac{3h\nu_e}{8\sqrt{2}} \frac{(n_1^2 - n_3^3)(n_2^2 - n_3^3)}{(n_1^2 + n_3^3)^{-1/2}(n_2^2 + n_3^3)^{-1/2}[(n_1^2 + n_3^3)^{-1/2}(n_2^2 + n_3^3)^{-1/2}]} \quad (2.33)$$

Being n_i, the refractive index of medium i, and ν_e the main electronic absorption frequency in the UV, assumed as $3 \times 10^{15} s^{-1}$ [45].

Some interesting features of VDW are: 1) the interaction between identical particles across any medium is always attractive; 2) when the medium is vacuum or air, there is always and attractive force between any two bodies. The Lifshitz theory is restricted to systems where the distance between particles is larger than molecular dimensions, where energy fluctuations become significant [45].

Another effect that should be taken into account is the modification of the Hamaker constant due to electrolytes in the third medium [45]. The electrostatic field between surfaces becomes screened due to the polarization of charges, leading to an exponential decay in the interaction potential with increasing distance. The screening on the Hamaker constant is particularly pronounced at small separation distances. Equation (2.34) can be used to compute this alteration [45].

$$A_{non-ret,scr} \approx A_{non-ret,v=0} e^{-\kappa l} + A_{non-ret,v>0} \quad (2.34)$$

Retardation effects come from the finite time required for the propagation of interactions between particles. An approximate correction (Equation 2.35) can be applied considering the retardation effects, as developed by Gregory [64].

$$A_{ret,v>0} \approx \frac{A_{non-ret,v>0}}{1 + 5.32\lambda_c^{-1}l} \tag{2.35}$$

Where λ_c is a characteristic wavelength, often assumed as 100 nm [64].

2.8 The relationship between disjoining pressure and contact angle

There are different approaches to model the contact angle, such as the surface tension component [17, 65], three-dimensional classical density functional theory [66], and the disjoining pressure method [16, 67, 68]. The latter takes into account the thin film of salt water that exists between the oil and rock surfaces, which is illustrated in Figure 2.4.
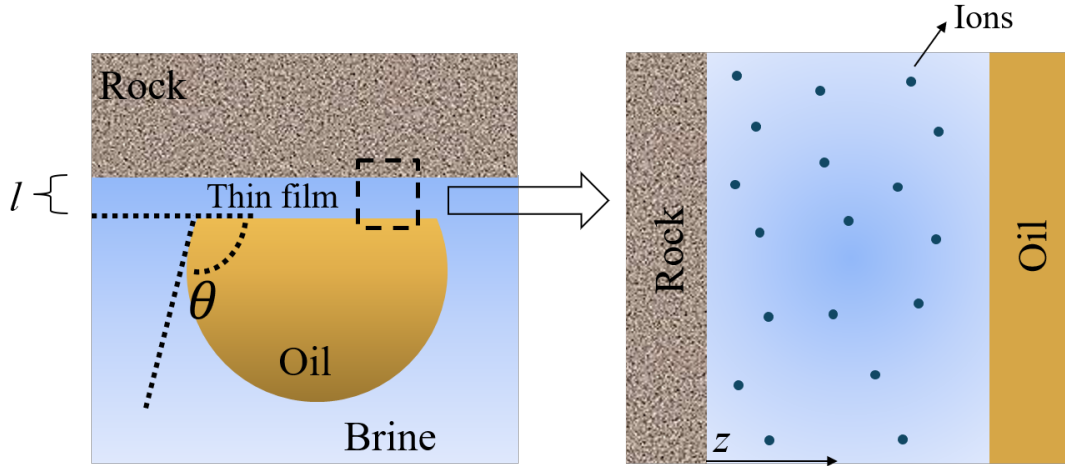
Figure 2.4: Thin film of brine between rock and oil phases.

In contrast to thick films, where the interlayer behaves as a bulk phase, retaining bulk properties, thin films exhibit overlapping transition zones of both interfaces across the film. As a result, the thermodynamic properties in that region become dependent on the separation distance. Then, a non-uniform density profile of species is present along the film [67, 69, 70].

This non-homogeneity causes a difference between the film pressure (P_f) and the pressure of a bulk phase (P_b) that has been thinned to form the actual film. This difference is called as the disjoining pressure (Π) [68, 69].

$$\Pi(l) = P_f - P_b \tag{2.36}$$

Being l, the film thickness.

As the thickness of the film increases, the absolute value of the disjoining pressure decreases, eventually disappearing in thick films [69]. The disjoining pressure can be negative or positive. In the case of negative disjoining pressure, it tends to bring the interfaces closer together; otherwise it tends to separate them [67].

For a flat and thin film of brine (Figure 2.4), the disjoining pressure can also be written as shown in Equation (2.37) [67, 70]:

$$\Pi(l) = -\frac{\partial(\gamma^f)}{\partial l} \tag{2.37}$$

Being γ^f the film tension. When the film is thick, the film tension equals the sum of the interfacial tensions on each side of the film, as shown in Equation (2.38) [67, 68, 70].

$$\gamma^f_{l\to\infty} = \gamma_{rb} + \gamma_{ob} \tag{2.38}$$

Being γ_{ij} the interfacial tension between phases i and j. The superscript 'f' designates the film.

However, a thin film differs from a thick one by a term related to the disjoining pressure, as shown in Equation (2.39) [67, 68, 70].

$$\gamma^f = \gamma_{rf} + \gamma_{of} + \Pi l \tag{2.39}$$

Replacing Equation (2.39) in Equation (2.37), and integrating the disjoining pressure from infinite (i.e., a thick film) to an equilibrium thickness, l_{eq}, we find [68]:

$$\gamma^f = \gamma_{rb} + \gamma_{ob} + \int_{l_{eq}}^{\infty} \Pi(l)dl + (\Pi l)_{eq} \tag{2.40}$$

For a hypothetical situation where the film thickness is zero, $\gamma^f \approx \gamma_{or}$ [67]. Therefore, the corresponding Young's equation to this system will be Equation (2.41).

$$\gamma^f = \gamma_{rb} - \gamma_{ob} \cos \theta \tag{2.41}$$

The replacement of Equation (2.41) in Equation (2.40) yields a relationship between the contact angle and disjoining pressure [68]:

$$\cos \theta = -1 + \frac{\int_{l_{eq}}^{\infty} \Pi(l)dl - (\Pi l)_{eq}}{\gamma_{ob}} \tag{2.42}$$

The conditions for the integral term in Equation (2.42) can be evaluated as follows [71]:

1. If $\int_{l_{eq}}^{\infty} \Pi(l)dl < (\Pi l)_{eq}$, the brine completely wets the solid;

2. If $(\Pi l)_{eq} \leq \int_{l_{eq}}^{\infty} \Pi(l)dl \leq (\Pi l)_{eq} + \gamma_{ob}$, the system holds a water-wet regime;

3. If $(\Pi l)_{eq} + \gamma_{ob} \leq \int_{l_{eq}}^{\infty} \Pi(l)dl \leq (\Pi l)_{eq} + 2\gamma_{ob}$, the system holds an oil-wet regime;

4. If $\int_{l_{eq}}^{\infty} \Pi(l)dl > (\Pi l)_{eq} + 2\gamma_{ob}$, the oil completely wets the solid;

The contact angle calculation relies on identifying appropriate terms for the disjoining pressure. It can be split into three contributions: electrical double layer (Π_{EDL}), van der Waals (Π_{vdW}), and structural or solvation (Π_s) [16, 67, 72].

$$\Pi = \Pi_{EDL} + \Pi_{vdW} + \Pi_s \tag{2.43}$$

Following the work of Barbosa [50] and Hirasaki [67], Equations (2.44) and (2.45) can be used to calculate the electrical double layer and van der Waals contributions to the total disjoining pressure. The first term on the right side of Equation (2.44) is the electrostatic contribution, whereas the second is an entropic contribution. Since the disjoining pressure should be independent of the position z along the film, it is chosen to be at the midplane ($z = l/2$). The van der Waals contribution is obtained by taking the derivative with respect to l of the VDW interaction energy between two flat surfaces (Equation 2.31).

$$\Pi_{EDL}(l) = -\frac{1}{2}\varepsilon_0\varepsilon\left(\frac{d\psi}{dz}\right)^2_{z=l/2} + k_B T \sum_i [\rho_i(z = l/2) - \rho_i^b] \tag{2.44}$$

$$\Pi_{vdw}(l) = -\frac{A_{\nu=0}\exp(-\kappa l)(2 + \kappa l)}{12\pi l^3} - \frac{A_{\nu>0}(2 + 15.9\kappa l_c^{-1}l)}{12\pi l^3(1 + 5.32\lambda_c^{-1}l)^2} \tag{2.45}$$

The Hamaker constants $A_{\nu=0}$ and $A_{\nu>0}$ can be calculated with Equation (2.33).

Van der Waals and PBE models do not account for the effects of hydrogen bonding or specific interactions between water and ions, which are referred to the solvation or structural forces. For films with thicknesses close to the molecular size, a strong repulsion sets in, and molecules can arrange themselves to achieve an efficient packing [14]. This effect is found to be significant at separations up to 5nm [73]. The structural contribution to the disjoining pressure (Π_s) is calculated using Equation (2.46).

$$\Pi_s(l) = A_s \exp{-\frac{l}{l_s}} \tag{2.46}$$

Being A_s a model coefficient, assumed as 1.5×10^5 bar, and l_s the characteristic decay length, assumed as 0.05nm [67].

2.9 Comments on recent studies

Studies involving low-salinity waterflooding (LSWF) for enhanced oil recovery applications began more than 70 years ago [11]. Current research is focused on understanding the underlying mechanisms, which can be achieved using different strategies, such as experimental and computational methods [11, 74]. For the former, the following techniques are commonly employed: contact angle, interfacial tension, zeta potential, core flooding, imbibition tests, and atomic force microscopy (AFM) [75–80]. The latter studies uses the well-known DLVO theory, with some improvements on the surface complexation reactions, Molecular Dynamics (MD), and quantum density functional theory (qDFT) simulations [12, 60, 79, 81–85]. Few studies have been reported using the classical density of functional theory (cDFT) [66, 86].

2.9.1 Low-salinity waterflooding mechanisms

The mechanisms of LSWF are still a subject of debate. Al-Saedi *et al.* [76] conducted a study to investigate the isolated effect of quartz and quartz with clays in the presence of low-salinity water on the recovery of sodium acetate using chromatography. Their investigation revealed pH alteration, ionic exchange, and a possible cation bridging effect (for Ca^{+2}). Their findings concluded that pure quartz was the main component responsible for the observed change in sodium acetate recovery (chosen to represent a polar oil). They observed some differences such as reduced permeability and fines migration in columns containing both clay and quartz in comparison to the pure quartz column. These could influence the observed trend in sodium acetate recovery.

In contrast, the works of Wei *et al.* [78], Ivuawuogu *et al.* [77], and Saeed *et al.* [83] showed the opposite. Wei *et al.* [78], using synthetic clay-sand packs in water flooding experiments found that LSWF could increase oil recovery only when clay minerals were present. Ivuawuogu *et al.* [77] also showed an increase in the oil recovery in columns containing clays compared to clay-free sand pack columns in core flooding experiments. Electrostatic effects (changes in zeta potential) and clay swelling were regarded as the central mechanisms. Saeed *et al.* [83] also corroborate these findings. They correlated a maximum energy barrier parameter calculated with an improved DLVO-based model with literature experimental CAs. They verified that clays could alter the zeta potential and wettability, depending on their surface site densities and specific surface areas. Performing a sensitivity analysis, they also classified the following factors in order of importance for the reservoir wettability: Ionic strength and brine composition, pH, temperature, sandstone mineralogy, total acid number, and total base number.

Not only the salinity but the control of the composition of the injected water is proven to be essential to oil recovery [11, 74]. The work of Liu *et al.* [80], using contact angle measurements, showed that decreasing salinity contributes to the wettability alteration towards more water spreading on the rock. However, this effect is minimized in the presence of divalent cations, as they act creating a bridge between oil and rock surfaces. On the other hand, divalent cations have a positive impact on permeability, leading to improved oil recovery and suggesting the use of a mixture of mono and polyvalent ions on low-salinity water.

The study of Hu *et al.*[79] supports the findings regarding the valence of cations. Using AFM, the authors demonstrated that the interaction between apolar group functionalized tips and a quartz glass is very weak compared to the force between carboxylic and silanol groups. The later force was also stronger when a brine with polyvalent cations was employed. For an apolar oil, the force between groups varied significantly, with concentration change only for brines containing polyvalent cations. For the polar tip, increased the interaction for all brines. The computational description of the system using MD simulations confirmed the experimental results and allowed the observation of the cation bridging effect between oil and silica surfaces.

Fluid-fluid interactions and their effects are also a part of the ongoing discussion on oil recovery due to the various trends of interfacial tension observed between oil and brine over the years. In some cases, IFTs do not reflect directly the wettability alteration [22, 87, 88]. Besides, the formation of water microdispersions is not in complete consensus. While some authors regard this mechanism as decisive for oil recovery [29, 89], others disagree [22, 90].

In the work of Rostami *et al.* [22], the salinity effect on the interfacial tension between crude or synthetic oil phases and diluted seawater was studied experimentally. In both systems, they observed an initial decrease of IFT with increasing salinity, followed by an increase with further salt additions. A similar trend for crude oil/seawater interfaces was found by Tetteh *et al.* [89]. Rostami *et al.* [22] explained that the first decrease was attributed to the transfer of cations to the oil phase, which interacts with the polar surface active agents. This interaction results in a reduction of the Gibbs free energy. The later increase in IFT was regarded as a salting-out effect, where water molecules cannot "hold" ions and polar organic compounds and tend to hydrate the incoming ions. Additionally, an interesting observation was the study of the adsorption of asphaltenes with a micromodel oil/brine interface. As expected, the brine salinity at which the adsorption was maximal coincided with the lowest IFT value. However, the measured contact angles between crude oil/brine/dolomite decreased with the increase in salinity. Since wettability alteration did not follow the same trend as IFT, it suggests that interactions between fluids and the

solid my impact the overall wettability behavior.

In the study of Mokhtari *et al.* [91], fluid-fluid interactions were evaluated through core flooding experiments. They used synthetic glass cores, crude oil, and synthetic brines with compositions mimicking formation and seawater in different concentrations. The highest and lowest recovery rates corresponded to the lowest and highest IFTs of brines. Interestingly, due to the dissolution of polar components into the brine, the pH and IFT of fresh and effluent brines varied significantly in the lower concentrated brines. Therefore, the fluid-fluid interactions were found to influence oil recovery greatly.

The effect of salinity in the IFT of the work of Saw and Mandal [88], was similar to the behavior of the aforementioned studies. However, the wettability alteration due to salinity was uncorrelated with the IFT changes. It agreed with the zeta potential measurements, which demonstrated the ion screening effect on the oil/brine interface and the inversion of the electrostatic potential in carbonate rock/brine interfaces due to the hydrolysis reactions of carbonate. Therefore, IFT alteration was not considered the leading mechanism but rather the calcite dissolution and the adjustment of ion composition.

As seen, several questions regarding the mechanisms of oil recovery by low-salinity water still need to be addressed. Crude oil and the rock have a complex composition, leading to significant changes in the system, such as: Phases composition, pH, interfacial tension, electrical and optical properties. Besides, many other experimental conditions may influence low-salinity effects. Therefore, the study of simpler systems is favored to isolate the specific fluid-fluid or fluid-solid interactions that are occurring [22, 23]. This will serve as a fundamental premise of this work, which will investigate the effect of salinity on wettability and fluid-fluid interactions.

2.9.2 Proposed model and similar studies

Appropriate phases should be chosen to propose a model system that captures important features of the reservoirs. Quartz was selected as the solid phase since it is the major component of sandstones. In order to represent a system containing only one charged surface, a hydrocarbon is the most suitable choice. Because some similar studies have utilized n-decane, it was chosen as the oil phase of this work [12, 17, 23, 32, 84, 87]. As for the brines, monovalent salt solutions of sodium chloride were selected. A disjoining pressure model based on PBE was selected to calculate the theoretical equilibrium contact angle [50]. This model is appropriate for a simple system containing a monovalent salt, and it should be able to describe it in a suitable way. Below, the results of some relevant studies involving similar systems are presented. It is important to note that while DLVO and PBE models

are often employed in this field, a majority of calculations presented have employed Molecular Dynamics to observe specific aspects, which can be helpful to evaluate the results of the proposed model in this work.

Zhao *et al.*[87] conducted a study using MD simulations to investigate the interface of between n-decane and sodium chloride solutions with concentrations ranging from 0.0 to 1.0 M. They observed an almost ion-free layer, indicating the low affinity between the ions and n-decane for all salinity ranges. The calculated IFT exhibited an initial decrease reached a minimal value at 0.2M and increased until 1.0M. The interfacial thickness showed an opposite trend. By evaluating the radial distribution functions of the species, they concluded that the change in adsorption interactions between water and n-decane were responsible for the observed effect: in 0.2M, they found the weakest adsorption between water and decane, which indicated that the interface structure was the loosest at this concentration.

Using MD simulations, Fang *et al.* [84] demonstrated important features of a thin sodium chloride brine film between a rigid quartz and a soft decane surface. For an uncharged quartz surface, they observed little change in the packing of water molecules and decane surfaces in a film of 2 to 3 water layers. On the other hand, for a charged quartz surface, they observed significant changes in the density of ions as the brine film was thinned. By inputting the calculated effective dielectric constant (smaller than the water bulk ε_0), the density profiles obtained with the PBE model were in better agreement with the MD density profile. Additionally, they demonstrated that the hydration (or structural) and the double electric layer contributions to the disjoining pressure are non-additive. This was clarified by the hydration force changing as the quartz surface becomes electrified.

Using Molecular Dynamics, Tian *et al.* [12] evaluated the wettability change with alteration in ionic strength in a system consisting of quartz/decane and decanoic acid mixture/brines. They observed three mechanisms: Cation bridging, EDL repulsion, and hydration repulsion. The two types of cations solutions studied exhibited different bridging effects between the oil and solid phases. While Ca^{2+} bridging was electrically neutral, K^+ bridging was negatively charged. As a result, the former tended to be more or less indifferent to changes in ionic strength, while the latter preferred an intermediate salt concentration. They also concluded that EDL repulsion and hydration repulsion dominate at low and high salinities, respectively. Therefore, to optimize brine composition, all three mechanisms should be considered.

The study of Mugele *et al.* [92] investigated the wettability of a solid/oil/brine system. The researchers employed pure decane as a model oil and used varying concentrations of two types of salt: Sodium and calcium chloride. They also examined two types of solid surfaces, namely silica and mica samples, with the latter repre-

senting clays. Their findings indicated that mica has a higher capacity to retain the oil phase compared to silica. In fact, no measurable contact angles were obtained when the silica surface was used. Calcium chloride enhanced the affinity with the oil phase. The measured brine film thicknesses between decane and mica showed a tendency to increase as the concentration of divalent salt diminished. Interestingly, even a highly concentrated monovalent cation solution resulted in a significant film thickness. To evaluate the effect of surface-active components, they added stearic acid to decane, which increased the spreading of the oil on the mica surface. Furthermore, the researchers derived a model similar to the disjoining pressure method, using the PBE. They applied the Neumann boundary condition, estimating the charge densities on mica and oil surfaces from zeta potential measurements. Notably, the minimum interaction potential for divalent salts occurred at smaller film thicknesses, whereas the opposite was observed for monovalent salts, with greater film thicknesses. The model demonstrated good agreement with the experimental data, indicating that monovalent cations solutions on both mica and silica surfaces result in small, negligible contact angles.

Kakati and Sangwai [23] conducted a study to evaluate the wettability of an oil/brine/quartz system using contact angle measurements. They investigated different aspects, among which salinity and composition of brines and different oil phases (pure alkanes and model oils, representing organic acid and basic compounds). Despite lying in a water-wet regime, wettability changes were observed with salinity alteration, particularly for divalent ions. A minimal wettability was reached at 0.1 M for all types of brines and oil phases. Specifically, for pure decane, CA varied less than 6 degrees in NaCl brines. The change in CA was attributed to the change in the liquid-liquid interfacial tensions. In contrast to pure alkanes, model oils allowed a wettability regime change from a water-wet to an intermediate-wet regime with varying ionic concentrations. Therefore, the presence of acid and basic components was an important evidence of the low-salinity waterflooding effects. Another important aspect is that the oil containing the amine group showed lesser CA, indicating a greater affinity of this phase for the solid.

Duffy *et al.*[32] studied the effect of temperature on the contact angle for a quartz/water/n-decane surface. They developed a capillary-based high-temperature apparatus to measure CA. Their findings revealed a linear dependency between contact angle and temperature. Using Young's equation, they demonstrated that interfacial tensions between solid and fluid phases were altered. Since viscous forces did not impact wetting behavior and the system did not contain electrolytes, the shift in the wettability was attributed to changes in van der Waals interactions and possibly polar or acid-base interactions between quartz and water. The researchers also pointed out that the increasing solubility at higher temperatures also reflects

changes in the interfacial tension between the solid and fluid phases.

Extending that study, Duffy *et al.* [17] applied the surface component approach to model the contact angles. In this method, the interfacial tension between the phases is calculated as the sum of van der Waals (including the Lifshitz approach) and acid-base (hydrogen-bonding) contributions. The CA is then computed from the Young equation. Notably, the model disregards the influence of the electrical double layer. They fitted literature dielectric data sets to obtain the temperature-dependent dielectric functions, which were used in the calculation of the Hamaker coefficient. The model proved to accurately represent the experimental data obtained in their previous study, and the other literature data for a different system.

Chapter 3

Materials and Methods

Here, we investigated a model system consisting of three phases: brine, oil, and rock. A quartz sample was selected as the solid phase to represent a sandstone reservoir. Brine solutions with varying concentrations of sodium chloride were prepared, and pure n-decane was used as the oil phase. Contact angles were measured using goniometry and calculated using a disjoining pressure approach based on the Poisson-Boltzmann equation. In order to demonstrate wettability change in a more complex system, simulations using crude oil as the oil phase were performed and compared to experimental literature data.

3.1   Experimental

3.1.1   Solid phase characterization

The quartz sample used in this study was obtained from previous work [93]. The sample had already been cut and polished using a 1 to 3 μm diamond suspension in a Struers Tegra polisher [93].

X-ray fluorescence (XRF) and X-ray diffraction (XRD) techniques were employed to confirm the sample composition. These analyses were conducted at the Laboratory of Hydrogen Technologies (LabTech) at COPPE/UFRJ. The sample was manually powered and subject to XRF analysis using a Rigaku Primini analyzer with a LiF crystal at 40kV and 1.25mA. A Rigaku MiniFlex II equipment equipped with a Cu X-ray tube was employed for the XRD analysis. The operation occurred at 30kV and 15mA. The diffraction angles were scanned from 5° to 90°, with a step size of 0.05° and a counting time of 1 second. Phase identification was performed using Profex, an open-source graphical user interface.

Surface morphology analysis was carried out using a ZEISS optical microscope at the Corrosion Laboratory (LabCorr) of the Metallurgical and Materials Engineering Program/UFRJ.

Atomic force microscopy (AFM) was employed to investigate the roughness and surface topography. This procedure was conducted using NT-MDT equipment at the Laboratory of Thermoanalysis and Rheology (LABTeR) of the School of Chemistry/UFRJ.

3.1.2 Cleaning and System Preparation

Solutions of sodium chloride (Vetec) with concentrations of 0, 2, 20, 200, and 1000 millimoles per liter were prepared using ultrapure water obtained from a Sartorius arium®mini equipment. The densities of these brine solutions and a 99% n-decane from Vetec were measured using an Anton Paar sound velocity and density meter at a temperature of 25°C.

Before each contact angle measurement, the quartz sample was subjected to a cleaning procedure involving sequential washing with pure acetone, ethanol, and ultrapure water. After that, the sample was stored in the brine solutions for 24 hours (saturation time), to approximate surface thermodynamic equilibrium. The pH of the brine solutions was measured before and after saturation, to observe any possible changes. A BEL W3B ph-meter was employed in this measurement.

3.1.3 Goniometry and Tensiometry

Contact angle measurements were conducted in a Dataphysics OCA model 15EC goniometer, which was coupled to a 7lab thermostatic bath, maintained at a temperature of 25.0 ±0.1°C. The captive bubble method was employed for these measurements [35]. The experimental setup consisted of a camera, a syringe, and a light source, as depicted in Figure 3.1. After saturation, a quartz cuvette was filled with the respective brine solution, and the solid surface was positioned at the top of the cuvette. Using a Hamilton syringe with a 0.52mm needle, 5 drops of 2 μl each of the oil phase were carefully deposited on the solid surface. Static contact angles were then measured by analyzing the projected images until equilibrium was approached. Each contact angle measurement was performed only after ensuring a minimum of 30 minutes of thermal equilibrium was reached before the placement of the drop.

Using the same equipment, interfacial tensions (IFTs) between brines and n-decane were measured (Figure 3.2). The Pendant drop bottom-up method, based on the Young-Laplace formulation (Equations 2.6 to 2.8), was employed for the IFTs measurements. Before each measurement, a thermal equilibrium of at least 30 minutes was ensured. The earlier measured densities were inputted into the software for the IFT calculation. 5 drops of 19 μl each of the oil phase were dispensed to compute the mean value.
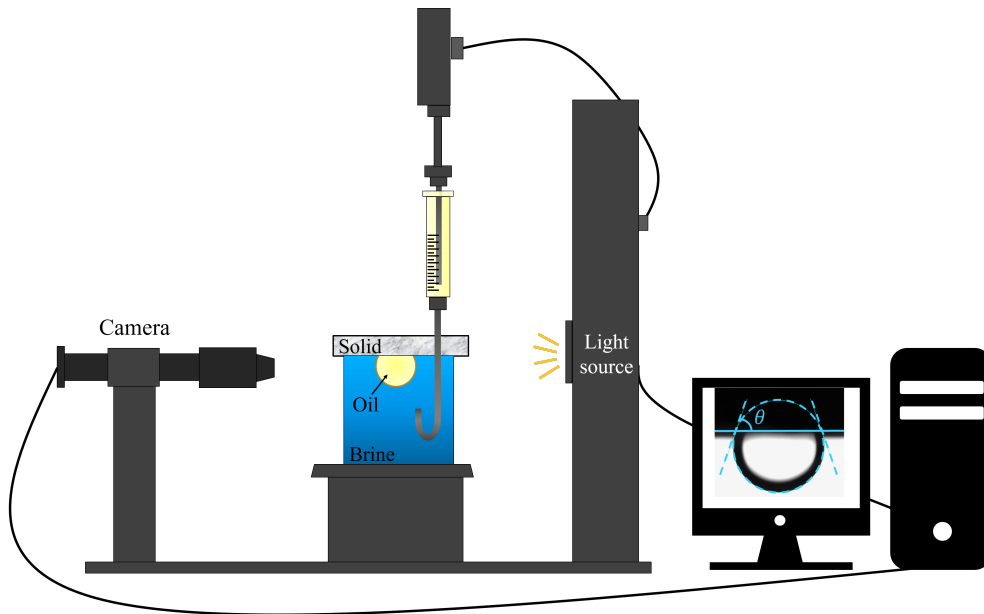
Figure 3.1: Contact Angle Measurement using the captive drop method in a Goniometer.
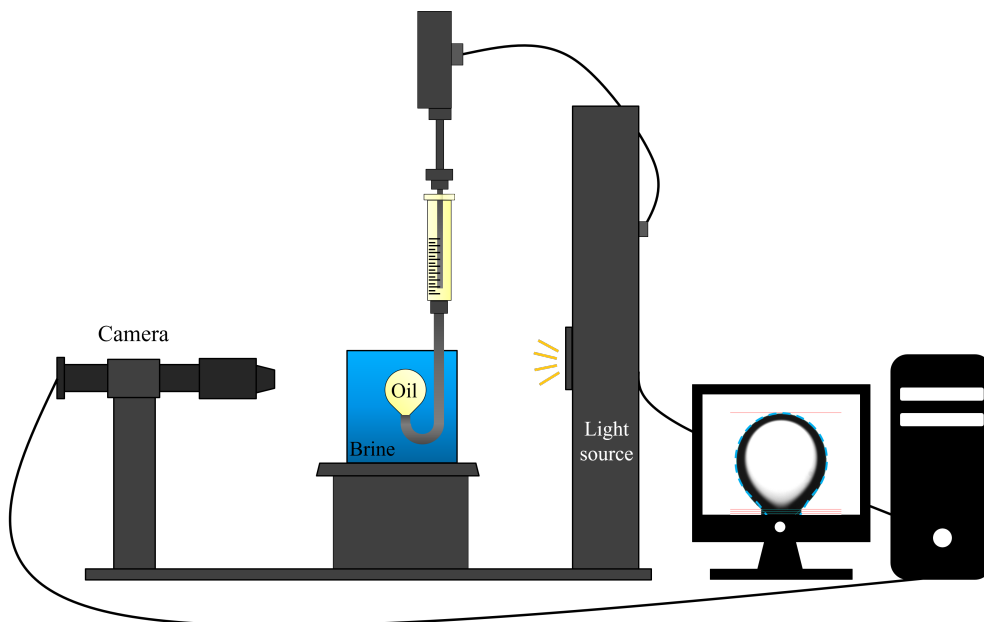
Figure 3.2: Interfacial tension measurement using the Pendant drop bottom-up method in a Goniometer.

3.2 Calculation

Figures 3.3 and 3.4 illustrate the model systems used in this work. The quartz and oil are considered flat surfaces, which are separated by a thin film of brine. The quartz surface undergoes charge regulation due to the dissociation and protonation of the silanol groups, while the n-decane surface is considered to be neutrally charged.
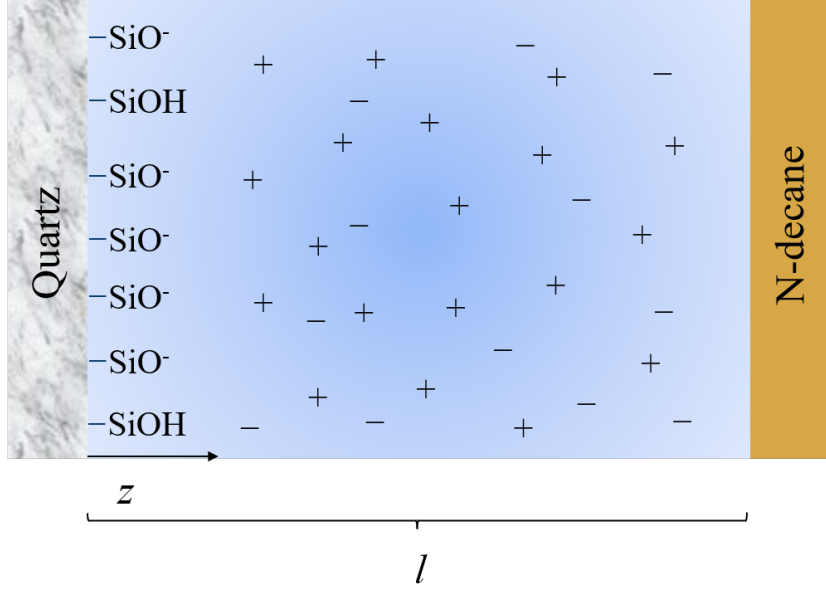
Figure 3.3: Scheme of the model system containing two flat surfaces (quartz and decane), separated by a thin brine film.

The crude oil phase is also described using a charge regulation model due to the dissociation and protonation of carboxylate and nitrogen base groups at the oil/brine interface. In the calculations, the ions are considered point charges without any volume, as assumed by PBE.

The algorithm used here (Figure 3.5) was adapted from the work of Barbosa [50]. It follows some steps, starting with the input of various parameters: temperature (T), the dielectric constant of the medium (ε), the bulk concentration of ions (ρ_i^b), ions valence (z_i), capillary pressure (p_c), interfacial tension between oil and brine (γ_{ob}), an initial guess for the film thickness (l^0), the surfaces parameters such as the density of sites (N_{max}), and equilibrium constants (pK_{eq}), as well as the Hamaker constants ($A_{\nu=0}$ and $A_{\nu>0}$). Then, the density profiles of ions are calculated by PBE using Robin boundary conditions for the quartz and crude oil surfaces and a Neumann boundary condition for the n-decane surface (which has a null fixed charge). PBE is solved using the finite volume method [47, 50].

Once the density profiles are obtained, the electrical double-layer component of the disjoining pressure is computed directly using Equation (2.44). After computing the van der Waals and structural components (Equations 2.45 and 2.46), the total disjoining pressure is compared to the capillary pressure. If Π is smaller than p_c, a decrease in the film thickness is applied until the capillary pressure is overcome. The equilibrium film thickness (l_{eq}) is then interpolated from the last two thicknesses, at which point the contact angle can be computed using Equation (2.42).
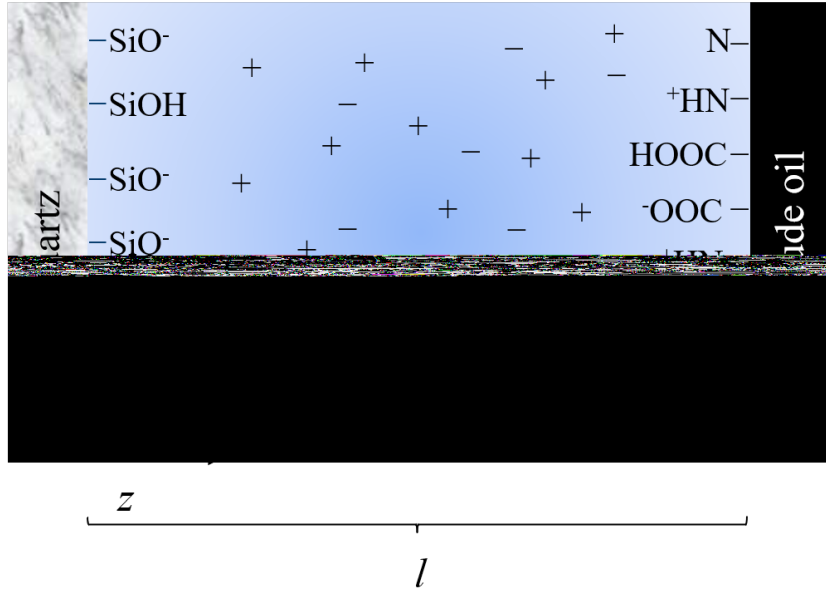
Figure 3.4: Scheme of the model system containing two flat surfaces (quartz and crude oil), separated by a thin brine film.
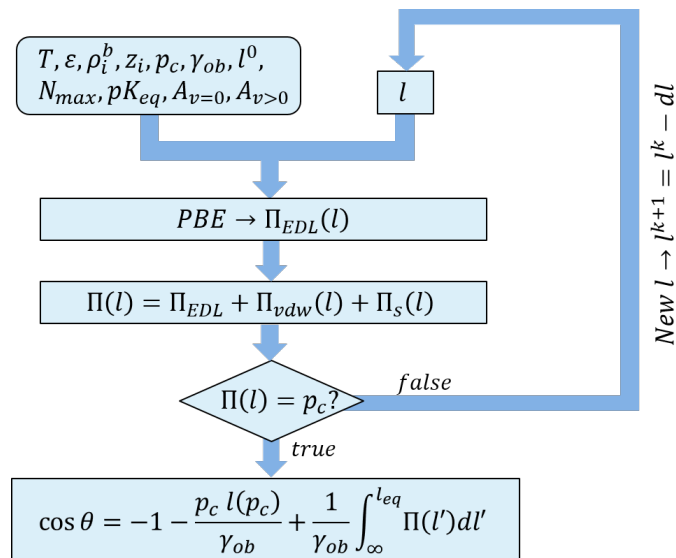

Figure 3.5: Algorithm for computing the contact angle from the disjoining pressure. Source: Adapted from [50].

3.2.1 Input parameters

As highlighted by Yates [94], soluble species can have an important effect in silica systems. pH, in particular, influences the solubility of α quartz, leading to the formation of different aqueous Si(IV) species, especially in the basic pH range. However, here the pH variation occurred within a range below 7.1, in which quartz solubility can be disregarded.

Silica surfaces have two types of hydroxyl groups: isolated and paired hydroxyl groups, which can interact through hydrogen bonding. Heating silica in a vacuum may promote a dehydration reaction, leading to the formation of stable siloxane groups. This may be responsible for some observed low surface densities of hydroxyl groups [94]. The value of 4.6 sites per nm^2, the most reported value by literature [95–102], will be employed in Equation (2.30).

For the silica surface, different surface reactions can be considered in the surface complexation model, including even cation adsorption/desorption, as in a Stern electric double-layer model [103–106]. The most probable protonation/deprotonation reaction of the silanol groups is shown in Equation (3.1) [103], which will be used in this work. Following Hiemstra *et al.* [103], the value of 7.5 was employed as the pK.

$$> SiOH \leftrightarrows \; > SiO^- + H^+ \qquad K_1 \tag{3.1}$$

The surface charge of the crude oil can be determined by considering the carboxylic acids and nitrogen bases groups surface reactions, as shown in Equations 3.2 and 3.3 [28, 107]. Following the work of Brady and Krumhansl [107], the density of sites for each surface group is assumed to be 1.67μmoles per m^2, and the logarithmic equilibrium constants of 5.0 and 6.0 are used for the carboxylic acids and nitrogen bases reactions, respectively.

$$> COOH \leftrightarrows \; > COO^- + H^+ \qquad K_2 \tag{3.2}$$

$$> NH^+ \leftrightarrows \; > N + H^+ \qquad K_3 \tag{3.3}$$
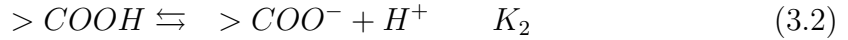
Considering the above-mentioned reactions, the procedure described in section 2.6.1 yields Equations (3.4) and (3.5) for the calculation of quartz and crude oil charge densities, respectively.

$$Q_{quartz} = \frac{-eK_1 N_{SiOH}}{K_1 + \rho_{H^+}|_{quartz}} \tag{3.4}$$

$$Q_{oil} = -e \left(\frac{K_2 N_{COOH}}{K_2 + \rho_{H^+}|_{oil}} - \frac{\rho_{H^+} N_N}{K_3 + \rho_{H^+}|_{oil}} \right) \tag{3.5}$$

Equation (2.33) was used for calculating the Hamaker constants. Table 3.1 presents the refractive indexes and dielectric constants of the three phases employed in this calculation. Since the screening of electrolytes on the Hamaker constant is already accounted for Equation (2.34), the dielectric constant of pure water (78.5) [45] was used in the calculations.

Table 3.1: Optical properties of the three phases of the system.

Parameter	Quartz	Water	N-decane	Crude oil
Refractive index (n_i)	1.536^a	1.333^b	1.406^c	1.455^d
Dielectric constant (ε_i)	4.29^a	78.5^b	2.0^c	1.925^d

[a] Properties from [108].
[b] Properties from [45].
[c] Properties from [17].
[d] Properties from [109].

The calculated $A_{\nu=0}$ and $A_{\nu>0}$ between quartz and n-decane were 2.630×10^{-21} J and 3.923×10^{-21} J, respectively. For crude oil, they were calculated as 2.635×10^{-21} J and 6.493×10^{-21} J, respectively.

In crude oil simulations, interfacial tensions were interpolated from the experimental data obtained in the work of Nicolini [93]. pH was maintained at 6 to find the vdW constant that provided the best fit to the experimental data. Once this constant was determined, the effect of pH alterations was further investigated.

Sadeqi-Moqadam et al. [72] demonstrated that a change in capillary pressure from 2 to 200kPa did not affect contact angle significantly. Some simulations were carried out for capillary pressures in the range of 0.06 to 5 bar, resulting in a coefficient of variation of less than 0.06% in the CA. Therefore, following the approach of Barbosa [50], the value of 0.3 bar was chosen.

Table 3.2 summarizes the input parameters used in the simulations.

Table 3.2: Summary of the simulation input parameters.

Parameter	Quartz/Decane/Brine	Quartz/Crude oil/Brine
N_{SiOH}	4.6 sites/nm^2 [a]	
N_{COOH}	-	1.0 sites/nm^2 [b]
N_N	-	1.0 sites/nm^2 [b]
pK_1	7.5[c]	
pK_2	-	5.0[b]
pK_3	-	6.0[b]
pH	6.87	6.0
$A_{\nu>0}$	3.923×10^{-21}J[d]	6.493×10^{-21}J[d]
$A_{\nu>0}$	3.923×10^{-21}J[d]	6.493×10^{-21}J[d]
Capillary pressure	0.3 bar	
Temperature	275.15 K	

[a] Property from [95].

[b] Properties from [107].

[c] Properties from [103].

[d] Calculated with Equation (2.33).

Chapter 4

Results and Discussion

4.1 Solid characterization

The analysis of the quartz diffractogram allowed the identification of a single phase, which was consistent with the quartz pattern of the Profex database (Figure 4.1). The main elements quantified by XRF analysis (Table 4.1) were silicon (Si) and oxygen (O), corresponding to a composition of 98.11% of SiO_2.
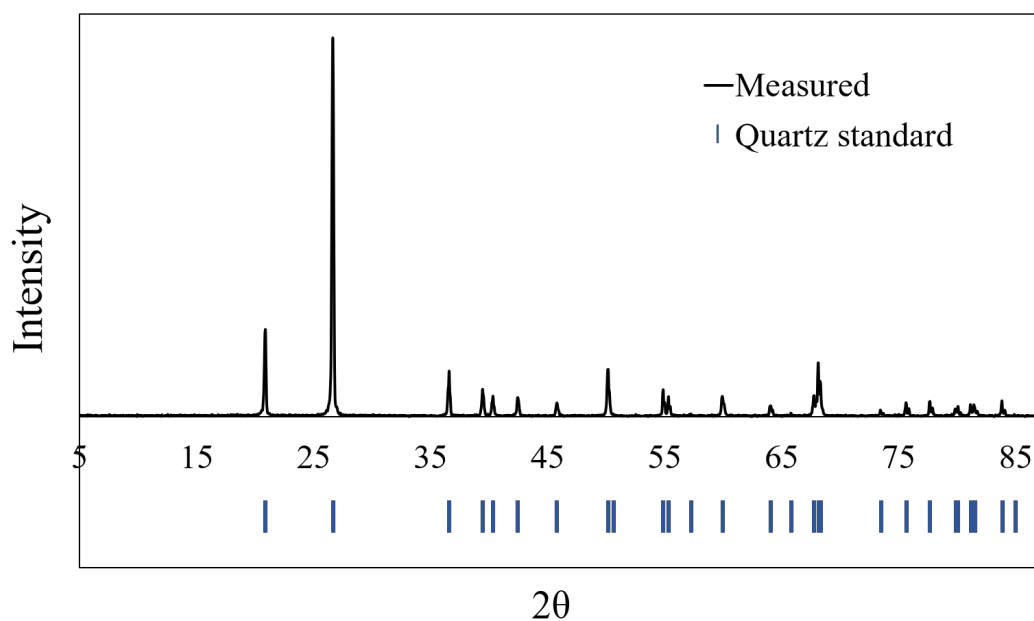
Figure 4.1: Diffractogram of the quartz sample.

Table 4.1: Quartz sample composition determined with XRF analysis.

Element	Composition (% m/m)
O	52.9323
Si	45.8605
Al	0.3475
Ca	0.2662
Fe	0.1837
Ag	0.1567
K	0.1151
S	0.1021
Cl	0.0360

Figure 4.2 exhibits a relatively homogeneous and smooth surface, along with some minor polishing scratches.
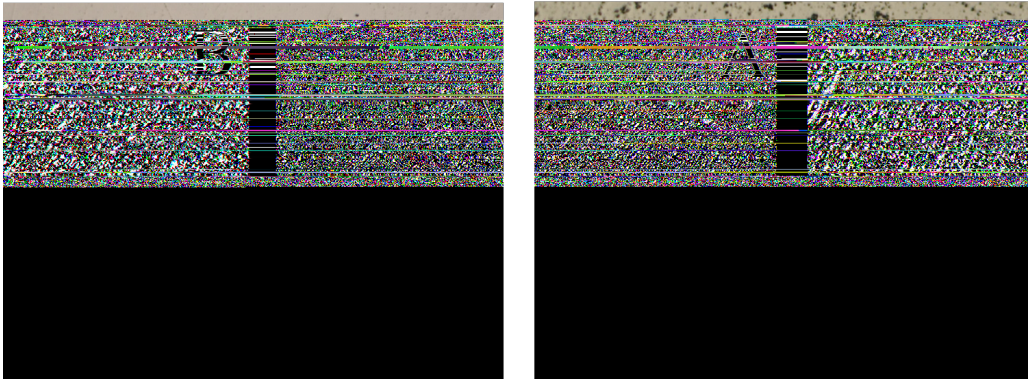
Figure 4.2: Optical microscopy images of the quartz sample at 200x (A) and 1012x (B).

Figures 4.3 and 4.4 show the quartz topography obtained using atomic force microscopy, confirming the observed previously smoothness. In Table 4.2, the main surface parameters obtained from this technique are presented.

4. 1F:Height
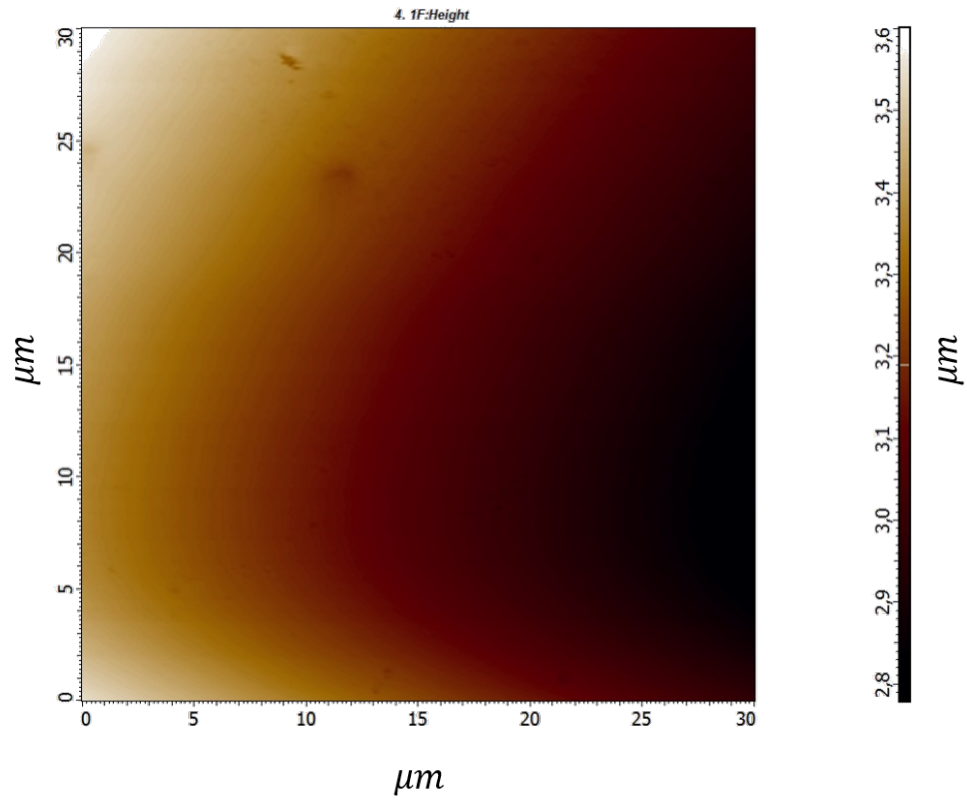
Figure 4.3: Quartz 2D surface obtained using atomic force microscopy.
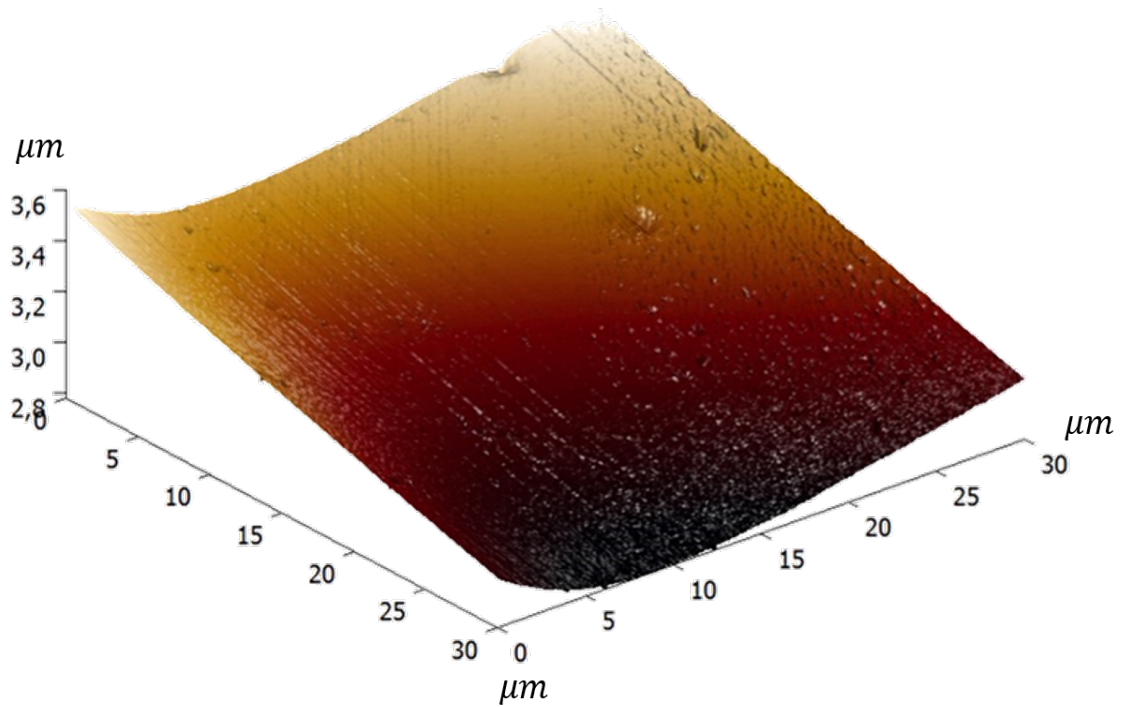
Figure 4.4: Quartz surface topography obtained using atomic force microscopy.

Table 4.2: Quartz roughness parameters obtained from AFM measurements.

Parameter	Value
Arithmetical mean deviation (Ra)	8.277nm
Root-mean-square deviation (Rq)	9.627nm
Maximum height (Rz)	39.646 nm
Projected area	900.240 μm^2
Surface area	900.773 μm^2

According to Equation(2.2), the calculated roughness factor was 1.001. Therefore, all these results affirm the applicability of Young's Equation (Equation 2.1) in describing the contact angle.

4.2 Fluid-fluid interactions

The variance analysis of the measured interfacial tension values is presented in Table 4.3, indicating a significant difference in all measured IFT within a 95% confidence interval. However, from 2 to 200mM, they were found to be equal (Table 4.4). This suggests that the ionic force within this range does not substantially alter the interfacial tension; in other words, fluid-fluid interactions remain unmodified.

Table 4.3: Analysis of Variance of IFT in brines with concentrations ranging from 0 to 1000mM.

Source of variation	SS	df	MS	F	P-value
Between groups	99.25	4	24.81	131.99	4.46×10^{-14}
Within groups	3.76	20	0.188		
Total	103.01	24			

SS=Sum of Squares, df= degrees of freedom, MS= Mean Squares.

F= variation between sample means/ variation within the samples.

P-value= probability of finding the observed results if the mean values were equal.

Table 4.4: Analysis of Variance of IFT in brines with concentrations ranging from 2 to 200mM.

Source of variation	SS	df	MS	F	P-value
Between groups	0.49	2	0.25	0.80	0.47
Within groups	3.69	12	0.31		
Total	4.18	14			

Figure 4.5 shows the interfacial tension results obtained at 25 ± 0.1°C for the n-decane/brine interface, as well as published values for similar systems [110–117].

For the interface between pure water and decane, our results are similar to the literature values. The number of studies evaluating the effect of the salinity on the IFT of decane/brine is very limited, and this effect remains uncertain. Aveyard and Saleem [117] found the IFT to increase with increasing NaCl concentration, while Sayed *et al.* [114] observed a decrease in the IFT for an intermediate concentration. Using Molecular Dynamics, Zhao *et al.* [87] observed a minimum IFT at 200mM, while Jiménez-Ángeles and Firoozabadi [118] showed an increase in the IFT with the increase in salt concentration. At lower salt concentration, our results agree with the decrease in the IFT. Therefore, further investigation is suggested to better understand this effect.
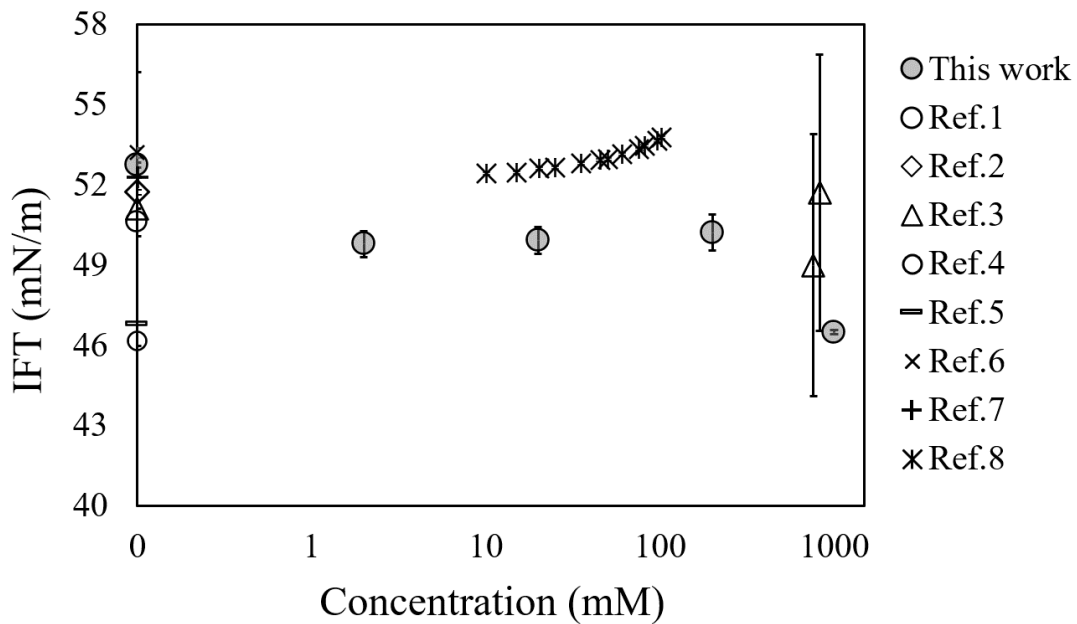
Figure 4.5: Effect of salinity on the interfacial tension between brine and n-decane. Experimental data from Ref.1 - Jennings and Newman [112], Ref.2 - Velusamy *et al.* [113], Ref.3 - Sayed *et al.* [114], Ref.4 - Adewunmi and Kamal [111], Ref.5 - Michaels and Hauser [110], Ref.6 - Goebel and Lunkenheimer [115], Ref.7 - Aveyard and Haydon [116] and Ref.8 - obtained by summing the IFT value from Aveyard and Haydon [116] with the increments in IFT from Aveyard and Saleem [117].

4.3   Fluid-solid interactions

The pH measurements of the aqueous solutions before and after quartz saturation did not vary significantly, indicating no detectable bulk effect (Figure 4.6). The final pH values for brines ranging from 0 to 1000mM varied from 6.54 to 7.14. Therefore, the average value of 6.87±0.26 was employed in the simulations.
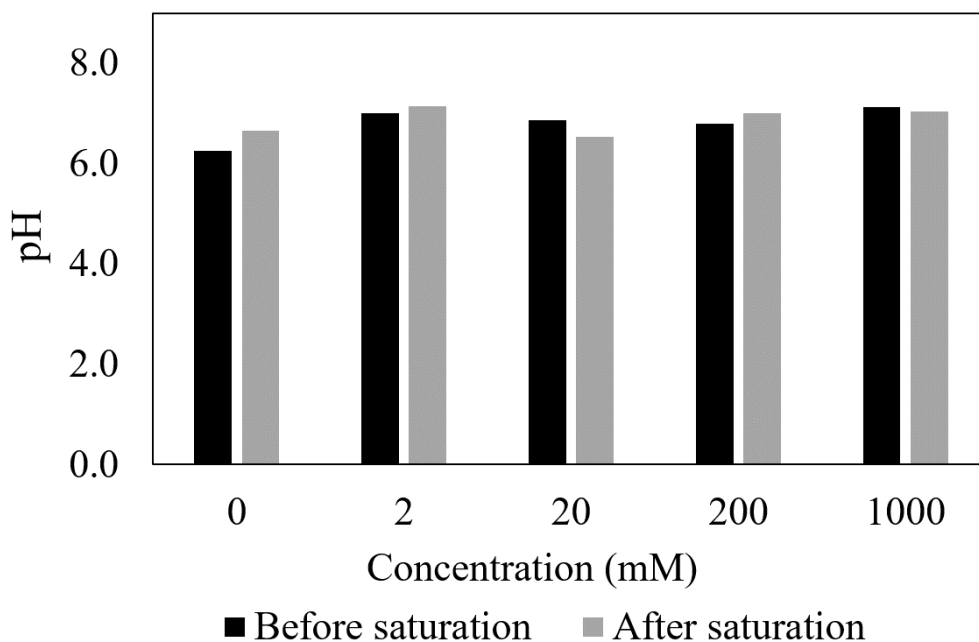
Figure 4.6: Brines pH variation after 24h of saturation with quartz.

Figure 4.7 exhibits the oil contact angles measured at 25 ±0.1°C between decane/quartz/brine, along with previously published values for similar systems [23, 32, 113]. Despite observing the same wettability regime (water-wet) in all works, the measured values significantly deviated from those reported in the literature. Some factors could contribute to these discrepancies, such as impurities, roughness, and variations in measurement conditions. If impurities were present, it would be expected to impact the interfacial tensions between brine and oil, resulting in significant deviations from literature values. However, this effect was not observed. As discussed in Chapter 2, contact angles are influenced by surface roughness. For CAs greater than 90°, Equation (2.3) yields larger apparent angles. Unfortunately, none of the published studies provided information on roughness, making it challenging to compare the results. Besides, measurements of Duffy *et al.* were conducted at higher pressure (69bar), although other studies have shown a minor influence of pressure on CA in crude oil systems [30, 31, 33]. Lastly, Kakati and Sangwai [23] employed an oil drop of 50μl, which is significantly larger than the recommended range for the captive drop method of 1 to 3 μl. This raises the possibility of gravitational effects that may not be negligible.
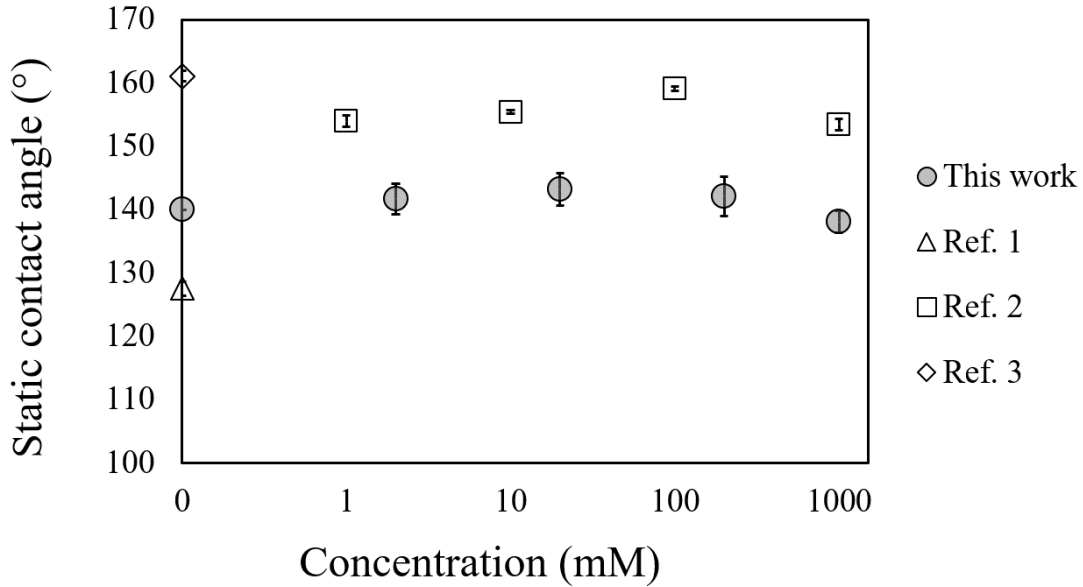
Figure 4.7: Effect of salinity on the contact angle in the system quartz/decane/brine. Experimental data from: Ref.1 - Velusamy *et al.* [113], Ref.2 - Kakati and Sangwai [23], and Ref.3 - Duffy *et al.* (69 bar) [32].

The results of this study exhibit similarities and differences when compared to the findings of Mugele *et al.* [92], who investigated a similar system. The authors showed that the drops of sodium chloride solutions of various concentrations spread almost completely on a silica surface immersed in a decane solution, resulting in contact angles nearly unmeasurable. This indicates that the contact angles measured from the oil phase were approximately 180 ° for the entire range of salinity studied. While their results agree with the water-wettability preference of a silicate surface, the discrepancy from this study may be attributed to differences in the silanol surface site densities of the solid phases, which was an amorphous silicon oxide layer in their study.

The mean contact angles from 0 to 1000mM presented a significant difference within a 95% confidence interval, as shown in Table 4.5. No significant difference was observed in the contact angles of brines ranging from 2 to 200 mM (Table 4.6), as well as in the CAs at 0 and 1000mM (Table 4.7). Consequently, the CA initially increases with an increase in salinity but is followed by a subsequent decrease. The maximum contact angle observed between 0 and 1000 mM suggests the reduction of affinity of the oil phase with the surface within this specific salinity range. These results support the utilization of low-salinity waterflooding to enhance oil recovery. The recognized low-salinity range in the literature typically falls between 1000 and 5000ppm [11]. In this study, among the investigated concentrations, 20mM (approximately 1170 ppm) would fall within this range.

Table 4.5: Analysis of Variance of CA in brines with concentrations ranging from 0 to 1000mM.

Source of variation	SS	df	MS	F	P-value
Between groups	80.98	4	20.24	3.69	0.021
Within groups	109.64	20	5.48		
Total	190.61	24			

Table 4.6: Analysis of Variance of CA in brines with concentrations ranging from 2 to 200mM.

Source of variation	SS	df	MS	F	P-value
Between groups	5.94	2	2.97	0.46	0.64
Within groups	77.15	12	6.43		
Total	83.08	14			

Table 4.7: Analysis of Variance of CA in brines with concentrations of 0 and 1000mM.

Source of variation	SS	df	MS	F	P-value
Between groups	8.93	1	8.93	2.20	0.18
Within groups	32.49	8	4.06		
Total	41.42	9			

However, despite observing this behavior, the variation in the contact angle was not expressive. This result aligns with the literature data presented in Figure 4.7. Another aspect that should be discussed is the impact of variation in fluid-fluid interactions on the CA. In Young's equation (Equation 2.1), if the interfacial tensions between the solid phase and fluids were influenced by brine ionic strength, the quantity $\gamma_{ob} \cos \theta$ would also change accordingly. Yet, according to Tables 4.8 and 4.9, the interactions between the solid and the fluids only exhibited a significant change in pure water compared to the other solutions. As Lyu *et al.*[11] highlighted, the low-salinity effects are not well observed for oils lacking polar compounds, which is the case of n-decane. Therefore, the influence of brine salinity on quartz wettability was not very evident for this specific system.

Table 4.8: Influence of salinity on the fluid-fluid and fluids-solid interactions.

Concentration (mM)	θ (°)	γ_{ob} (mN m^{-1})	$\gamma_{ob} \cos\theta$
0	140.0 ± 2.4	52.8 ± 0.1	-35.6 ± 1.3
2	141.7 ± 2.6	49.8 ± 0.5	-39.4 ± 1.4
20	143.2 ± 3.2	49.9 ± 0.5	-39.9 ± 1.6
200	142.1 ± 1.7	50.2 ± 0.7	-39.3 ± 0.9
1000	138.1 ± 1.5	46.5 ± 0.1	-39.2 ± 0.9

Table 4.9: Analysis of Variance of $\gamma_{ob} \cos\theta$ in brines with concentration ranging from 0 to 1000mM.

Source of variation	SS	df	MS	F	P-value
Between groups	62.1	4	15.5	9.9	0.0001
Within groups	31.2	20	1.6		
Total	93.3	24			

4.4 Calculations of Quartz/Brine/Decane Systems

Figure 4.8 shows the simulated charge densities of the quartz surface for various brine solutions as a function of the film thickness (L). As explained previously, the two smallest film thickness correspond to the values used to calculate the equilibrium equilibrium. Notably, the equilibrium thicknesses for brines of 2 and 20 mM were significantly larger compared to the others. As expected, quartz kept a negative surface charge when in contact with all brines. Moreover, the absolute charge density increased with higher salinity. As Equation (2.30) indicates, the absolute charge density is inversely proportional to the concentration of H$^+$ ions near the quartz surface. Therefore, the calculated charge density precisely represents the decreasing profile of the concentration of these ions at the solid surface as the salinity increases (see Figure 4.9). Although somewhat counterintuitive, this result is attributed to the entropic effect between the cations. In these films, if the salt concentration increases, a "competition" between H$^+$ and Na$^+$ ions to screen the electrostatic potential occurs. As a consequence, it leads to the deprotonation of the quartz surface.
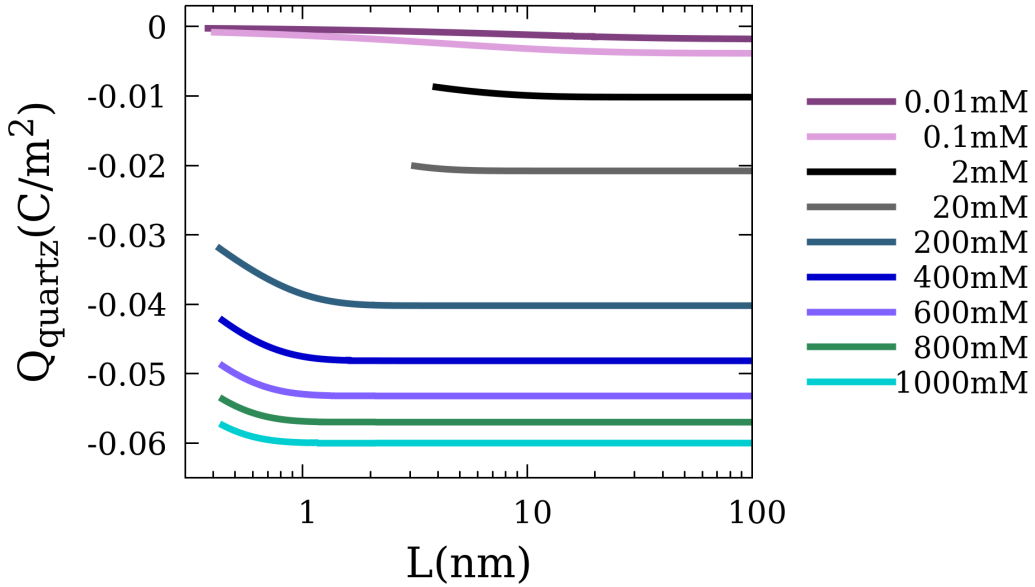
Figure 4.8: Quartz surface charge density simulated for different film thicknesses (L) and different electrolyte concentrations in the quartz/brine/decane system.
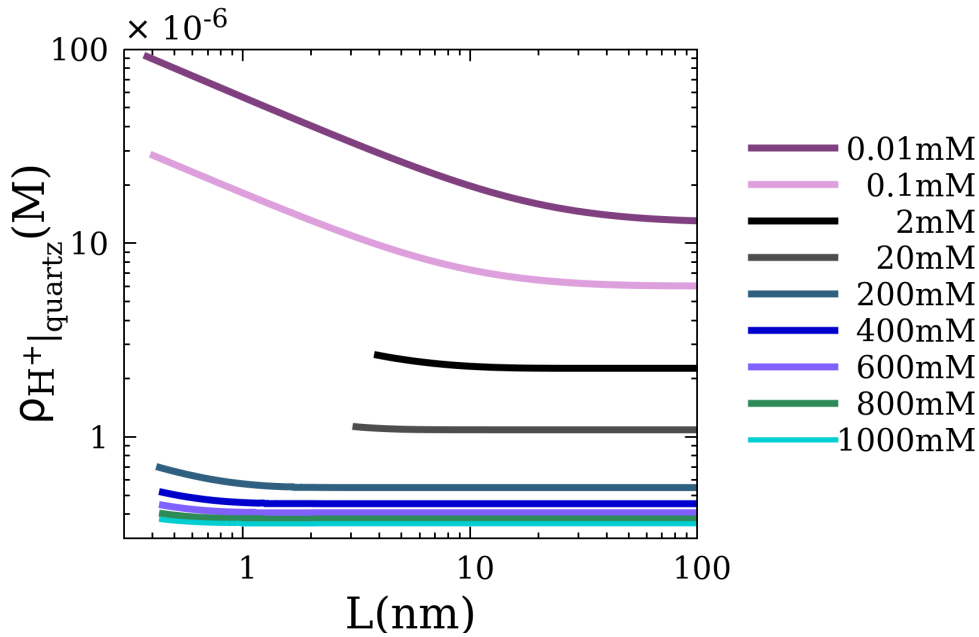

Figure 4.9: Concentration of cations H^+ on the quartz surface for different film thicknesses (L) and different electrolyte concentrations in the quartz/brine/decane system.

Furthermore, it is observed that below a certain film thickness, the absolute surface charge density decreases with decreasing film thickness. This occurs because there is an increase in the concentration of H^+ ions in the film, leading to a more protonated quartz surface. As the film thickness increases, the concentration of H^+ gradually decreases until reaching a fixed concentration limit. As a result, the magnitude of the charge density diminishes and becomes practically invariant. Notably,

the thickness at which the charge density stabilizes is smaller as the salinity of the aqueous medium increases, which implies that higher electrolyte concentrations result in a steeper decay of the effective interaction between the surface sites of the quartz and the H^+ ions.

The mean electrostatic potential (MEP) profiles along the equilibrium film thickness for different brines are shown in Figure 4.10. To facilitate comparisons, the distance along the film was normalized by the equilibrium film thickness. The quartz and n-decane surfaces are located at distances of 0 and maximum normalized film thickness, respectively, indicating that the electrostatic potential remains negative at the n-decane surface. Additionally, at the equilibrium film thickness, the lower the salinity, the greater the absolute MEP. This trend could be attributed to the ion screening effects; however, as it will be seen further, the calculated equilibrium film sizes exhibited a great variation (Figure 4.12). Since the interaction potential also depends on the separation distance [14], a more appropriate evaluation of this effect can be demonstrated in Figure 4.11, where the largest calculated film thickness (38 nm) was employed.
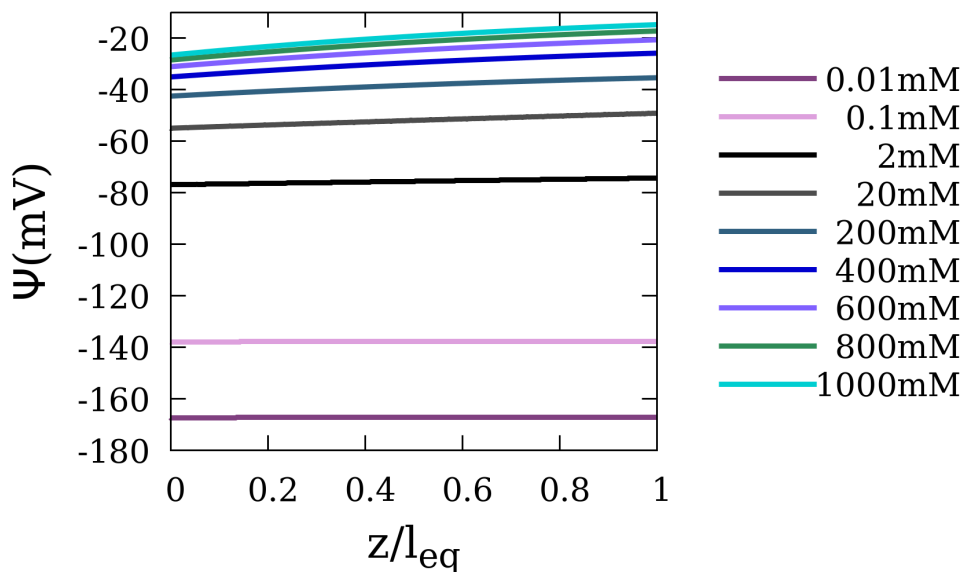

Figure 4.10: Calculated mean electrostatic potential for the different electrolyte concentrations. The quartz and n-decane surfaces are located at distances of 0 and maximum normalized film thickness, respectively.
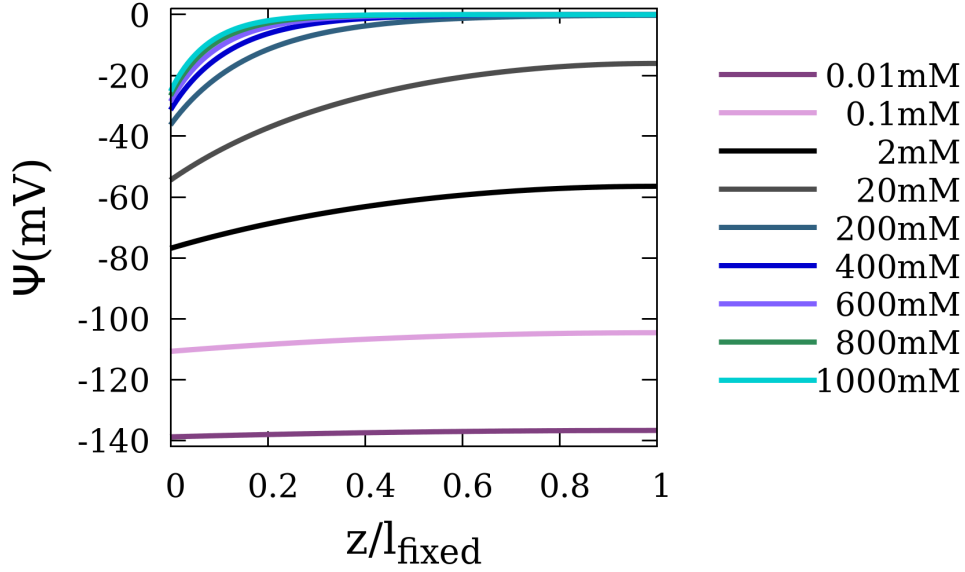
Figure 4.11: Calculated mean electrostatic potential for the different electrolyte concentrations at a fixed film thickness (l_{fixed}) of 38 nm. The quartz and n-decane surfaces are located at distances of 0 and l_{fixed}, respectively.

Furthermore, in Figure 4.10, the derivative of the mean electrostatic potential concerning the distance increases as the brine salinity rises. This indicates that for the low-salinity brines, at the equilibrium distances, the electrostatic potential is not effectively screened. As we will seen later, this will directly impact the electric double-layer disjoining pressure component.

Figure 4.12 illustrates the ion density profiles along the equilibrium film thickness for the various brines. The cations exhibit a higher affinity for the quartz surface, whereas the anions interact stronger with the n-decane surface. However, cations concentration at the n-decane surface is much higher than anions concentration. This behavior can be attributed to the electrostatic potential pattern (Figure 4.10), which shows that the MEP remains highly negative at the decane surface. Only sodium ions become adsorbed in the film, while the other ions are depleted. This finding agrees with the observations of Fang *et al.* [84], where the density of chloride anions is very small between the charged quartz and the uncharged decane surface.
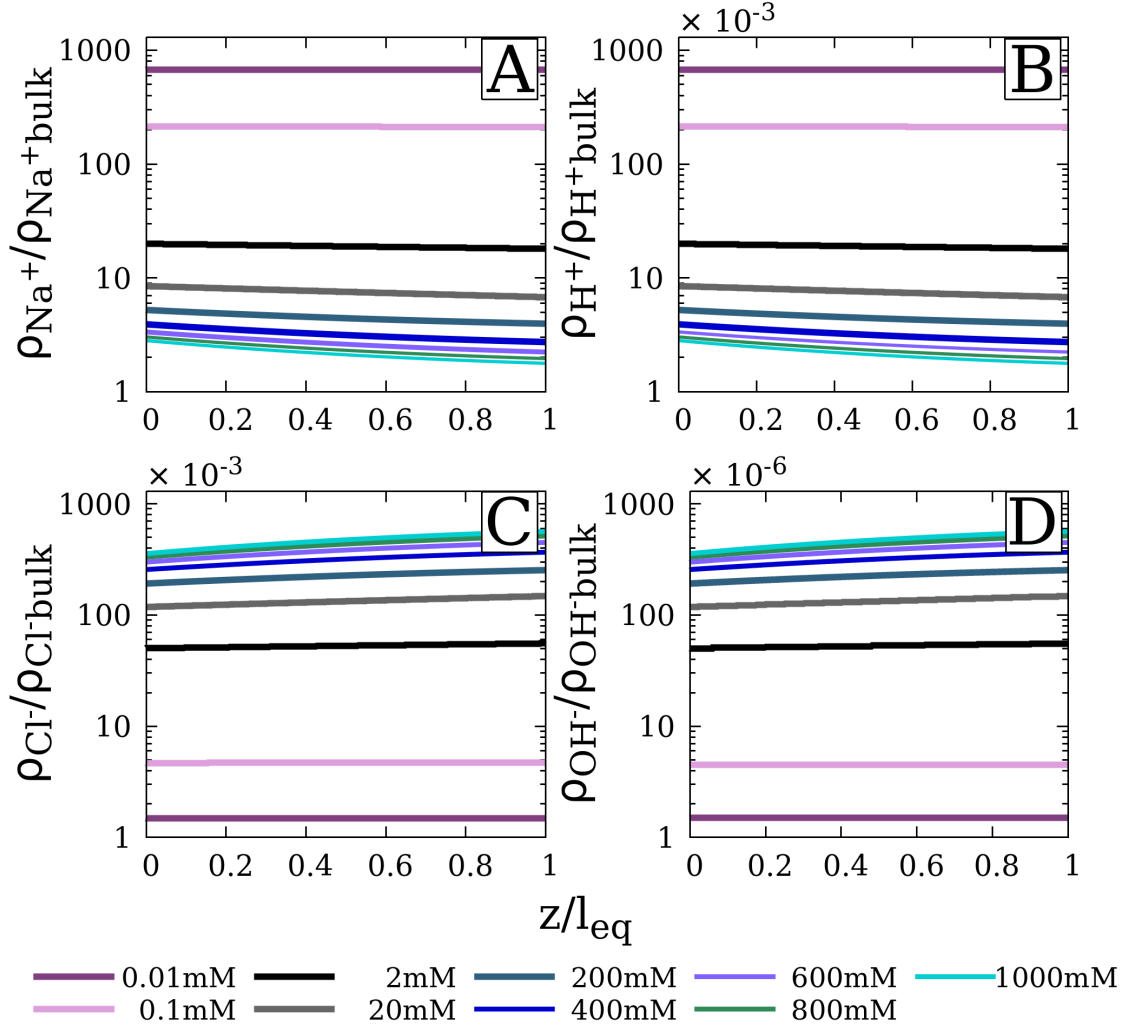
Figure 4.12: Ion density profiles at equilibrium film thicknesses for the different bulk electrolyte concentrations: A) Na^+, B) H^+, C) Cl^-,and D) OH^- .The quartz and n-decane surfaces are located at distances of 0 and maximum normalized film thickness, respectively.

The components of the simulated disjoining pressure (DP) are presented in Figure 4.13. As explained previously, simulations were performed from an initial film size guess, which was diminished until the total DP reached 0.3 bar. Therefore, the two lowest distances in Figure 4.13 correspond to the thicknesses from which the equilibrium distance was interpolated. As expected, the electrical and structural contributions to the disjoining pressure exhibit repulsive behavior, while the van der Waals contributions are attractive. All absolute DP components exhibit the same order of magnitude. Even considering the influence of electrolytes on the Hamaker constant (Equation 2.34), changes in salt concentration do not significantly impact the van der Waals contributions to the disjoining pressure. Therefore, variations in the total disjoining pressure among the different brine solutions can be attributed to the double-layer contribution. For the concentrations of 0.01 and 0.1 mM, the EDL

disjoining pressures were significantly smaller, even at smaller film thicknesses. In these brines, the MEP was less effectively ion-screened, leading to a decrease in the first term on the right side of Equation (2.44), as explained earlier. Specifically, for concentrations of 2 and 20 mM, the total disjoining pressure was found to be positive throughout the system, indicating a purely repulsive behavior. Consequently, the integral term in Equation 2.42 becomes negative, resulting in undefined contact angles in these systems, which indicates the complete wetting of the surface by the aqueous phase. Additionally, for a fixed thickness, we observe the rise of the disjoining pressure as the salinity decreases. This agrees with the results of Fang *et al.*[84], and supports the role of the electric double-layer mechanism in wettability alteration.

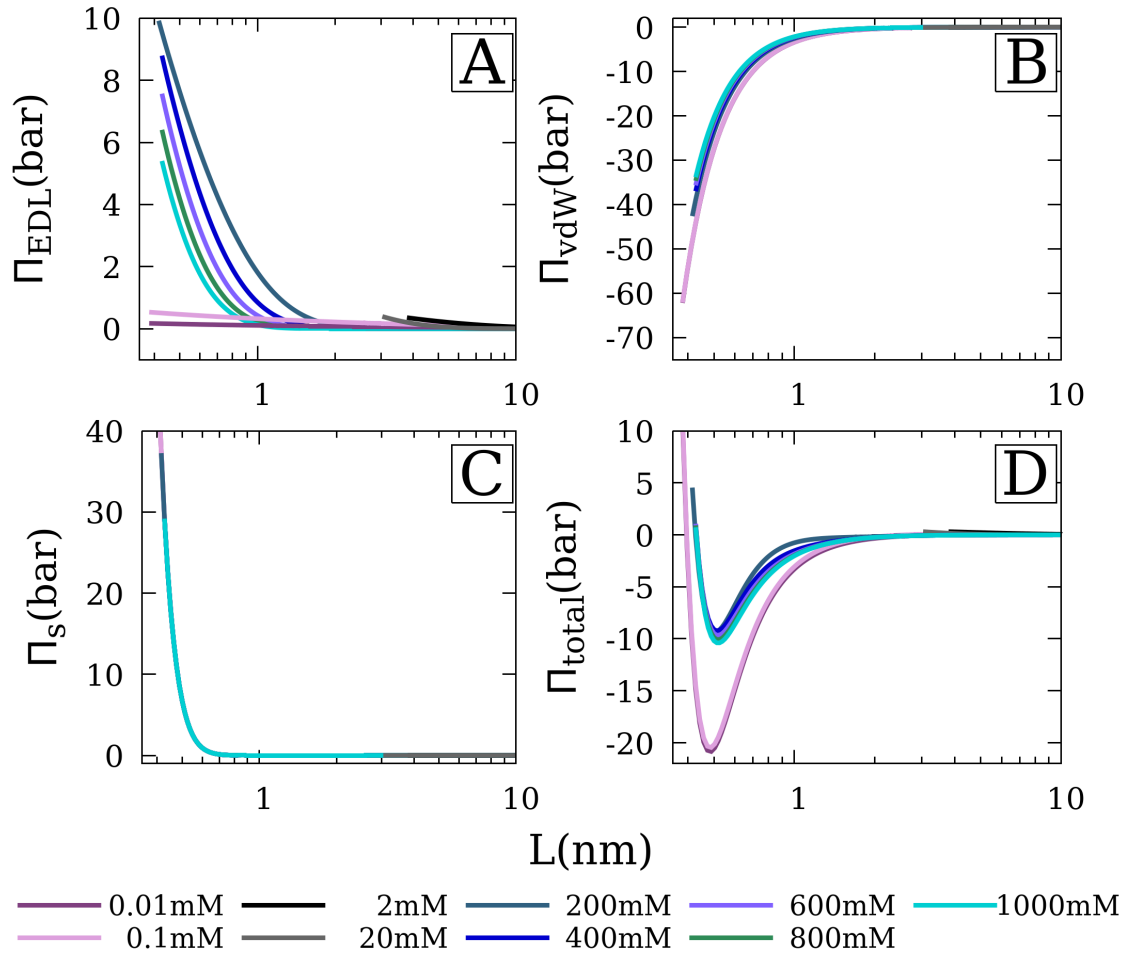Figure 4.13: Disjoining pressure (Π) contributions: (A) Double layer, (B) van der Waals, (C) structural, and (D) total disjoining pressure for different brines as a function of film thickness (L) between quartz and n-decane surfaces.

Figure 4.14 shows the calculated equilibrium thicknesses. For brines with concentrations between 1.2 and 92mM, the film thicknesses were significantly larger,

indicating the presence of strong repulsive forces within the system. As pointed out by Ding and Rahman [119], increasing the brine film thickness is desired because it can enhance oil mobility and further increase oil recovery. Therefore, the use of water within a specific range of salinity for this purpose is confirmed.
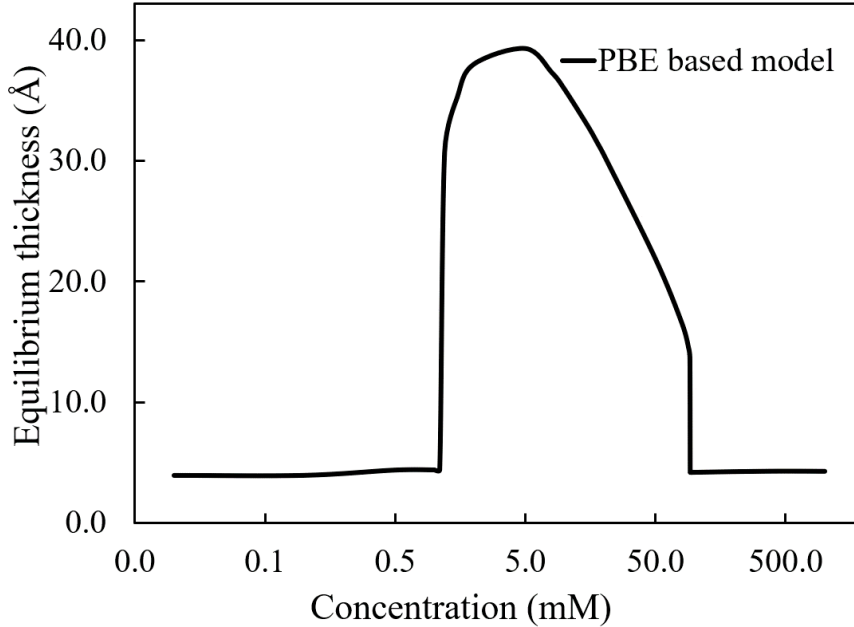

Figure 4.14: Film equilibrium thicknesses (L) as a function of the electrolyte concentration in the system quartz/brine/decane.

Figure 4.15 presents the simulated and experimental contact angles. The reduction in the wettability of the solid by the oil phase as the ionic force decreases aligns with the well-established concept of low-salinity waterflooding. Between 1.2 and 92mM, the strong electrical repulsion led the macroscopic contact angles to become parallel to the solid phase, and the film wets the surface thoroughly, causing the oil phase to be detached [14, 71]. Importantly, the water-wet state extends over a wider concentration range (around 70 to 5400ppm) than the reported in the literature (1000 to 5000 ppm) [11]. Furthermore, outside that concentration range, a slight variation in the contact angle is observed, as expected for a system containing a non-polar oil [11].
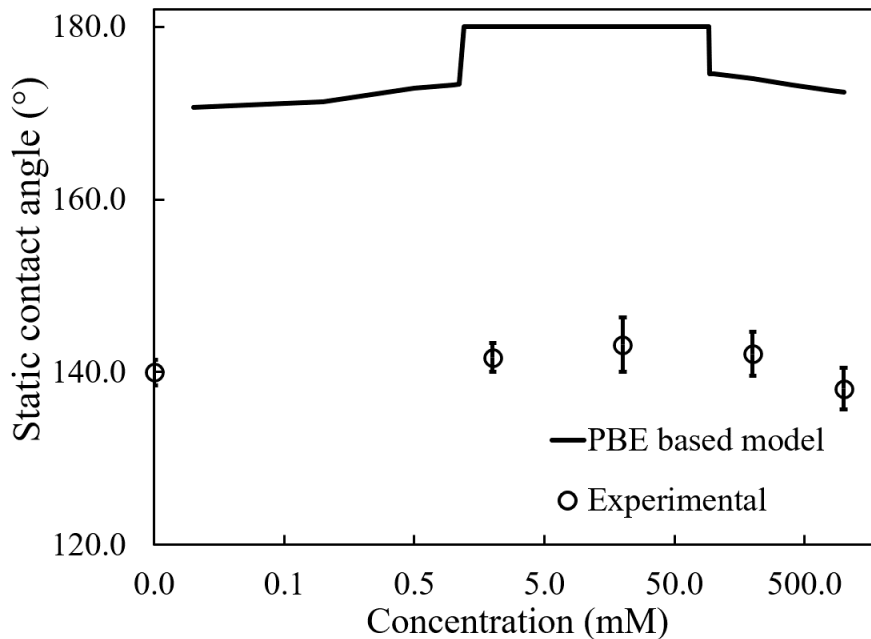
Figure 4.15: Experimental and calculated contact angles using the PBE model as function of the electrolyte concentration in the system quartz/brine/decane.

Unfortunately, the calculated CAs disagreed with the experimental ones. The Lifshitz theory is based on a continuum approach, in which intensive physical properties remain unchanged throughout the phase. However, at the molecular level, optical properties can fluctuate up to the interface [25, 45, 84]. Consequently, on this size scale, Equation (2.33) may fail to provide a complete description of the dispersion interactions when bulk optical properties are employed. As pointed out by Israelachvili [45], $A_{\nu=0}$ cannot exceed $\frac{3}{4}k_B T$ (3.09×10^{-21}J at 298.15K), but $A_{\nu>0}$ can be very high if one of the media has a significant refractive index. Therefore, additional simulations were conducted by increasing the $A_{\nu>0}$ coefficient. These results are presented in Figure 4.16.
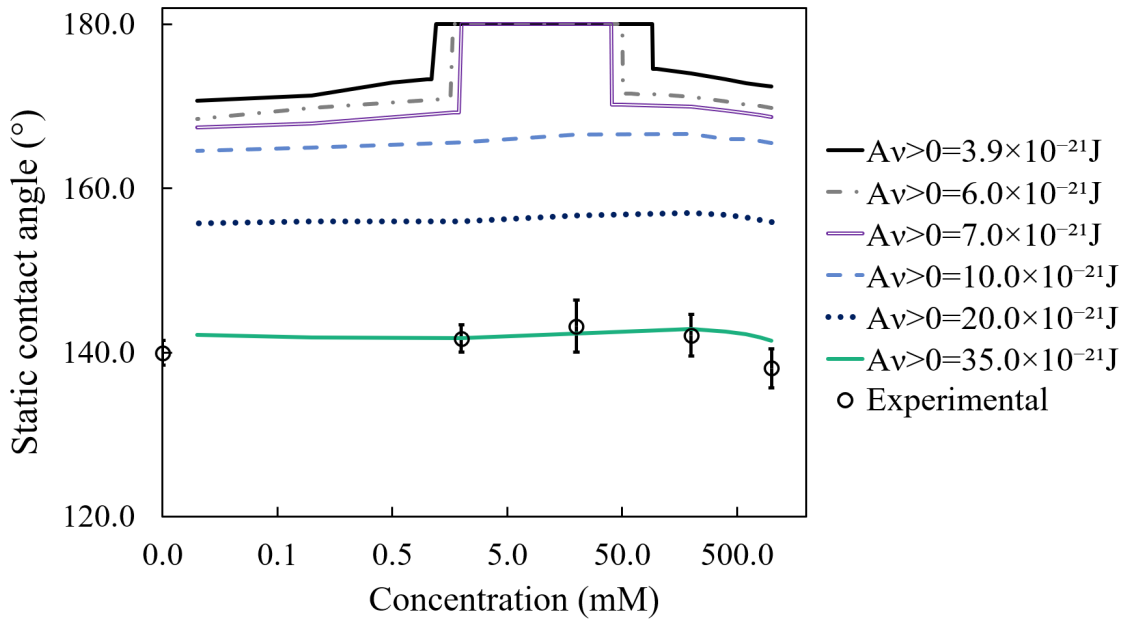
Figure 4.16: Contact angles as function of the electrolyte concentration for different Hamaker constants. $A_{\nu>0} = 3.9 \times 10^{-21}$ J is the calculated Hamaker constant using Lifshitz Theory.

Expectedly, the increment on the Hamaker coefficient resulted in an enhanced wettability of the solid by the oil phase. As the $A_{\nu>0}$ increased, the concentration range where the oil phase detaches decreased. Figure 4.16 demonstrates that setting $A_{\nu>0}$ to 35.0×10^{-21} J resulted in the best fit with the experimental data. Notably, there is good agreement between the calculated and experimental contact angles. Even for the highest concentrated system (1000mM), where PBE usually meets limitations [19], the standard error was found to be less than 2.5%. In these new simulations, CA did not vary expressively for each $A_{\nu>0}$, and no detachment of the oil phase was obtained. The overall wettability behavior was similar to the previously discussed results.

The new equilibrium thicknesses were smaller than the previously calculated and showed a marginal increase with increasing salinity outside the oil detachment concentration range (Figure 4.17). Table 4.10 shows the literature data for the ionic and hydrated diameters of ions and water. Notably, several calculated equilibrium thicknesses are close to the molecular diameter, and in some cases, are even smaller. This physical inconsistency is justified since PBE neglects the ion sizes. However, these findings invigorate the utilization of more detailed models, such as density functional theory, which incorporates excluded volumes.
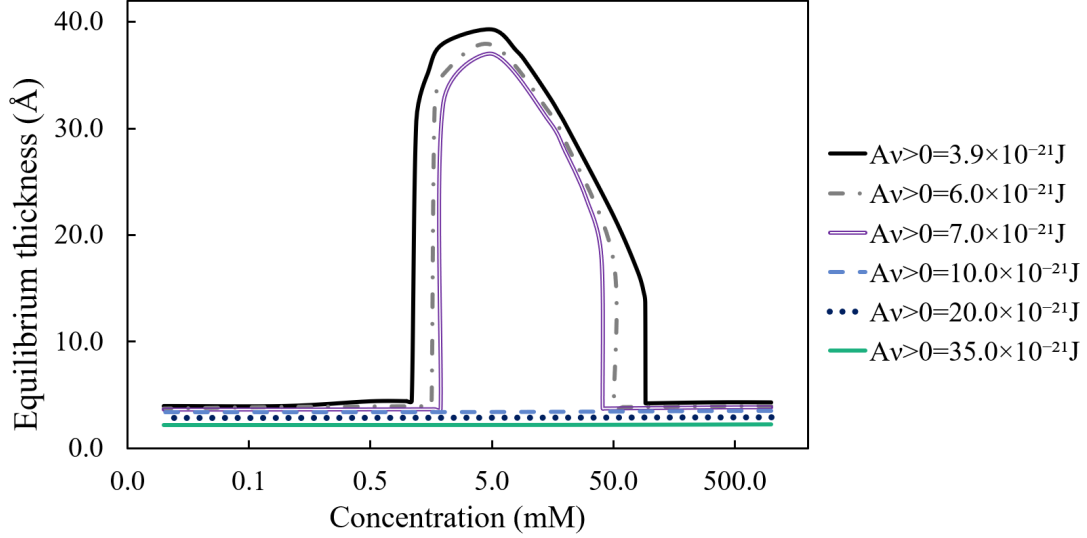
Figure 4.17: Film equilibrium thicknesses (L) as function of the electrolyte concentration for different Hamaker constants in a quartz/brine/decane system. $A_{\nu>0} = 3.9 \times 10^{-21}$J is the calculated Hamaker constant using Lifshitz Theory.

Table 4.10: Ionic and hydrated diameters.

Specie	Bare diameter(Å)	Hydrated diameter(Å)
Na^+	1.9	7.2
H_3O^+	-	5.6
Cl^-	3.6	6.6
OH^-	3.5	6.0
H_2O	2.5	-

Properties from [45].

The electrostatic potential and ions density profile, obtained using $A_{\nu>0} = 35.0 \times 10^{-21}$J, for different brines, are shown in Figures 4.18 and 4.19, respectively. The mean electrostatic potentials exhibited similar behavior to the previously calculated ones, with little variation along the film thickness. The potentials remained highly negative near the oil surface, which can be attributed to the reduction in the film thicknesses. Since equilibrium thicknesses varied only marginally (from 2.18 to 2.24Å), the ion screening effect on the electrostatic potential becomes evident as the ionic strength increases. The ion density profiles reflected the MEP behavior. Cations densities remained relatively constant throughout the film thickness. An enormous adsorption of Na^+ is observed in the lowest concentrated brine film as an attempt to balance the substantial existing negative MEP.
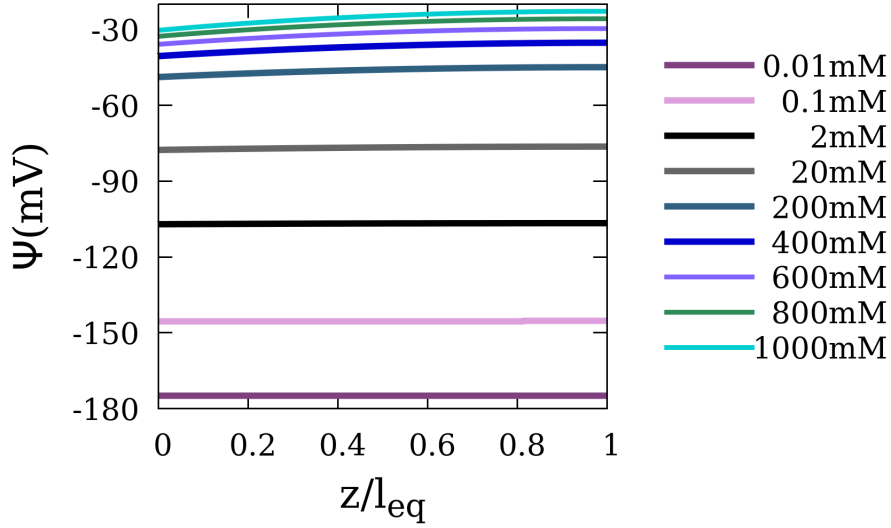
Figure 4.18: Simulated electrostatic potentials, using $A_{\nu>0} = 35.0 \times 10^{-21}$ J, as a function of the normalized film thicknesses of different brines.

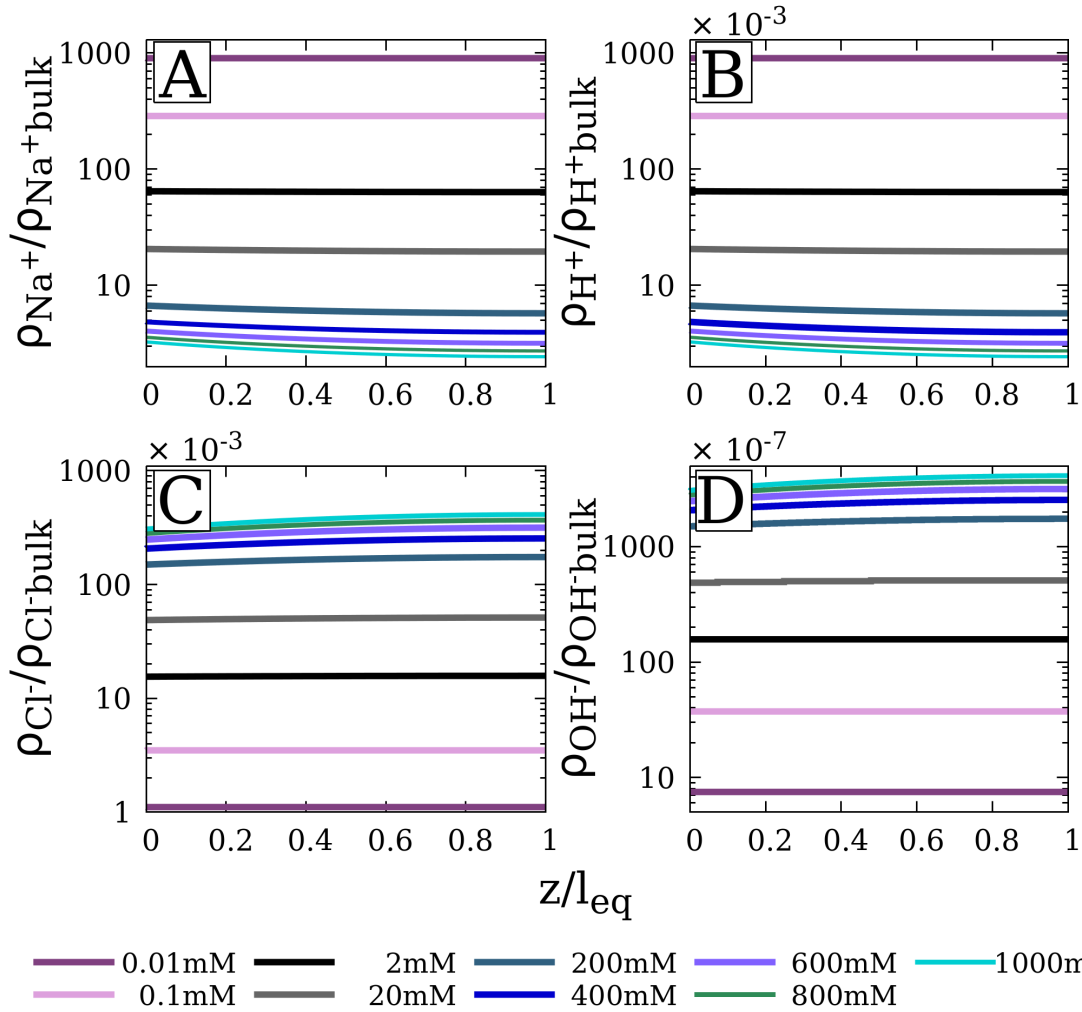Figure 4.19: Ions density profiles, using $A_{\nu>0} = 35.0 \times 10^{-21}$ J, as a function of the normalized film thicknesses for different brines: A) Na$^+$, B) H$^+$, C) Cl$^-$,and D) OH$^-$.

Figure 4.20 shows the disjoining pressure components, calculated using $A_{\nu>0} = 35.0 \times 10^{-21}$ J, as a function of film size, for different brines. The increase in the van der Waals interactions has resulted in a similar behavior of the total disjoining pressure for all brines, which explains the nearly constant wettability behavior observed in Figure 4.16. The equilibrium EDL disjoining pressure component is two orders of magnitude smaller than the van der Waals and structural components. Nonetheless, since both contributions are not affected by salinity, the wettability behaviour is determined by variation in the EDL component.
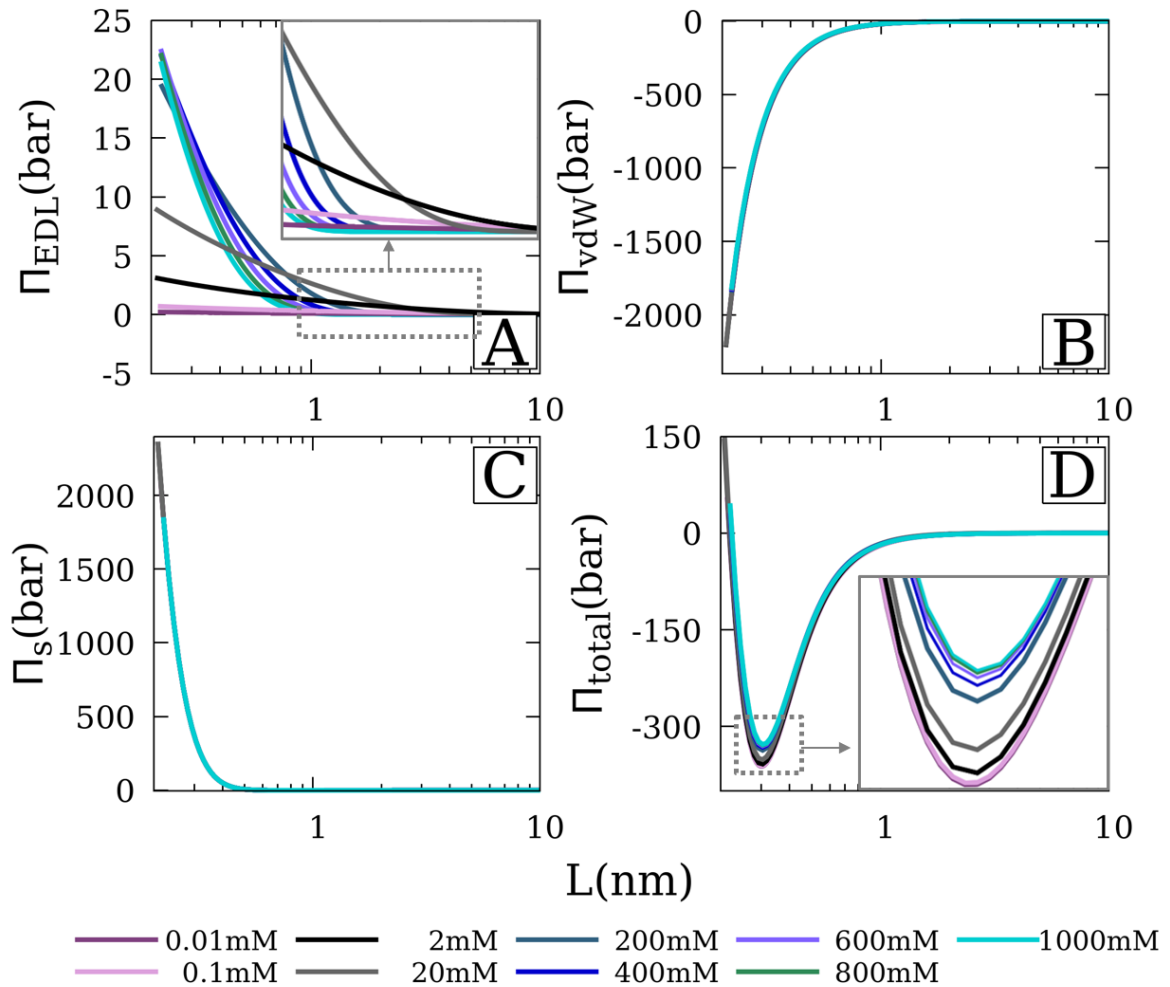
Figure 4.20: Disjoining pressure (Π) contributions using $A_{\nu>0} = 35.0 \times 10^{-21}$ J: (A) Double layer, (B) van der Waals, (C) structural, and (D) total disjoining pressure for different brines as a function of film thickness (L).

Interestingly, there is an inversion in the repulsion behavior of the brines as the film size diminishes. Initially, for larger film thicknesses, the lowest concentrated brine has the most repulsive Π_{EDL}. As the film size decreases slightly, the aqueous solution with a concentration of 0.1mM becomes more repulsive than the 0.01mM

one. This trend continues until the highest concentrated brine shows the most repulsive electrical behavior. The change in the MEP profile can explain that as the film size decreases. Referring to Equation (2.44), we observe that the first term on the right side depends on the derivative of the mean electrostatic potential concerning distance at the midplane of film thickness. As shown in Figure 4.21, when the film thickness decreases, this derivative diminishes, causing the second term related to concentrations to dominate Π_{EDL}. As observed previously, only sodium cations became highly adsorbed in the film. Consequently, the rise in the concentration of these cations as the film diminishes (Figure 4.22) leads to an increase in the electrostatic disjoining pressure component. Therefore, in very small film thicknesses, the dominant contribution to the electrical disjoining pressure are entropic effects.
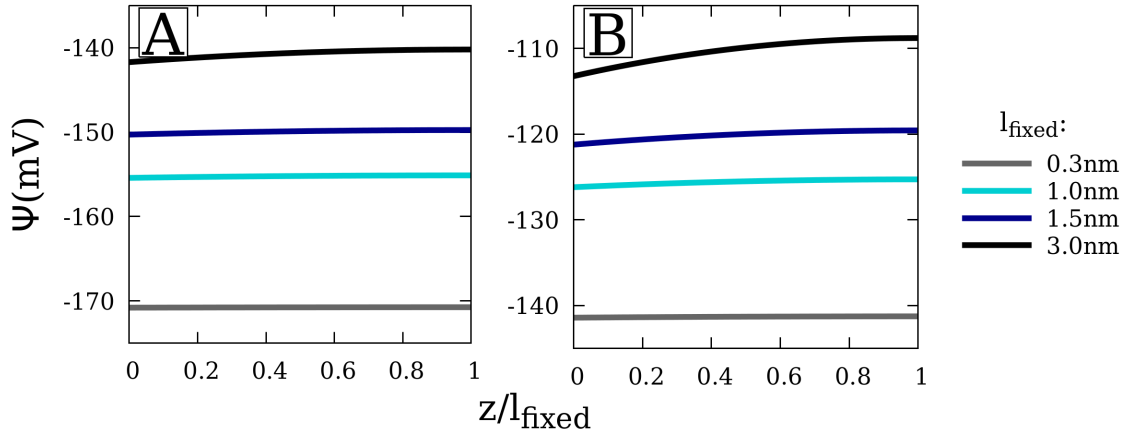

Figure 4.21: Effect of the film size (l_{fixed}) on the mean electrostatic potentials using $A_{\nu>0} = 35.0 \times 10^{-21}$J for 0.01mM (A) and 0.1mM (B) brines.

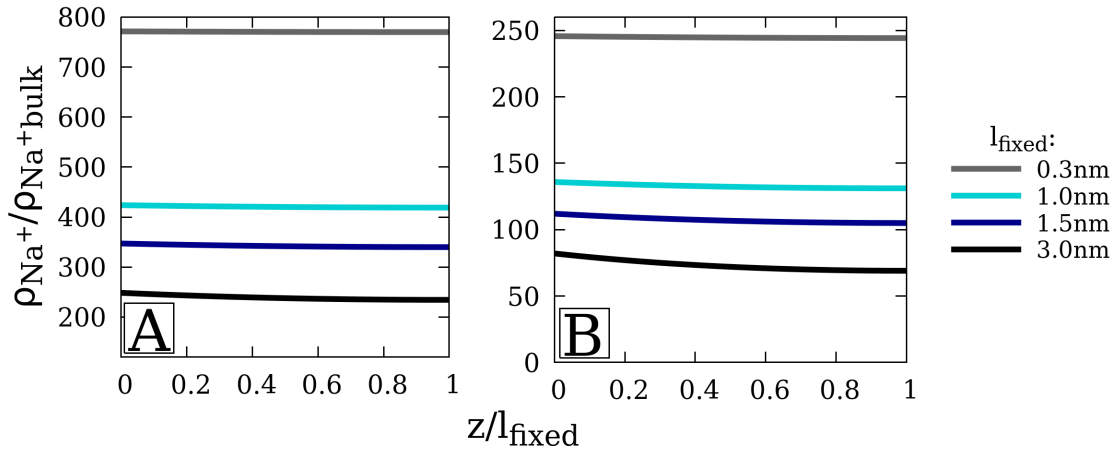Figure 4.22: Effect of the film size (l_{fixed}) on Na$^+$ profile using $A_{\nu>0} = 35.0 \times 10^{-21}$J for 0.01mM (A) and 0.1mM (B) brines.

In summary, for the quartz/decane/brine systems studied, the wettability of

quartz did not exhibit significant variations with changes in ionic strength, which is expected for a non-polar oil [11]. This behavior is consistent with the experimental data and values reported in the literature. The PBE model consistently captured this behavior and was able to represent it accurately. Additionally, the model proved to be useful in indicating possible inversions in the $\Pi_E DL$ contributions at lower film thicknesses. Moreover, considering the obtained film thickness, the influence of solvation and van der Waals forces was found to be highly significant.

4.5 Calculations of Quartz/Brine/Crude Oil Systems

Figures 4.23 and 4.24 present the calculated equilibrium thicknesses and contact angles for the quartz/crude oil/brine systems, along with experimental data from the work of Lu *et al.* [120]. This system contains two charged surfaces, quartz and crude oil. The presented data were estimated using the Hamaker coefficients calculated using Equation (2.33) and the best fitted to the experimental data ($A_{\nu>0} = 22.0 \times 10^{-21}$ J). The calculated equilibrium thicknesses showed a slight increase with the rise of the ionic strength, which contradicts experimental observations of higher concentrated systems [9, 10].

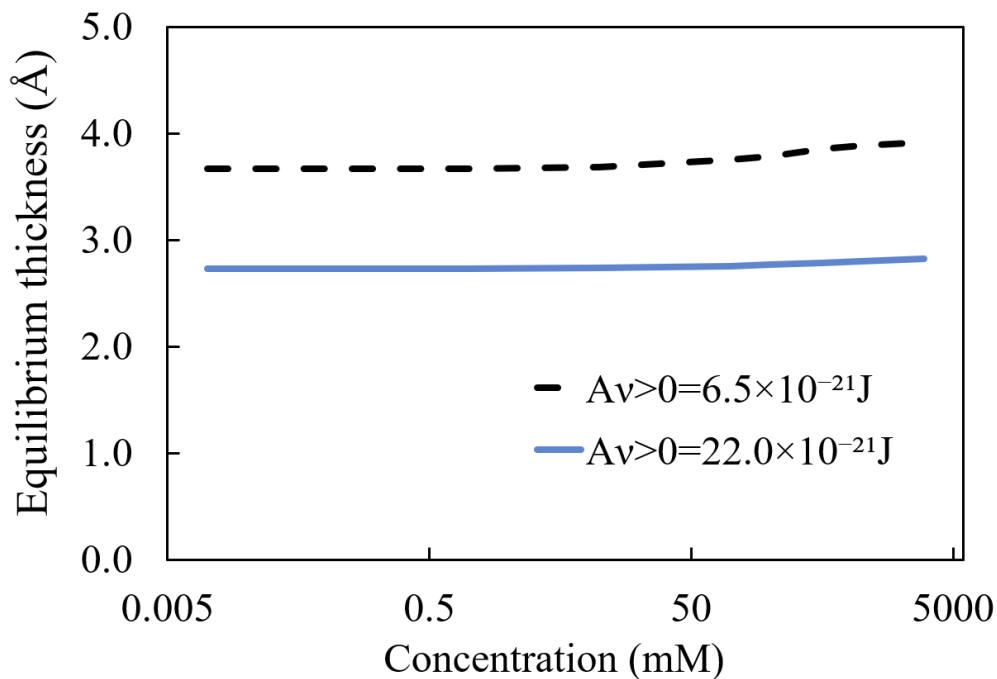Figure 4.23: Film equilibrium thicknesses (L) as function of the electrolyte concentration for the calculated, $A_{\nu>0}$=6.5×10^{-21}J, and best-fitted Hamaker constant, $A_{\nu>0} = 22.0 \times 10^{-21}$ J, in the system quartz/crude oil/brine.

Figure 4.24: Contact angles as a function of the electrolyte concentration for the calculated, $A_{v>0}$=6.5×10^{-21}J, and best-fitted Hamaker constant, $A_{v>0}$=22.0×10^{-21}J, in the system quartz/crude oil/brine. Ref.1 - Experimental data from Lu *et al.* [120].

The increase in the Hamaker constant improved the agreement with the experimental data obtained in lower salt concentrations. Since the PBE model does not consider entropic effects, the expected deviations between the calculated and experimental data in highly concentrated systems were found. These discrepancies might also be attributed to the variation of the fluid - fluid interactions with salinity. The surface parameters and IFTs used in the simulations were obtained from different sources [93, 107] and may not fully represent the studied system of Lu *et al.* [120]. Crude oils have a highly complex composition [8, 13], which can result in different interfacial and bulk properties. Even though it does not accurately represent the experimental data for higher concentrated systems, the model demonstrated the possibility of obtaining a significant variation in wettability, particularly when $A_{v>0}$ was equal to 22.0×10^{-21}J.

The mean electrostatic potential profiles for the quartz/brine/crude oil system, obtained using the Hamaker coefficient of 22.0×10^{-21}J, in different brines are shown in Figure 4.25.
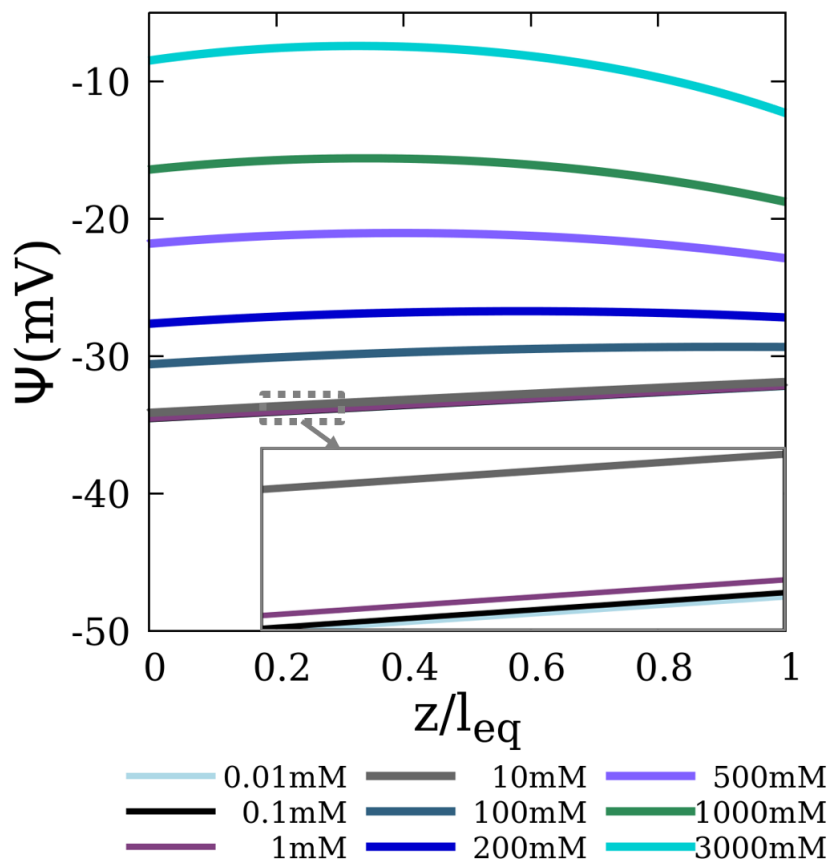
Figure 4.25: Calculated electrostatic potentials, using $A_{v>0} = 22.0 \times 10^{-21} J$, as a function of the normalized film thicknesses of different brines. The quartz and crude oil surfaces are at 0 and maximum normalized film thickness, respectively. The electrostatic potential profiles are nearly identical for 0.01, 0.1 and 1mM brines.

The MEP profile illustrates the superposition of the electrical potentials of each interface, which can result in different interfacial properties. The electrostatic potential profiles were nearly identical for 0.01, 0.1 and 1 mM brines, indicating that the electrostatic behavior becomes almost invariant. Notably, there is an inversion of the surface, which has a more negative electrical potential with increasing salinity. In brines with a concentration below 500 mM, quartz has the most negative surface potential, while in more concentrated systems, oil becomes more negative. Since the equilibrium thicknesses of all brine films were similar (ranging from 2.73 to 2.82 Å), the ions screening effects on the MEP can be observed. It is worth noting that the difference between the electrostatic potentials is not as expressive as it was observed in the quartz/brine/n-decane system.

Table 4.11 summarizes the quartz and crude oil surface charges at the equilibrium film thicknesses. The surface charges are consistent with the inversion of the most negative surface potential. As explained previously, as the salinity rises, the absolute charges at surfaces increase, which indicates a "competition" between cations Na^+

and H^+ to approach the surface sites, leading to the deprotonation of the surface. Interestingly, the surface charge of the crude oil interface became even positive for brines with a concentration below 20mM, indicating the predominant presence of groups $> NH^+$ on this surface.

Table 4.11: Charges at quartz and crude oil surfaces at equilibrium thicknesses for different brines using $A_{\nu>0} = 22.0 \times 10^{-21}$J.

Concentration (mM)	$Q_{quartz}(Cm^{-2})$	$Q_{crude\ oil}(Cm^{-2})$
0.01	-0.0060	0.0060
0.1	-0.0060	0.0060
1	-0.0060	0.0059
10	-0.0061	0.0052
100	-0.0070	-0.0006
200	-0.0079	-0.0055
500	-0.0098	-0.0154
1000	-0.0121	-0.0247
3000	-0.0164	-0.0393

The ion density profiles for the quartz/brine/crude oil system, obtained using the Hamaker coefficient of 22.0×10^{-21}J, in different brines are shown in Figure 4.26. Similarly to the MEP profiles presented, the profiles of cations and anions for the brines with concentration of 0.01, 0.1, and 1.0 mM were nearly identical. Na^+ and H^+ were strongly attracted to both quartz and oil surfaces. However, due to the inversion of the most negatively charged surface with the change in salinity, cations showed more affinity for the quartz surface for brines with concentrations below 500 mM. On the other hand, anions were more concentrated in the middle region of the film for the more concentrated systems (above 500mM), due the repulsion of both surfaces. For brines with concentrations below 500mM, anions exhibited more affinity for the oil surface.
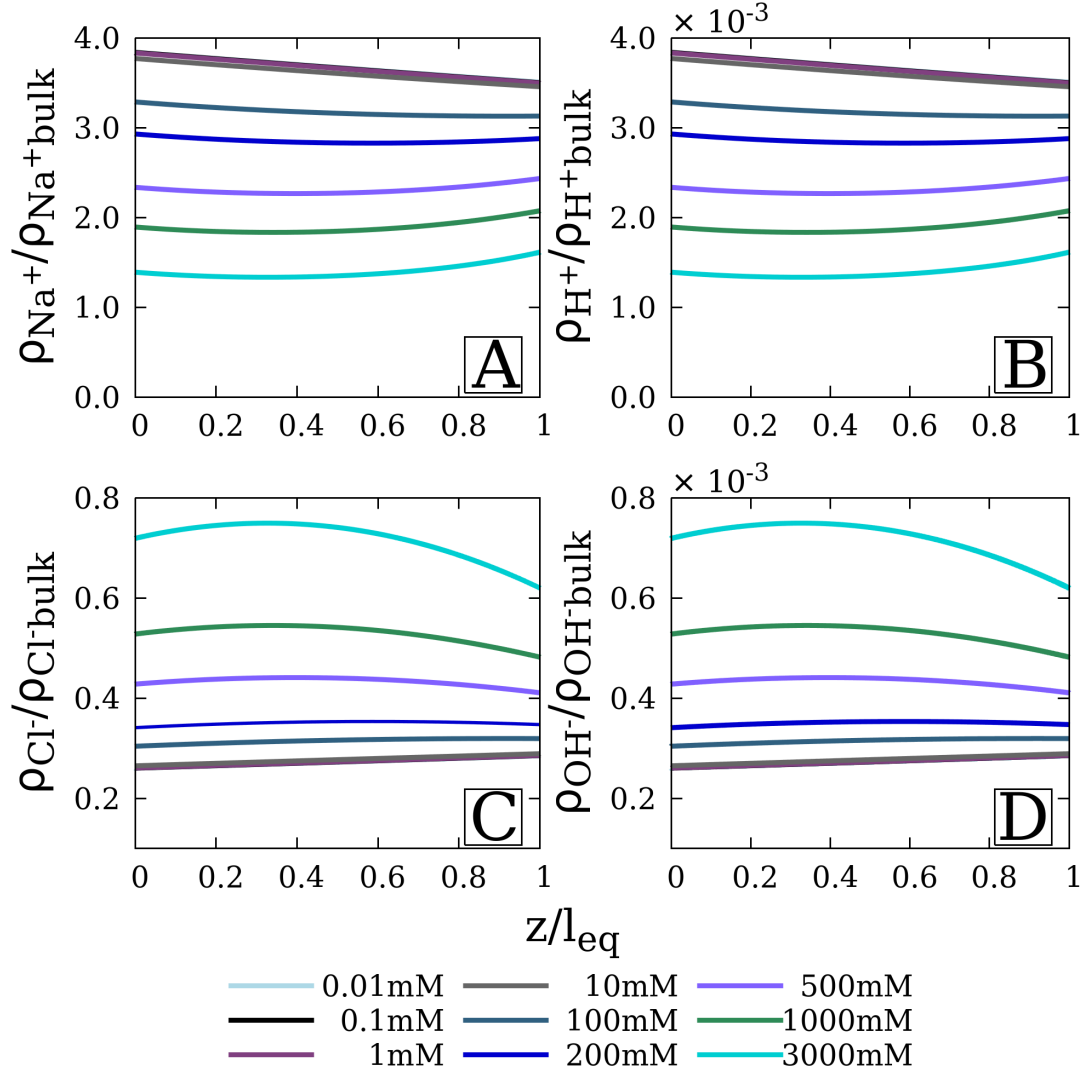
Figure 4.26: Ions density profiles, using $A_{v>0} = 22.0 \times 10^{-21} J$, as a function of the normalized film thicknesses for different brines: A) Na^+, B) H^+, C) Cl^-, and D) OH^-. The quartz and crude oil surfaces are at 0 and maximum normalized film thickness, respectively.

Figure 4.27 shows the disjoining pressure components, calculated using $A_{v>0} = 22.0 \times 10^{-21} J$, as a function of film size, for different brines. Similarly to the quartz/brine/n-decane system, vdW and structural contributions to the DP are greater than the EDL component, yet they do not dominate the total disjoining pressure behavior since they are not affected by the salinity. Interestingly, similarly to Figure 4.20, an inversion of the EDL repulsion behavior of brines was found as the film thickness was reduced. This effect is again attributed to the diminishing impact of the electrostatic potential and the increasing concentration of the electrostatic component as the film size decreases.
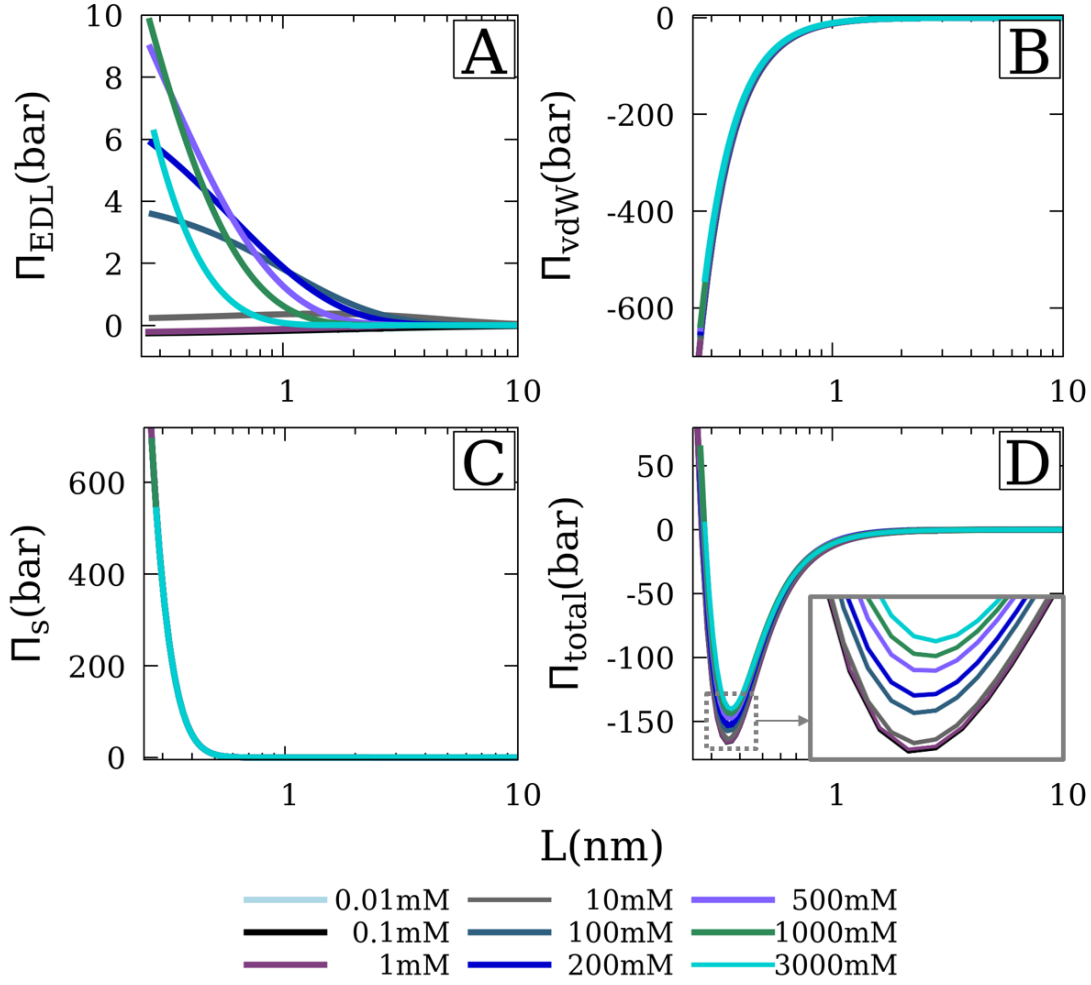
Figure 4.27: Disjoining pressure (Π) contributions in the quartz/brine/crude oil system, using $A_{v>0} = 30.0 \times 10^{-21} J$: (A) Double layer, (B) van der Waals, (C) structural, and (D) total disjoining pressure for different brines as a function of film thickness (L).

The effect of pH alterations on the contact angle and the equilibrium thickness, using $A_{v>0}$=22.0×10^{-21}J, is presented in Figures 4.28 and 4.29. The increase in the pH diminished the wettability of quartz by the oil phase and expanded the concentration range of oil detachment. This finding aligns with the expectations for a sandstone reservoir [11]. Moreover, the calculated contact angles at a pH of 8 are in better agreement with the experimental data at higher concentration, which could be an explanation for the previously mentioned deviations in the higher salinity range. As explained by Lyu *et al.* [11], the salinity influences the solubility of organic substances in water. Therefore, pH variation could result from the interaction between crude oil compounds and different brines. Unfortunately, the work of Lu *et al.* [120] does not provide pH measurements. Nevertheless, this observation illustrates the potential action of simultaneous phenomena that could be critical for understanding the wettability behavior.
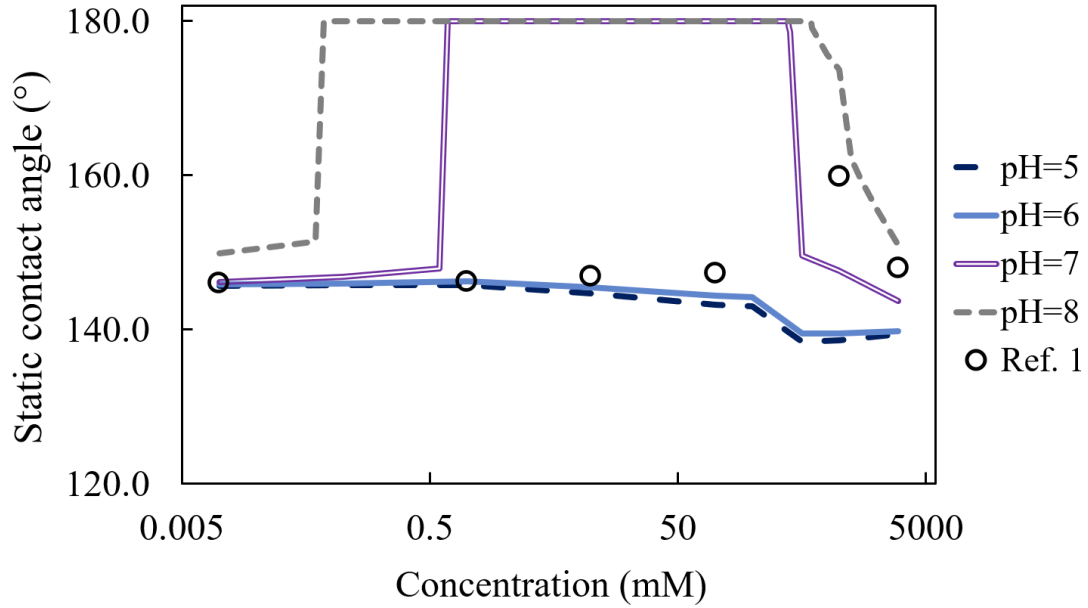
Figure 4.28: Contact angles as a function of the electrolyte concentration for different pHs, using $A_{v>0}$=22.0×10^{-21}J, in the system quartz/crude oil/brine. Ref.1 - Experimental data from Lu *et al.* [120].
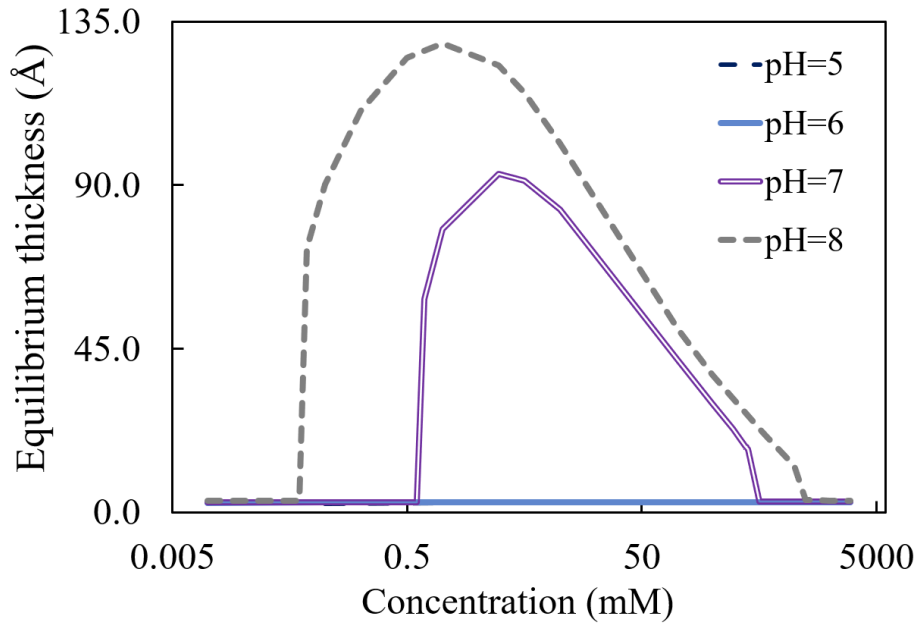
Figure 4.29: Film equilibrium thicknesses (L) as function of the electrolyte concentration for for different pHs, using $A_{v>0}$=22.0×10^{-21}J, in the system quartz/crude oil/brine.

The main effect of the pH alteration is on the charge density of both surfaces, as observed in Figures 4.30 and 4.31. At low salt concentrations, the surfaces become more protonated, making the surface charge densities to approach zero. The increase in the Na$^+$ ion concentration makes the surface less protonated, resulting in

a decrease in the charge densities from pH 6 to 8. Since the surface charge density depends on the equilibrium thickness, we observe changes in the derivative of the curves for pH 7 and 8 due to the wettability change occuring at 388mM and 590mM, respectively.

Figure 4.30: Quartz surface charge densities as a function of the electrolyte concentration for different pHs, using $A_{v>0}=22.0\times10^{-21}$J at the equilibrium thicknesses, in the system quartz/crude oil/brine.

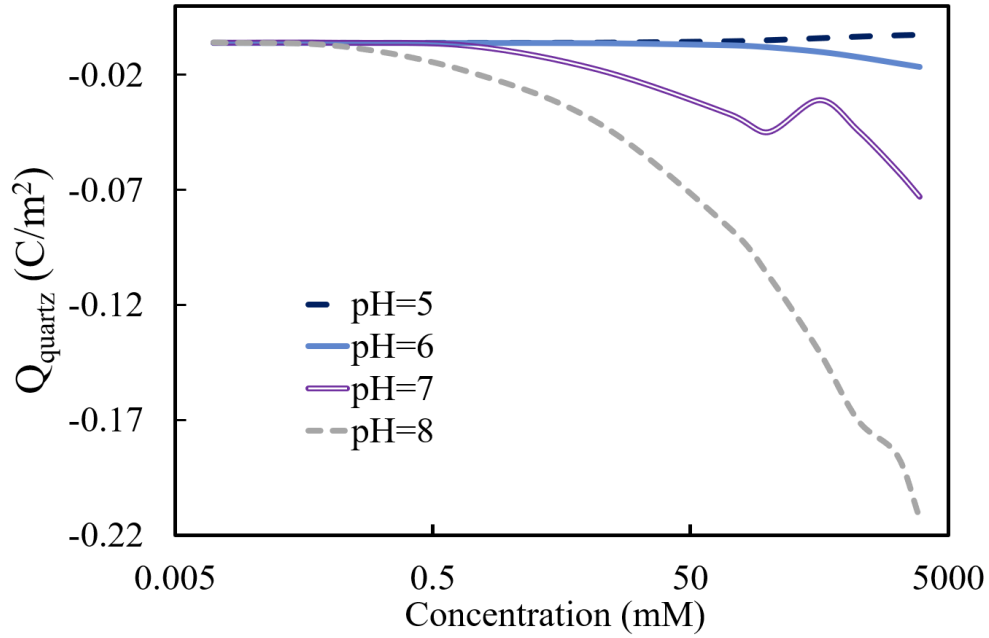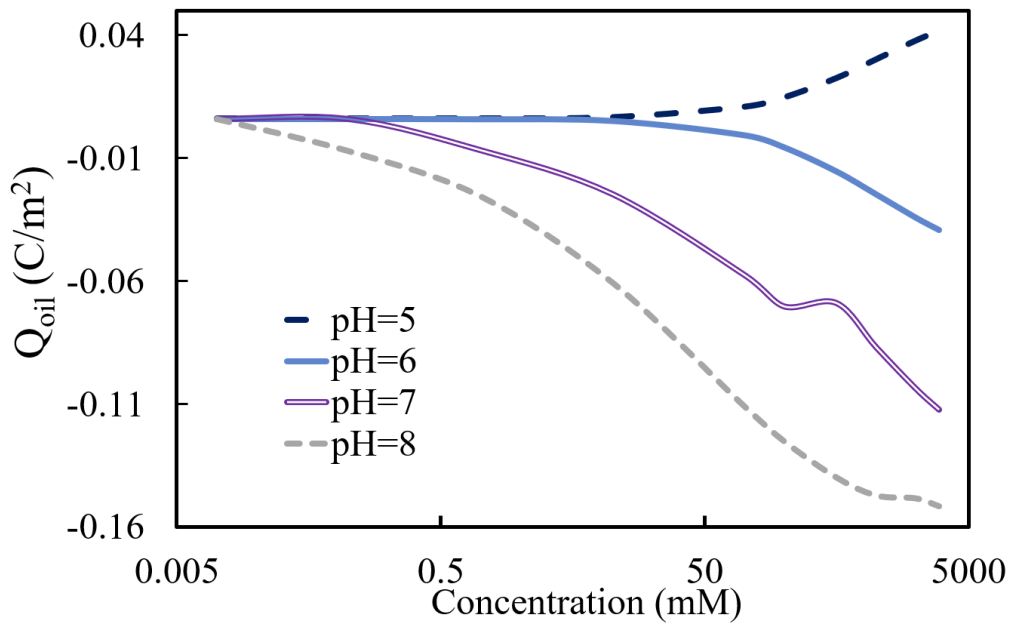Figure 4.31: Crude oil surface charge densities as a function of the electrolyte concentration for different pHs, using $A_{v>0}=22.0\times10^{-21}$J at the equilibrium thicknesses, in the system quartz/crude oil/brine.

Interestingly, an opposite trend is observed at a pH of 5. The increase on the concentration of H^+ causes the protonation of both surfaces. The crude oil surface becomes positively charged within all the concentration range, indicating the dominance of $> NH^+$ groups at the surface. Consequently, the electrostatic potential becomes positive along the distance for all brines, as shown in Figure 4.32.
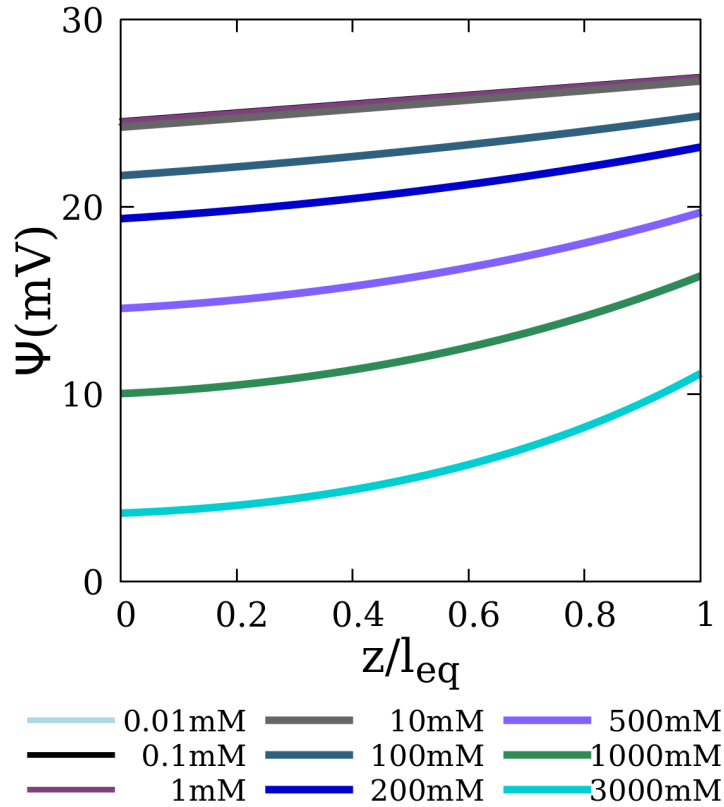
Figure 4.32: Calculated electrostatic potentials, using $A_{v>0} = 22.0 \times 10^{-21} J$ at pH 5, as a function of the normalized film thicknesses of different brines. The quartz and crude oil surfaces are at 0 and maximum normalized film thickness, respectively. The electrostatic potential profiles are nearly identical for 0.01, 0.1 and 1mM brines.

The ion density profiles for the same system at pH of 5, using a Hamaker coefficient of 22.0×10^{-21}J, in different brines are shown in Figure 4.33. The profiles of cations and anions for the brines with concentration of 0.01, 0.1, and 1.0 mM were nearly identical. While all anions become adsorbed in the film, the cations are depleted. As expected, Cl^- and OH^- exhibit a greater affinity towards the oil surface, which is positively charge. On the other hand, Na^+ and H^+ are more concentrated near the quartz surface, which is negatively charged (Figure 4.30).
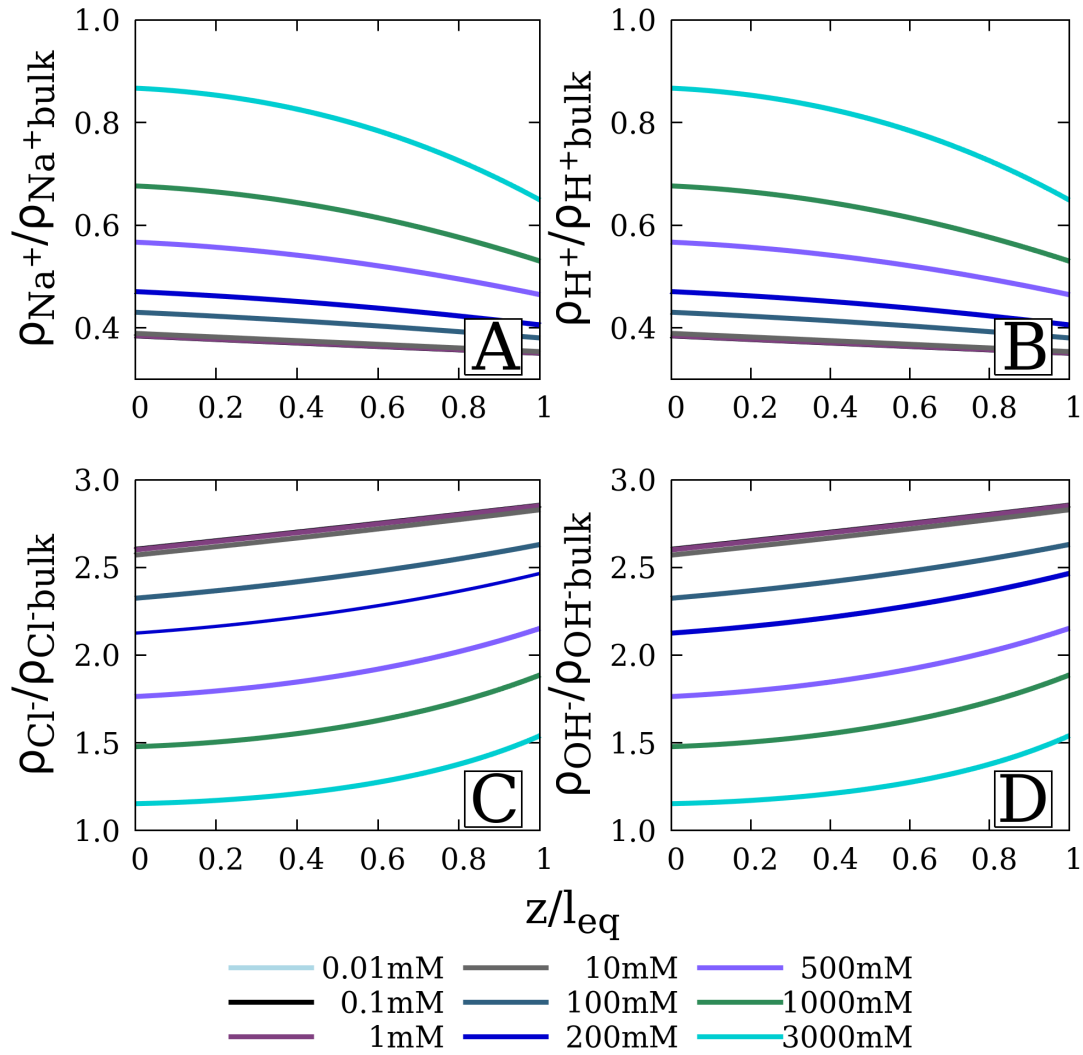
Figure 4.33: Ions density profiles, using $A_{v>0} = 22.0 \times 10^{-21} J$ at pH of 5, as a function of the normalized film thicknesses for different brines: A) Na^+, B) H^+, C) Cl^-, and D) OH^-. The quartz and crude oil surfaces are at 0 and maximum normalized film thickness, respectively.

All in all, the PBE model used here can accurately represent the wettability of a quartz/crude oil/brine system for low-concentrated aqueous solutions. Other aspects regarding the oil surface parameters, the changes in the fluid-fluid interactions and the pH variation may help to explain the wettability behavior in highly concentrated systems, highlighting the importance of a comprehensive understanding of the phenomena involved in the system. Besides, these calculations demonstrated important features, such as a more significant wettability alteration and an inversion in the surface charge density with the variation of pH.

Chapter 5

Conclusions and Suggestions

This work investigates the wettability of solid/oil/brine model systems using a combination of goniometry and computer simulations. The study focused on understanding the influence of three types of interactions: Coulombic, van der Waals, and structural forces. For the quartz/decane/brine systems studied, contact angles exhibited a modest variation in the wettability of quartz with increasing salinity. This observation is consistent with both experimental and theoretical expectations for a non-polar oil [13, 23]. Importantly, the PBE model consistently captured and accurately represented this behavior, even for the high-salinity brine. Lastly, the calculations demonstrated the substantial impact of van der Waals and solvation forces within the film.

Calculations of the quartz/brine/crude oil systems were able to reproduce the experimental data reported in the literature for the low-salinity range. In highly concentrated systems, additional information about the system, including the oil surface parameters, alterations in the fluid-fluid interactions and variations in pH may be required to explain the wettability behavior. Furthermore, calculations provided valuable insights into the system, revealing the possibility of observing the wettability alteration as well as the inversion of the surface charge density in response to pH changes.

Overall, this work emphasizes the importance of understanding the underlying mechanisms of the rock/oil/brine systems. Hence, a logical progression of this research could involve measuring contact angles and interfacial tensions with fully characterized crude oil. Furthermore, the study of a more realistic surface, such as an outcrop sandstone, is recommended in order to understand the role of fluid-solid interactions.

Given that the size scale of the calculated film thicknesses was very small and was physically incompatible, future studies using more sophisticated approaches, including the size of particles, such as classical density functional theory and molecular simulation, are suggested. This could enhance the potential of using these models

to control and manipulate wettability in practical applications.

References

[1] L. M. Grigoryev and D. D. Medzhidova, "Global energy trilemma," *Russian Journal of Economics*, vol. 6, no. 4, pp. 437–462, 2020.

[2] "World energy trilemma index 2022," 2022.

[3] L. Marti and R. Puertas, "Sustainable energy development analysis: Energy trilemma," *Sustainable Technology and Entrepreneurship*, vol. 1, no. 1, p. 100007, 2022.

[4] S. Carley and D. M. Konisky, "The justice and equity implications of the clean energy transition," *Nature Energy*, vol. 5, no. 8, pp. 569–577, 2020.

[5] "bp statistical review of world energy 2022," 2022.

[6] R. Farajzadeh, G. Glasbergen, V. Karpan, R. Mjeni, D. Boersma, A. Eftekhari, A. C. Garcia, and J. Bruining, "Improved oil recovery techniques and their role in energy efficiency and reducing co2 footprint of oil production," *Journal of Cleaner Production*, vol. 369, p. 133308, 2022.

[7] C. Dai, Q. You, M. Zhao, G. Zhao, and F. Zhao, *Principles of Enhanced Oil Recovery*. Singapore: Springer Nature, 2023.

[8] N. Morrow and J. Buckley, "Improved oil recovery by low-salinity waterflooding," *Journal of petroleum Technology*, vol. 63, no. 05, pp. 106–112, 2011.

[9] T. Austad, "Water-based eor in carbonates and sandstones: new chemical understanding of the eor potential using smart water," in *Enhanced oil recovery Field case studies*, pp. 301–335, Elsevier, 2013.

[10] P. C. Myint and A. Firoozabadi, "Thin liquid films in improved oil recovery from low-salinity brine," *Current Opinion in Colloid & Interface Science*, vol. 20, no. 2, pp. 105–114, 2015.

[11] C. Lyu, L. Zhong, Z. Ning, M. Chen, and D. R. Cole, "Review on underlying mechanisms of low salinity waterflooding: comparisons between sandstone and carbonate," *Energy & Fuels*, vol. 36, no. 5, pp. 2407–2423, 2022.

[12] H. Tian, F. Liu, X. Jin, and M. Wang, "Competitive effects of interfacial interactions on ion-tuned wettability by atomic simulations," *Journal of colloid and interface science*, vol. 540, pp. 495–500, 2019.

[13] W. G. Anderson, "Wettability literature survey-part 1: rock/oil/brine interactions and the effects of core handling on wettability," *Journal of petroleum technology*, vol. 38, no. 10, pp. 1125–1144, 1986.

[14] G. Hirasaki, "Wettability: fundamentals and surface forces," *SPE formation evaluation*, vol. 6, no. 02, pp. 217–226, 1991.

[15] A. Neumann and R. Good, "Techniques of measuring contact angles," *Surface and Colloid Science: Volume 11: Experimental Methods*, pp. 31–91, 1979.

[16] Q. Xie, A. Saeedi, E. Pooryousefy, and Y. Liu, "Extended dlvo-based estimates of surface force in low salinity water flooding," *Journal of Molecular Liquids*, vol. 221, pp. 658–665, 2016.

[17] T. S. Duffy, I. K. Gamwo, R. T. Johns, and S. N. Lvov, "Modeling contact angle vs. temperature for the quartz-water-decane system," *SPE Journal*, vol. 26, no. DOE/NETL-2021/2811, 2021.

[18] V. A. Parsegian and D. Gingell, "On the electrostatic interaction across a salt solution between two bodies bearing unequal charges," *Biophysical journal*, vol. 12, no. 9, pp. 1192–1204, 1972.

[19] J. Masliyah and S. Bhattacharjee, *Electrokinetic and Colloid Transport Phenomena*. Hoboken: Wiley-Interscience, 2006.

[20] R. Evans, *Density Functional Theory for Inhomogeneous Fluids I: Simple Fluids in Equilibrium*, ch. 2. Kazimierz Dolny, Poland: Warsaw University Press, 2009.

[21] N. S. V. Barbosa, E. R. de Almeida Lima, and F. W. Tavares, "Molecular modeling in chemical engineering," *Reference Module in Chemistry, Molecular Sciences and Chemical Engineering*, 2017.

[22] P. Rostami, M. F. Mehraban, M. Sharifi, M. Dejam, and S. Ayatollahi, "Effect of water salinity on oil/brine interfacial behaviour during low salinity waterflooding: A mechanistic study," *Petroleum*, vol. 5, no. 4, pp. 367–374, 2019.

[23] A. Kakati and J. S. Sangwai, "Wettability alteration of mineral surface during low-salinity water flooding: role of salt type, pure alkanes, and model oils

containing polar components," *Energy & Fuels*, vol. 32, no. 3, pp. 3127–3137, 2018.

[24] R. Cossé, *Oil and gas field development techniques. Basics of reservoir engineering.* Paris: Editions Technips, 1993.

[25] D. Myers, *Surfaces, interfaces, and colloids*, vol. 415. New York: Wiley-VCH, 1999.

[26] F. Ding and M. Gao, "Pore wettability for enhanced oil recovery, contaminant adsorption and oil/water separation: A review," *Advances in Colloid and Interface Science*, vol. 289, p. 102377, 2021.

[27] K. Bjorlykke, *Petroleum geoscience: From sedimentary environments to rock physics.* Heidelberg, New York, Dordrecht, London: Springer, 2 ed., 2015.

[28] L. Yue, W. Pu, S. Zhao, S. Zhang, F. Ren, and D. Xu, "Insights into mechanism of low salinity water flooding in sandstone reservoir from interfacial features of oil/brine/rock via intermolecular forces," *Journal of Molecular Liquids*, vol. 313, p. 113435, 2020.

[29] P. Mahzari, M. Sohrabi, and J. M. Façanha, "The decisive role of microdispersion formation in improved oil recovery by low-salinity-water injection in sandstone formations," *SPE Journal*, vol. 24, no. 06, pp. 2859–2873, 2019.

[30] O. Hjelmeland and L. Larrondo, "Experimental investigation of the effects of temperature, pressure, and crude oil composition on interfacial properties," *SPE Reservoir Engineering*, vol. 1, no. 04, pp. 321–328, 1986.

[31] W. Wang and A. Gupta, "Investigation of the effect of temperature and pressure on wettability using modified pendant drop method," in *SPE Annual Technical Conference and Exhibition?*, pp. SPE–30544, SPE, 1995.

[32] T. S. Duffy, J. Li, R. T. Johns, and S. N. Lvov, "Capillary contact angle for the quartz-distilled water-normal decane interface at temperatures up to 200 c," *Colloids and Surfaces A: Physicochemical and Engineering Aspects*, vol. 609, p. 125608, 2021.

[33] Y. Zhang, J. Zeng, J. Qiao, X. Feng, and Y. Dong, "Investigating the effect of the temperature and pressure on wettability in crude oil–brine–rock systems," *Energy & Fuels*, vol. 32, no. 9, pp. 9010–9019, 2018.

[34] H.-J. Butt, K. Graf, and M. Kappl, *Physics and chemistry of interfaces.* Germany: John Wiley & Sons, 2003.

[35] G. Bracco and B. Holst, *Surface science techniques*. Heidelberg, New York, Dordrecht, London: Springer Science & Business Media, 2013.

[36] R. N. Wenzel, "Resistance of solid surfaces to wetting by water," *Industrial & engineering chemistry*, vol. 28, no. 8, pp. 988–994, 1936.

[37] A. Cassie and S. Baxter, "Wettability of porous surfaces," *Transactions of the Faraday society*, vol. 40, pp. 546–551, 1944.

[38] A. Cassie, "Contact angles," *Discussions of the Faraday society*, vol. 3, pp. 11–16, 1948.

[39] D. Murakami, H. Jinnai, and A. Takahara, "Wetting transition from the cassie–baxter state to the wenzel state on textured polymer surfaces," *Langmuir*, vol. 30, no. 8, pp. 2061–2067, 2014.

[40] D. Shaw and D. Shaw, *Introduction to Colloid and Surface Chemistry*. Chemical, Petrochemical & Process, Oxford: Butterworth-Heinemann, 4th ed. ed., 1992.

[41] A. I. Rusanov and V. A. Prokhorov, *Interfacial tensiometry*. Amsterdam, Lausanne, New York, Oxford, Shannon and Tokyo: Elsevier, 1996.

[42] H. Green, S. Ono, S. Kondo, F. P. Buff, S. Ono, and S. Kondo, "Molecular theory of surface tension in liquids," *Structure of Liquids/Struktur der Flüssigkeiten*, pp. 134–280, 1960.

[43] J. Drelich, C. Fang, and C. White, "Measurement of interfacial tension in fluid-fluid systems," *Encyclopedia of surface and colloid science*, vol. 3, pp. 3158–3163, 2002.

[44] J. D. Berry, M. J. Neeson, R. R. Dagastine, D. Y. Chan, and R. F. Tabor, "Measurement of surface and interfacial tension using pendant drop tensiometry," *Journal of colloid and interface science*, vol. 454, pp. 226–237, 2015.

[45] J. N. Israelachvili, *Intermolecular and surface forces*. Boston: Academic Press, third edition ed., 2011.

[46] H. Helmholtz, "Studien über electrische grenzschichten," *Annalen der Physik*, vol. 243, no. 7, pp. 337–382, 1879.

[47] E. R. A. Lima, *Cálculo de propriedades físico-químicas de sistemas coloidais via equação de Poisson-Boltzmann*. PhD thesis, Universidade Federal do Rio de Janeiro, 2008.

[48] M. Boström, E. R. Lima, E. C. Biscaia Jr, F. W. Tavares, and W. Kunz, *Modifying the Poisson–Boltzmann Approach to Model Specific Ion Effects*, pp. 293–309. New Jersey, London, Singapore, Beijing, Shanghai, Hong Kong, Taipei and Chennai: World Scientific, 2010.

[49] R. Roth and D. Gillespie, "Shells of charge: a density functional theory for charged hard spheres," *Journal of Physics: Condensed Matter*, vol. 28, no. 24, p. 244006, 2016.

[50] N. S. V. Barbosa, *Poisson-Boltzmann equation and classical Density Functional Theory applied to electrolyte solutions: from biological systems to enhanced oil recovery.* PhD thesis, Universidade do Estado do Rio de Janeiro, 2019.

[51] T. T. Duignan, S. M. Kathmann, G. K. Schenter, and C. J. Mundy, "Toward a first-principles framework for predicting collective properties of electrolytes," *Accounts of Chemical Research*, vol. 54, no. 13, pp. 2833–2843, 2021.

[52] E. d. A. Soares, N. S. Vernin, M. S. Santos, and F. W. Tavares, "Real electrolyte solutions in the functionalized mean spherical approximation: A density functional theory for simple electrolyte solutions," *The Journal of Physical Chemistry B*, vol. 126, no. 32, pp. 6095–6101, 2022.

[53] P. Hohenberg and W. Kohn, "Inhomogeneous electron gas," *Physical review*, vol. 136, no. 3B, p. B864, 1964.

[54] D. A. McQuarrie, *Statistical Mechanics.* Harper's Chemistry Series, New York: HarperCollins Publishing, Inc., 1976.

[55] F. W. Tavares, D. Bratko, H. W. Blanch, and J. M. Prausnitz, "Ion-specific effects in the colloid- colloid or protein- protein potential of mean force: role of salt- macroion van der waals interactions," *The Journal of Physical Chemistry B*, vol. 108, no. 26, pp. 9228–9235, 2004.

[56] P. V. Brady, N. R. Morrow, A. Fogden, V. Deniz, and N. Loahardjo, "Electrostatics and the low salinity effect in sandstone reservoirs," *Energy & Fuels*, vol. 29, no. 2, pp. 666–677, 2015.

[57] S. A. Lima, M. A. Murad, and R. Domingues, "A new multiscale computational model for low salinity alkaline waterflooding in clay-bearing sandstones," in *SPE Reservoir Simulation Conference*, OnePetro, 2017.

[58] M. Bonto, A. A. Eftekhari, and H. M. Nick, "An overview of the oil-brine interfacial behavior and a new surface complexation model," *Scientific reports*, vol. 9, no. 1, p. 6072, 2019.

[59] M. Takeya, A. Ubaidah, M. Shimokawara, H. Okano, T. Nawa, and Y. Elakneswaran, "Crude oil/brine/rock interface in low salinity waterflooding: Experiments, triple-layer surface complexation model, and dlvo theory," *Journal of Petroleum Science and Engineering*, vol. 188, p. 106913, 2020.

[60] F. Bordeaux-Rego, M. Mehrabi, A. Sanaei, and K. Sepehrnoori, "Improvements on modelling wettability alteration by engineered water injection: Surface complexation at the oil/brine/rock contact," *Fuel*, vol. 284, p. 118991, 2021.

[61] F. W. Tavares, I. S. V. Segtovich, and F. A. Medeiros, *Termodinâmica na Engenharia Química*. Rio de Janeiro: LTC, 1st ed. ed., 2023.

[62] V. A. Parsegian, *Van der Waals forces: a handbook for biologists, chemists, engineers, and physicists*. Cambridge, New York, Melbourne, Madrid, Cape Town, Singapore, São Paulo: Cambridge university press, 2005.

[63] H. C. Hamaker, "The londonvan der waals attraction between spherical particles," *physica*, vol. 4, no. 10, pp. 1058–1072, 1937.

[64] J. Gregory, "Approximate expressions for retarded van der waals interaction," *Journal of colloid and interface science*, vol. 83, no. 1, pp. 138–145, 1981.

[65] C. J. van Oss, M. Chaudhury, and R. J. Good, "Monopolar surfaces," *Advances in colloid and interface science*, vol. 28, pp. 35–64, 1987.

[66] N. S. Barbosa, E. R. Lima, and F. W. Tavares, "Wettability of rock, oil and brine system based on density functional theory," *Fluid Phase Equilibria*, vol. 479, pp. 99–105, 2019.

[67] N. R. Morrow, *Interfacial phenomena in petroleum recovery*. New York: Marcel Dekker, 1991.

[68] A. Firoozabadi, *Thermodynamics and applications in hydrocarbon energy production*. New York, Chicago, San Francisco, Athens, London, Madrid, Mexico City, Milan, New Delhi, Singapore, Sydney and Toronto: McGraw-Hill Education, 2016.

[69] B. V. Derjaguin, N. V. Churaev, V. M. Muller, and V. Kisin, *Surface forces*. Moscow: Springer Science and Business Media New York, 1987.

[70] A. I. Rusanov, "Surface thermodynamics revisited," *Surface Science Reports*, vol. 58, no. 5-8, pp. 111–239, 2005.

[71] S. Basu and M. M. Sharma, "Measurement of critical disjoining pressure for dewetting of solid surfaces," *Journal of colloid and interface science*, vol. 181, no. 2, pp. 443–455, 1996.

[72] M. Sadeqi-Moqadam, S. Riahi, and A. Bahramian, "An investigation into the electrical behavior of oil/water/reservoir rock interfaces: The implication for improvement in wettability prediction," *Colloids and Surfaces A: Physicochemical and Engineering Aspects*, vol. 490, pp. 268–282, 2016.

[73] R. J. Hunter, *Foundations of colloid science.* Oxford, New York, Athens, and other: Oxford University Press, 2 ed., 2001.

[74] H. Guo, N. Nazari, S. Esmaeilzadeh, and A. R. Kovscek, "A critical review of the role of thin liquid films for modified salinity brine recovery processes," *Current Opinion in Colloid & Interface Science*, vol. 50, p. 101393, 2020.

[75] H. N. Al-Saedi, R. E. Flori, and P. V. Brady, "Effect of divalent cations in formation water on wettability alteration during low salinity water flooding in sandstone reservoirs: Oil recovery analyses, surface reactivity tests, contact angle, and spontaneous imbibition experiments," *Journal of Molecular Liquids*, vol. 275, pp. 163–172, 2019.

[76] H. N. Al-Saedi, P. V. Brady, R. E. Flori, and P. Heidari, "Insights into the role of clays in low salinity water flooding in sand columns," *Journal of Petroleum Science and Engineering*, vol. 174, pp. 291–305, 2019.

[77] H. Ivuawuogu, Y. Cheng, Y. Zhang, and S. Khataniar, "Experimental investigation of the role of different clays in low salinity waterflooding," in *SPE Annual Technical Conference and Exhibition*, OnePetro, 2020.

[78] X. Wei, Y. Zhang, W. Jiang, Z. Wang, X. Li, and F. Wu, "Experimental investigation on the role of clays in low salinity water flooding," *Frontiers in Energy Research*, vol. 8, p. 593639, 2020.

[79] Y. Hu, Z. Chu, C. Dai, F. Wang, H. Ren, X. Jin, and Y. Wu, "Probing of the hydrated cation bridges in the oil/brine/silica system via atomic force microscopy and molecular dynamics simulation," *Fuel*, vol. 306, p. 121666, 2021.

[80] G. Liu, F. Jiang, L. Ge, Q. Zhang, X. Chen, Z. Fan, and J. Wang, "Investigation of salinity and ion effects on low salinity water flooding efficiency in a tight sandstone reservoir," *Energy Reports*, vol. 9, pp. 2732–2744, 2023.

[81] N. S. Al Maskari, Q. Xie, and A. Saeedi, "Role of basal-charged clays in low salinity effect in sandstone reservoirs: adhesion force on muscovite using atomic force microscope," *Energy & Fuels*, vol. 33, no. 2, pp. 756–764, 2019.

[82] Y. Chen, V. J. Niasar, and Q. Xie, "Electrostatic characterization of the- cooh–brine–clay system: Implications for wettability alteration during low salinity waterflooding in sandstone reservoirs," *Energy & Fuels*, vol. 35, no. 20, pp. 16599–16606, 2021.

[83] M. Saeed, P. Jadhawar, S. C. Ayirala, R. Abhishek, and Y. Zhou, "Modelling the effects of reservoir parameters and rock mineralogy on wettability during low salinity waterflooding in sandstone reservoirs," *Journal of Petroleum Science and Engineering*, vol. 215, p. 110676, 2022.

[84] C. Fang, S. Sun, and R. Qiao, "Structure, thermodynamics, and dynamics of thin brine films in oil–brine–rock systems," *Langmuir*, vol. 35, no. 32, pp. 10341–10353, 2019.

[85] M. M. Koleini, M. H. Badizad, H. Mahani, A. M. Dastjerdi, S. Ayatollahi, and M. H. Ghazanfari, "Atomistic insight into salinity dependent preferential binding of polar aromatics to calcite/brine interface: implications to low salinity waterflooding," *Scientific reports*, vol. 11, no. 1, p. 11967, 2021.

[86] G. M. Ong, A. Gallegos, and J. Wu, "Modeling surface charge regulation of colloidal particles in aqueous solutions," *Langmuir*, vol. 36, no. 40, pp. 11918–11928, 2020.

[87] J. Zhao, G. Yao, S. B. Ramisetti, R. B. Hammond, and D. Wen, "Molecular dynamics simulation of the salinity effect on the n-decane/water/vapor interfacial equilibrium," *Energy & Fuels*, vol. 32, no. 11, pp. 11080–11092, 2018.

[88] R. K. Saw and A. Mandal, "A mechanistic investigation of low salinity water flooding coupled with ion tuning for enhanced oil recovery," *RSC advances*, vol. 10, no. 69, pp. 42570–42583, 2020.

[89] J. T. Tetteh, S. E. Cudjoe, S. A. Aryana, and R. B. Ghahfarokhi, "Investigation into fluid-fluid interaction phenomena during low salinity waterflooding

using a reservoir-on-a-chip microfluidic model," *Journal of Petroleum Science and Engineering*, vol. 196, p. 108074, 2021.

[90] J. Song, S. Rezaee, W. Guo, B. Hernandez, M. Puerto, F. M. Vargas, G. J. Hirasaki, and S. L. Biswal, "Evaluating physicochemical properties of crude oil as indicators of low-salinity–induced wettability alteration in carbonate minerals," *Scientific reports*, vol. 10, no. 1, p. 3762, 2020.

[91] R. Mokhtari, S. Ayatollahi, and M. Fatemi, "Experimental investigation of the influence of fluid-fluid interactions on oil recovery during low salinity water flooding," *Journal of Petroleum Science and Engineering*, vol. 182, p. 106194, 2019.

[92] F. Mugele, B. Bera, A. Cavalli, I. Siretanu, A. Maestro, M. Duits, M. Cohen-Stuart, D. Van Den Ende, I. Stocker, and I. Collins, "Ion adsorption-induced wetting transition in oil-water-mineral systems," *Scientific reports*, vol. 5, no. 1, p. 10519, 2015.

[93] J. V. Nicolini, *Formulação de água de injeção por nanofiltração para recuperação avançada de petróleo*. PhD thesis, Universidade Federal do Rio de Janeiro, 2017.

[94] D. E. Yates, *The structure of the oxide/aqueous electrolyte interface*. PhD thesis, University of Melbourne, 1975.

[95] J. De Boer, M. Hermans, and J. Vleeskens, "Chemisorption and physical adsorption of water on silica," *Proc. Kon. Ned. Akad.*, vol. B60, pp. 45–54, 1957.

[96] J. A. Hockey and B. A. Pethica, "Surface hydration of silicas," *Transactions of the Faraday Society*, vol. 57, pp. 2247–2262, 1961.

[97] C. Armistead, A. Tyler, F. Hambleton, S. Mitchell, and J. A. Hockey, "Surface hydroxylation of silica," *The Journal of Physical Chemistry*, vol. 73, no. 11, pp. 3947–3953, 1969.

[98] A. C. Riese, *Adsorption of radium and thorium onto quartz and kaolinite. a comparison of solution/surface equilibria models*. PhD thesis, Colorado School of Mines, 1982.

[99] L. Zhuravlev, "Concentration of hydroxyl groups on the surface of amorphous silicas," *Langmuir*, vol. 3, no. 3, pp. 316–318, 1987.

[100] L. Zhuravlev, "Surface characterization of amorphous silicaa review of work from the former ussr," *Colloids and Surfaces A: Physicochemical and Engineering Aspects*, vol. 74, no. 1, pp. 71–90, 1993.

[101] E. F. Vansant, P. Van Der Voort, and K. C. Vrancken, *Characterization and chemical modification of the silica surface.* The Netherlands: Elsevier, 1995.

[102] L. Zhuravlev, "The surface chemistry of amorphous silica. zhuravlev model," *Colloids and Surfaces A: Physicochemical and Engineering Aspects*, vol. 173, no. 1-3, pp. 1–38, 2000.

[103] T. Hiemstra, W. H. Van Riemsdijk, and G. Bolt, "Multisite proton adsorption modeling at the solid/solution interface of (hydr) oxides: A new approach: I. model description and evaluation of intrinsic reaction constants," *Journal of colloid and interface science*, vol. 133, no. 1, pp. 91–104, 1989.

[104] C. Tang, J. Zhu, Q. Zhou, J. Wei, R. Zhu, and H. He, "Surface heterogeneity of sio2 polymorphs: an xps investigation of α-quartz and α-cristobalite," *The Journal of Physical Chemistry C*, vol. 118, no. 45, pp. 26249–26257, 2014.

[105] J. Yang, H. Su, C. Lian, Y. Shang, H. Liu, and J. Wu, "Understanding surface charge regulation in silica nanopores," *Physical Chemistry Chemical Physics*, vol. 22, no. 27, pp. 15373–15380, 2020.

[106] P. Leroy, A. Maineult, S. Li, and J. Vinogradov, "The zeta potential of quartz. surface complexation modelling to elucidate high salinity measurements," *Colloids and Surfaces A: Physicochemical and Engineering Aspects*, vol. 650, p. 129507, 2022.

[107] P. V. Brady and J. L. Krumhansl, "A surface complexation model of oil–brine–sandstone interfaces at 100 c: Low salinity waterflooding," *Journal of Petroleum Science and Engineering*, vol. 81, pp. 171–176, 2012.

[108] L. Bergström, "Hamaker constants of inorganic materials," *Advances in colloid and interface science*, vol. 70, pp. 125–169, 1997.

[109] A. George and R. Singh, "Electronic polarizability of light crude oil from optical and dielectric studies," in *Journal of Physics: Conference Series*, vol. 869, p. 012016, IOP Publishing, 2017.

[110] A. Michaels and E. Hauser, "Interfacial tension at elevated pressure and temperature. ii. interfacial properties of hydrocarbon–water systems.," *The Journal of Physical Chemistry*, vol. 55, no. 3, pp. 408–421, 1951.

[111] A. A. Adewunmi and M. S. Kamal, "Effect of water/decane ratios and salt on the stability, rheology, and interfacial tension of water/decane emulsions," *Energy & Fuels*, vol. 33, no. 9, pp. 8456–8462, 2019.

[112] H. Y. Jennings Jr and G. H. Newman, "The effect of temperature and pressure on the interfacial tension of water against methane-normal decane mixtures," *Society of petroleum engineers Journal*, vol. 11, no. 02, pp. 171–175, 1971.

[113] S. Velusamy, S. Sakthivel, and J. S. Sangwai, "Effect of imidazolium-based ionic liquids on the interfacial tension of the alkane–water system and its influence on the wettability alteration of quartz under saline conditions through contact angle measurements," *Industrial & Engineering Chemistry Research*, vol. 56, no. 46, pp. 13521–13534, 2017.

[114] A. M. Sayed, K. B. Olesen, A. S. Alkahala, T. I. Sølling, and N. Alyafei, "The effect of organic acids and salinity on the interfacial tension of n-decane/water systems," *Journal of Petroleum Science and Engineering*, vol. 173, pp. 1047–1052, 2019.

[115] A. Goebel and K. Lunkenheimer, "Interfacial tension of the water/n-alkane interface," *Langmuir*, vol. 13, no. 2, pp. 369–372, 1997.

[116] R. Aveyard and D. Haydon, "Thermodynamic properties of aliphatic hydrocarbon/water interfaces," *Transactions of the Faraday Society*, vol. 61, pp. 2255–2261, 1965.

[117] R. Aveyard and S. M. Saleem, "Interfacial tensions at alkane-aqueous electrolyte interfaces," *Journal of the Chemical Society, Faraday Transactions 1: Physical Chemistry in Condensed Phases*, vol. 72, pp. 1609–1617, 1976.

[118] J.-A. Felipe and F. Abbas, "Tunable substrate wettability by thin water layer," *The Journal of Physical Chemistry*, vol. 120, pp. 24688–24696, 2016.

[119] H. Ding and S. Rahman, "Experimental and theoretical study of wettability alteration during low salinity water flooding-an state of the art review," *Colloids and Surfaces A: Physicochemical and Engineering Aspects*, vol. 520, pp. 622–639, 2017.

[120] Y. Lu, N. F. Najafabadi, and A. Firoozabadi, "Effect of temperature on wettability of oil/brine/rock systems," *Energy & Fuels*, vol. 31, no. 5, pp. 4989–4995, 2017.